# INVESTIGATING THE AGGREGATION OF NEURODEGENERATIVE PROTEINS USING MOLECULAR DYNAMICS SIMULATIONS: IMPLICATIONS FOR TAU PATHOGENESIS

By

**Unmesh Dutta Chowdhury**

**Enrolment No - CHEM11201804028**

**National Institute of Science Education and Research, Bhubaneswar**

*A thesis submitted to the*

*Board of Studies in Chemical Sciences*

*In partial fulfillment of requirements*

*for the Degree of*

**DOCTOR OF PHILOSOPHY**
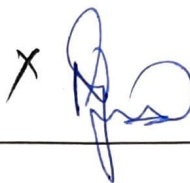
*of*

**HOMI BHABHA NATIONAL INSTITUTE**

July, 2023

# Homi Bhabha National Institute
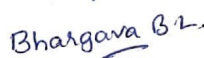
## Recommendations of the Viva Voce Committee

As members of the Viva Voce Committee, we certify that we have read the dissertation prepared by **Unmesh Dutta Chowdhury** entitled **"Investigating the aggregation of neurodegenerative proteins using molecular dynamics simulations: Implications for tau pathogenesis"** and recommend that it may be accepted as fulfilling the thesis requirement for the award of Degree of Doctor of Philosophy.

Chairman – Dr. Sharanappa Nembenna          Date: 3/11/2023

Guide / Convener – Dr. Bhargava B. L.   Bhargava BL    Date: 03.11.2023

Examiner – Prof. Sandip Paul    Sandip Paul    Date: 3/11/2023

Member 1 – Dr. U. Lourderaj          Date: 3/11/2023

Member 2 – Dr. V. Krishnan    V. Krishnan    Date: 3/11/2023

Member 3 – Dr. Snehasis Chowdhuri          Date: 3/11/2023

Final approval and acceptance of this thesis is contingent upon the candidate's submission of the final copies of the thesis to HBNI.

I/We hereby certify that I/we have read this thesis prepared under my/our direction and recommend that it may be accepted as fulfilling the thesis requirement.

Date: 03.11.2023

Place: NISER, Bhubaneswar

Bhargava BL

(Dr. Bhargava B. L.)

Guide

## STATEMENT BY AUTHOR

This dissertation has been submitted in partial fulfillment of requirements for an advanced degree at Homi Bhabha National Institute (HBNI) and is deposited in the Library to be made available to borrowers under rules of the HBNI.

Brief quotations from this dissertation are allowable without special permission, provided that accurate acknowledgement of source is made. Requests for permission for extended quotation from or reproduction of this manuscript in whole or in part may be granted by the Competent Authority of HBNI when in his or her judgment the proposed use of the material is in the interests of scholarship. In all other instances, however, permission must be obtained from the author.

Unmesh Dutta Chowdhury

Name & Signature of the Student

# DECLARATION

I hereby declare that I am the sole author of this thesis in partial fulfillment of the requirements for a postgraduate degree from National Institute of Science Education and Research (NISER). I authorize NISER to lend this thesis to other institutions or individuals for the purpose of scholarly research.

Unmesh Dutta Chowdhury

Name & Signature of the Student

## List of Publications

**Journal**

1. Chowdhury, U. D., Bhargava, B. L. (2022). Helix-coil Transition and Conformational Deformity in A$\beta$ 42-Monomer: a Case Study using the Zn$^{2+}$ cation. J. Biomol. Struct. Dyn., 40(19), 8949-8960.

2. Chowdhury, U. D., Malayil, I., Bhargava, B. L. (2023). Understanding the Screening effect of Aqueous DES on the IDPs: A Molecular Dynamics Simulation Study using Amyloid $\beta$ 42 Monomer. J. Mol. Graph. Model., 119, 108398.

3. Chowdhury, U. D., Paul, A., Bhargava, B. L. (2022). The effect of Lipid Composition on the Dynamics of Tau Fibrils. Proteins, 90(12), 2103-2115.

4. Chowdhury, U. D., Paul, A., Bhargava, B. L. (2023). Interaction of the Tau Fibrils with the Neuronal Membrane. Biophys. Chem., 298, 107024.

5. Chowdhury, U. D., Paul, A., Bhargava, B. L. Phosphatidylinositol (Pl) lipids Modulate the Binding of Tau Fibrils on Lipid Bilayers *(*Manuscript in Preparation).

6. Dash, S., Chowdhury, U. D., Bhargava, B. L. (2022). The Effect of External salts on the Aggregation of the Multiheaded Surfactants: All-atom Molecular Dynamics Studies. J. Mol. Graph. Model., 111, 108110.

7. Chowdhury, U. D., Bhargava, B. L. (2022). Understanding the Conformational changes in the Influenza B M2 Ion Channel at various Protonation States. Biophys. Chem., 289, 106859.

## Conferences

1. EMBO Workshop: In situ structural biology: from cryo-EM to multi scale modelling, European Molecular Biology Laboratory Meyerhofstraße, Heidelberg, February 2023, Germany.

2. Biocxcel Summer School on Biomolecular Simulations, Science and Technology Park of Sardinia, Pula, June 2022, Italy.

3. National Conference on Molecular Modelling and Simulations (NCMMS) VIT Bhopal, February 2022, India.

4. Theoretical Chemistry Symposium, IISER Kolkata / IACS Kolkata / Kalyani University, December 2021, India.

5. Theoretical Chemistry Symposium, BITS Pilani, February 2019, India.

Unmesh Dutta Chowdhury

Name & Signature of the Student

# DEDICATIONS

To all the women in my family, on whose grit, and sacrifices, rests my future doctoral privilege.

# Contents

# Summary

Alzheimer's disease (AD) and dementia are conditions that impact memory, thinking, and behavior. Around 50 million people worldwide have dementia, and this number is expected to increase to 152 million by 2050, particularly in low and middle-income countries. Neurodegenerative diseases such as dementia are characterized by the accumulation of specific proteins within the brain, including amyloid beta (A$\beta$ 42/40) and tau. Amyloid $\beta$ peptide with the metal ions ($Cu^{2+}$ and $Zn^{2+}$) stabilize the amyloid beta also evident from our simulations. Since the drug targets for the amyloid beta remained unsuccessful, the focus has been shifted to the biophysical characterization of tau aggregation and their role as therapeutic targets. The cryo-electron microscopy (cyro-EM) structures of the tau filaments, packed along with the lipid bilayers are taken as the starting configuration for the molecular dynamics simulations. A fundamental understanding of the interaction of tau fibrils with the cell membrane is pivotal to deciphering tau pathogenesis. So far, no studies are providing a molecular-level picture of the effects of bilayer compositions on tau morphology. The influence of the charge on the lipids and the presence of cholesterol, phosphatidylinositol [PI(4,5)P2] in the bilayer on the structure of tau fibrils can be deciphered from the interactions of the tau fibrils with the model bilayers. The MD simulation studies provide insights into the tau binding to the cell membrane and the key residues governing the interaction. Finally, to gain a detailed understanding of the interaction of tau fibrils and the cell membrane, we carried out microseconds of all-atom MD simulations imitating the in-vivo composition of neuronal membranes. MD simulations thus help elucidate the essential residues and key interactions that provide insights into designing tau-targeted therapeutics.

# List of Figures

4

5

# List of Tables

# Chapter 1

# Introduction

Protein folding is a fundamental biological process in which a linear chain of amino acids assumes its three-dimensional functional structure [1]. The folding of proteins is crucial for their stability, functionality, and interactions with other molecules within cells. However, in certain circumstances, proteins can misfold or aggregate abnormally, leading to detrimental consequences for cellular health [2, 3]. Neurodegenerative diseases, such as Alzheimer's disease, Parkinson's disease, Huntington's disease, and amyotrophic lateral sclerosis (ALS), are characterized by the accumulation of misfolded proteins and their subsequent aggregation in specific regions of the brain [4]. These protein aggregates are believed to play a central role in the pathogenesis of these disorders, leading to neuronal dysfunction and ultimately neurodegeneration. In this thesis, we will explore the process of protein folding and delve into the mechanisms underlying the abnormal aggregation of neurodegenerative proteins. Protein folding and the abnormal aggregation of neurodegenerative proteins play critical roles in the pathogenesis of neurodegenerative diseases. Understanding the intricate mechanisms underlying protein misfolding and aggregation is essential for the development of effective therapeutic strategies. Targeting protein misfolding, enhancing protein quality control systems, and modulating the aggregation process are potential approaches to mitigate the detrimental effects of neurodegenerative protein aggregates and halt disease progression. Further research in this field is crucial to unravel the complexities of protein folding and aggregation and to pave the way for novel therapeutic interventions in neurodegenerative diseases.

The role of protein misfolding in the aggregation of neurodegenerative proteins is cru-

cial in the pathogenesis of neurodegenerative diseases. Protein misfolding refers to the incorrect folding of proteins, leading to the adoption of aberrant conformations that are thermodynamically unstable. Misfolded proteins are prone to self-association and aggregation, resulting in the formation of insoluble protein aggregates, which are a hallmark of many neurodegenerative disorders [2].

There are several key aspects of protein misfolding that contribute to the aggregation process

- **Genetic Mutations**: In certain neurodegenerative diseases, such as Alzheimer's disease, Parkinson's disease, and Huntington's disease, specific genetic mutations can lead to the production of mutant proteins that are more prone to misfolding. These mutations may alter the stability, structure, or folding pathway of the proteins, making them more susceptible to misfolding and subsequent aggregation [5, 6].

- **Conformational Changes**: Proteins have distinct folding pathways that guide them to their native three-dimensional structures. However, factors such as genetic mutations, environmental stressors, or post-translational modifications can disrupt the folding process, resulting in the misfolding of proteins. Misfolded proteins may adopt partially folded or partially unfolded states, exposing hydrophobic regions that are normally buried within the native structure. These exposed hydrophobic regions act as aggregation-prone sites, facilitating the self-association of proteins and the formation of aggregates [7].

- **Oligomer Formation**: Misfolded proteins can form soluble oligomeric intermediates during the aggregation process. Oligomers are small assemblies of misfolded proteins with a higher propensity for toxicity than larger aggregates. Oligomers are believed to be the most toxic species in neurodegenerative diseases, as they can disrupt cellular processes, induce oxidative stress, impair synaptic function, and initiate

inflammatory responses [8].

- **Seeding and Templating**: Once protein aggregates start to form, they can act as seeds or templates for the recruitment and conversion of soluble proteins into aggregates. This process, known as seeding or templating, propagates the aggregation process and accelerates the formation of larger and more stable aggregates. The aggregated proteins can induce conformational changes in soluble proteins, leading to their misfolding and subsequent incorporation into the growing aggregates [9].

- **Spreading of Aggregates**: In some neurodegenerative diseases, the misfolded proteins can propagate from cell to cell, spreading the pathology throughout the brain. This phenomenon is believed to occur through the release of misfolded proteins or aggregates from affected cells, which can be taken up by neighboring cells and initiate the aggregation process in previously unaffected regions. The spreading of aggregates contributes to the progressive nature of neurodegenerative diseases [10].

The aggregation of misfolded proteins in neurodegenerative diseases leads to the formation of insoluble protein aggregates, including amyloid plaques, Lewy bodies, neurofibrillary tangles, and inclusion bodies [4]. These aggregates disrupt cellular functions, impair protein degradation pathways, induce cellular stress responses, and trigger neuroinflammation, ultimately leading to neuronal dysfunction and neurodegeneration.

Understanding the role of protein misfolding and aggregation is crucial for the development of therapeutic strategies aimed at preventing or reversing the aggregation process in neurodegenerative diseases. Targeting the mechanisms involved in protein misfolding, promoting protein quality control systems, and inhibiting the formation and spreading of aggregates are potential therapeutic approaches to mitigate the pathological effects of protein aggregation in neurodegenerative disorders.
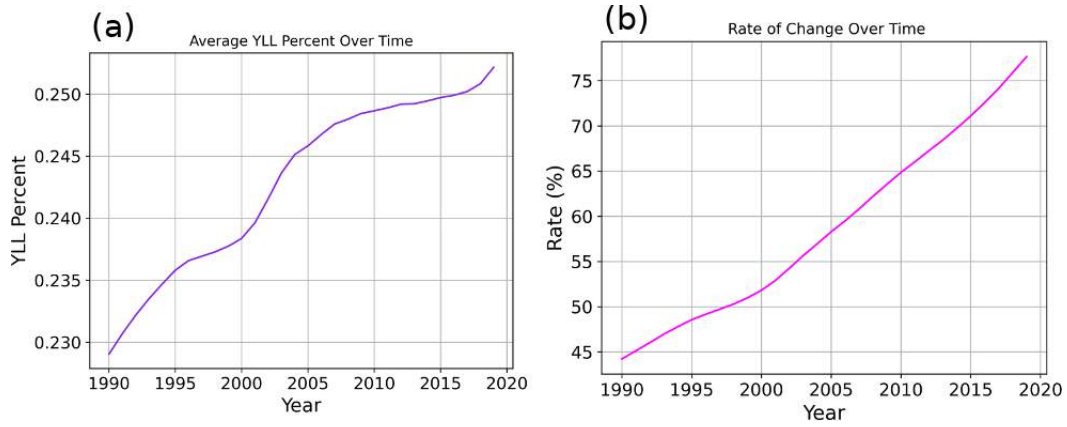
Figure 1.1: 'YLL' refers to the 'years of life lost' related to neurological disorders. Raw data is taken from online Global Health Data Exchange (GHDx) Query Tool. https://vizhub.healthdata.org/gbd-results

## 1.1    Aggregation of Neurodegenerative Proteins

Alzheimer's disease (AD) and dementia are conditions that affect memory, thinking, and behavior. Around 50 million people worldwide have dementia, and this number is expected to increase to 152 million by 2050, particularly in low and middle-income countries. These conditions have an impact on individuals, their families, and the economy. The annual economic costs associated with dementia are about US dollar 1 trillion, with informal carers providing around 50% of the care [11]. The statistics of dementia worldwide in terms of the 'years lost' with respect to cognitive decline are given in Figure 1.1. Both the percentage of increase of the years lost and the rate of increase of the years lost related to dementia shows a positive climb.

Dementia is closely linked to the accumulation of neurodegenerative proteins in the brain. Neurodegenerative proteins, such as amyloid $\beta$ and tau, can build up in the brain over time, causing damage to brain cells and leading to cognitive impairment and other symptoms associated with dementia. In Alzheimer's disease, for example, amyloid $\beta$ proteins form plaques outside of brain cells, while tau proteins form tangles inside brain cells,

13

both of which contribute to the destruction of brain tissue and the development of dementia. In healthy individuals, the tau proteins are important to maintain the structure and stability of the microtubules. However, in diseased individuals, tau gets hyperphosphorylated, leading to neurofibrillary tangles. These neurofibrillary tangles interfere with cell signaling and are responsible for the cognitive decline and memory loss characteristic of Alzheimer's disease [12]. Tauopathies refer to diseases caused by the abundant tau inclusions in the brain [13]. Other forms of dementia, such as frontotemporal dementia and Lewy body dementia, are also associated with accumulating specific neurodegenerative proteins in the brain. Understanding the role of neurodegenerative proteins in the development of dementia is an active area of research, and new treatments are being developed that target these proteins in an effort to slow or prevent the progression of the disease. Several biophysical techniques are used to characterize neurodegenerative proteins like amyloid $\beta$, $\alpha$-synuclein, and tau proteins. These techniques allow researchers to study the proteins' structure, stability, and interactions, which can provide insights into their role in disease development. Some common biophysical techniques used to study amyloid and other neurodegenerative proteins include X-ray crystallography, Circular Dichroism (CD), NMR spectroscopy, Atomic force microscopy (AFM), etc [14, 15, 16, 17]. With the advent of the new generation supercomputers and with faster algorithms molecular dynamics (MD) simulations have also emerged as an important tool to study the aggregation of the neurodegenerative proteins. The simulations provide a complete atomic-level description of the behavior of biomolecules like proteins, with high temporal resolution. Advances in simulation technology, accuracy, and accessibility, as well as the availability of more experimental data on biomolecules, have made biomolecular simulation more attractive to experimentalists, especially in the field of neuroscience, but not exclusively. Research on Alzheimer's disease was majorly focused on the amyloid beta peptide but due to the failures of the amyloid beta targeting treatment in clinical trials, tau proteins are getting a

lot of attention from the researchers [18]. With the structures of the tau polymorphs being available through cryo-electron microscopy, one can get the near-atomic resolution of the tau structures being responsible for causing a series of neurodegenerative diseases collectively called tauopathies [19]. The major tau polymorphs are termed paired helical filaments (PHFs) and the minority structures are straight filaments (SFs). Both PHFs and SFs are considered pathological structures, as they are associated with the degeneration of neurons and cognitive decline. Tau filaments have similar structural characteristics to amyloid, with extended beta-sheets along the helical axis of the filaments [20]. Filamentous tau inclusions lead to a number of other neurodegenerative diseases, including Pick's disease (PiD), progressive supranuclear palsy (PSP), corticobasal degeneration (CBD), chronic traumatic encephalopathy (CTE), globular glial tauopathy (GGT) and argyrophilic grain disease (AGD) [21].

## 1.2 Neurodegenerative Diseases

Most of the neurodegenerative diseases are characterized by the aggregation of misfolded proteins such as amyloid-$\beta$ and tau in Alzheimer's disease, $\alpha$-synuclein in Parkinson's disease, and TAR DNA-binding protein 43 in amyotrophic lateral sclerosis. Moreover, the tau aggregation cause a series of diseases combinedly known as tauopathies.

Here are a few examples of neurodegenerative diseases and the proteins associated with their aggregation:

- Alzheimer's disease (AD): In AD, amyloid $\beta$ protein accumulates outside neurons in the form of plaques, and tau protein forms tangles inside neurons. These aggregates disrupt the normal functioning of neurons and contribute to cognitive decline and memory loss [22, 23].

- Parkinson's disease (PD): PD is characterized by the loss of dopamine-producing

neurons in the brain. It is associated with the aggregation of alpha-synuclein protein, which forms Lewy bodies. These aggregates impair the normal release and transmission of dopamine, leading to the motor symptoms observed in PD [24].

- Huntington's disease (HD): HD is caused by a mutation in the huntingtin gene, which results in the production of a mutant huntingtin protein [25, 26]. The mutant huntington protein aggregates in neurons, particularly in the basal ganglia. These aggregates disrupt cellular processes and lead to the progressive loss of motor control, cognitive decline, and psychiatric symptoms [27].

- Amyotrophic lateral sclerosis (ALS): ALS involves the degeneration of motor neurons, which control voluntary muscle movement. In some cases of ALS, an abnormal form of superoxide dismutase 1 (SOD1) protein aggregates in motor neurons. This aggregation leads to neuronal dysfunction and eventual cell death [28].

## 1.3   Role of lipid bilayers in the pathogenesis of neurodegenerative diseases

The cell membrane is known to play an important role in the pathogenesis of Alzheimer's disease and dementia [29]. As the cell membrane is the interface between the cell and its environment, it is responsible for a number of critical cellular processes, including signal transduction, ion transport, and energy metabolism. There are several ways in which the cell membrane can contribute to the development and progression of Alzheimer's disease and dementia, such as oxidative stress and tau phosphorylation. For example, the cell membrane can regulate tau phosphorylation by affecting the activity of the enzymes responsible for phosphorylating tau, or this can affect a number of cellular processes that are involved in the pathogenesis of Alzheimer's disease and dementia, including synaptic plasticity and energy metabolism [30, 31]. The study of the interaction of the tau structures

and the model lipid membranes leads us to understand tau pathogenesis. Strodel group has extensively studied the effect of the amyloid beta structures in lipid membrane degradation and the neuronal membrane damage caused by the amyloid beta structures using molecular dynamics simulations [23, 32, 33]. But the studies related to the tau proteins and lipid membranes are scarce and molecular dynamics simulations can provide a wealth of information related to the tau mediated cell toxicity [34]. The exact mechanisms of how the accumulation of abnormal tau proteins leads to Alzheimer's disease are not yet fully understood. Current research focuses on understanding the factors that contribute to the formation of tau protein aggregates and developing new treatments that can target these processes to slow or stop the progression of the disease [35]. The critical study is to understand the molecular mechanisms that govern the tau interaction with the lipid bilayers. The starting configurations of the proteins with the lipid membranes are modeled using the force field parameters pre-parameterized through quantum mechanical calculations. Both the conventional molecular dynamics simulations and the enhanced sampling techniques (like metadynamics, hamiltonian replica exchange molecular dynamics) are carried out to deduce the important interactions governing the binding with the lipid membranes [32]. As the simulations are CPU/GPU extensive, machine learning (ML) techniques are also used in addition to the molecular dynamics simulations to accelerate and enhance the sampling of conformational space or to identify important features in the large datasets derived from the molecular dynamics simulations [36, 37]. In molecular dynamics simulations of the neurodegenerative proteins with lipid membranes, it is important to include the lipid components that are relevant to the brain membrane composition. The brain membrane is mainly composed of phospholipids, with the most abundant ones being phosphatidylcholine (PC), phosphatidylethanolamine (PE), and sphingomyelin (SM). In addition to these major phospholipids, the brain membrane also contains cholesterol, which is known to play an important role in modulating the fluidity and stability of the membrane [38]. Therefore,

including cholesterol in the lipid membrane model is also important for simulating the interactions between the neurodegenerative proteins and the membrane. Another important lipid component to consider in the simulations is the lipid headgroup charge. The brain membrane has an overall negative charge due to the presence of phosphatidylserine (PS) and phosphatidylinositol (PI) lipids. These negatively charged headgroups can affect the electrostatic interactions between the tau protein and the membrane, and their inclusion in the simulation can provide a more accurate representation of the system. Finally, it is also important to consider the length and saturation of the acyl chains of the phospholipids. The length and saturation of the acyl chains can affect the fluidity and order of the membrane, which can in turn affect the interactions between tau protein and the membrane. Therefore, it is important to include different types of phospholipids with varying acyl chain lengths and saturation levels in the simulation. The molecular dynamics simulations provide a powerful tool for understanding the properties of lipid bilayers at a molecular level and can be used to study a wide range of biophysical phenomena [39]. For example, the area per lipid of the lipid bilayers defines the membrane fluidity, bending modulus of the lipid bilayers is important to understand the effects of the curvature and morphology of the membrane. These key properties of the lipid bilayers are calculated for both the true systems with pure bilayers and for the systems comprising the neurodegenerative proteins with lipid bilayers [40]. The comparison between the control simulations and the true systems will help understand the effect of the tau incorporation over the lipid bilayers. The expected results of the study of the molecular dynamics simulations of the neurodegenerative proteins with lipid membranes can vary depending on the specific research question and methodology used. However, some potential outcomes of such a study could include structural insights. The simulations can provide valuable information about the structural dynamics of the neurodegenerative proteins in interaction with different lipid membranes. This can include insights into the conformational changes and flexibility of such proteins in response to the

lipid environment. The simulations can help identify specific lipid molecules that interact strongly with the tau protein, and the amino acid residues involved in these interactions. This can provide insights into the specific lipid components that play a role in modulating the function of tau protein in vivo. The simulations can also provide information on the thermodynamic stability of the tau protein-lipid complexes and the strength of the tau protein-lipid interactions. This can help identify factors that contribute to the stability of tau protein-lipid complexes and potentially guide the design of small molecule inhibitors that target these interactions [41]. The simulations can provide a framework for understanding the dynamic nature of tau-lipid interactions in vivo, and help generate hypotheses about the role of these interactions in modulating tau function and aggregation. Overall, the study of molecular dynamics simulations of tau proteins with lipid membranes has the potential to provide valuable insights into the structure and function of tau protein in relation to lipid membranes and to guide the development of therapeutic strategies for tauopathies. The thesis will yield an important understanding of tau pathogenesis over a wide series of lipid components that comprise the neuronal cell membrane. It will help to understand the tau interactions with the specific lipid components that can hasten the designing of the AD targeted drugs for the tau proteins. Ultimately, the research will help us understand Alzheimer's disease and dementia better.

## 1.4    Molecular Dynamics Simulations

Molecular dynamics (MD) simulations are a computational approach in which the equations of motions are solved using Newton's laws and the trajectories generated are used to extract macroscopic variables. MD simulations aim to solve the numerical solutions to many-body potentials which are otherwise difficult to solve analytically. MD simulations allow a hypothetical numerical analysis of the system of interest. For example, extreme
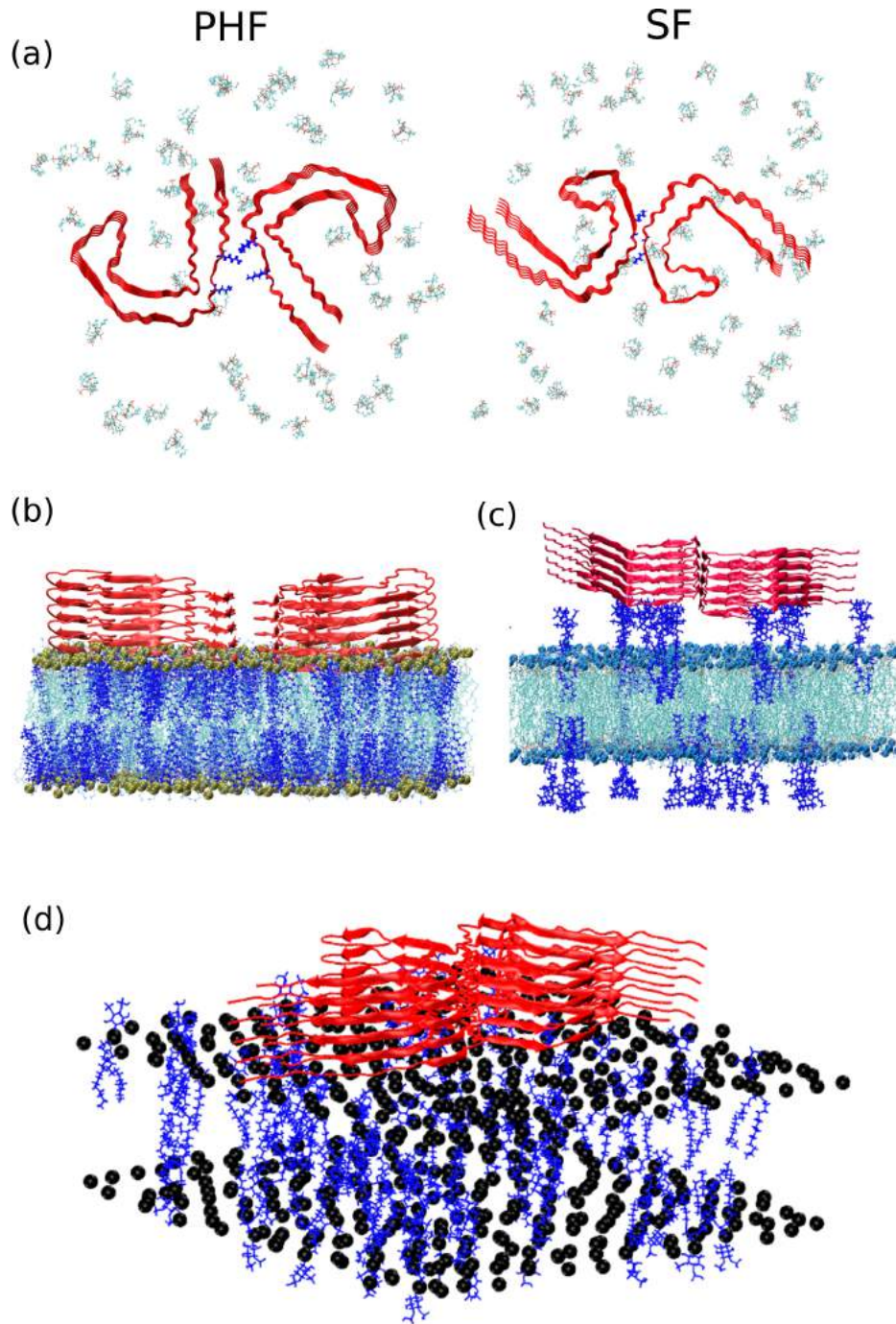
Figure 1.2: Shown in (a) are the cryo-EM structures of the tau polymorphs paired helical filaments (PHFs) and straight filaments (SFs) used as the starting structures for MD simulations. (b) and (c) are the starting configurations of the tau fibril and lipid bilayers with cholesterol and GM1 lipids shown in blue line representation respectively. (d) is the starting configuration of the tau fibrils with the PI lipids. The phosphorus head groups are shown in black VDW spheres.

20

conditions such as high temperature and pressure can be simulated at unprecedented level of accuracy which is otherwise impossible in a physical laboratory. The caveat lies in the choice of the numerical model used to define the system. Yet MD simulations have emerged as a powerful computational tool for studying the behavior and interactions of biomolecules at the atomic level. By applying the principles of classical mechanics and statistical thermodynamics, MD simulations are extensively used to investigate the dynamic behavior of complex biological systems, such as proteins, nucleic acids, and membranes.

MD simulations involve the integration of Newton's equations of motion to track the positions and velocities of individual atoms over time. By simulating the interactions between atoms using force fields that describe the potential energy landscape, MD simulations provide insights into the structural changes, conformational dynamics, and thermodynamic properties of biomolecules.

### 1.4.1 Verlet Algortithm

The important aspects of the MD simulations are the modeling of the interparticle interactions, calculation of the forces and energies from the model and integrating the equations of motion. The simplest way to integrate the equations of motion is using the Taylor series. The position of a particle at (t+$\Delta$t) is expressed as the following equation neglecting the higher order terms.

$$\mathbf{x}(t + \Delta t) = \mathbf{x}(t) + \mathbf{v}(t)\Delta t + \frac{1}{2}\mathbf{a}(t)(\Delta t)^2 \tag{1.1}$$

Similarly the position of the particle at (t-$\Delta$t) can be expressed as

$$\mathbf{x}(t - \Delta t) = \mathbf{x}(t) - \mathbf{v}(t)\Delta t + \frac{1}{2}\mathbf{a}(t)(\Delta t)^2 \tag{1.2}$$

Note that $v(t)$ and $a(t)$ are the first order and second order time derivatives of the position respectively. Adding the equations 1.1 and 1.2 we obtain,

$$\mathbf{x}(t + \Delta t) + \mathbf{x}(t - \Delta t) = 2\mathbf{x}(t) + \mathbf{a}(t)(\Delta t)^2 \tag{1.3}$$

which after rearrangement becomes

$$\mathbf{x}(t + \Delta t) = 2\mathbf{x}(t) - \mathbf{x}(t - \Delta t) + \mathbf{a}(t)(\Delta t)^2 \tag{1.4}$$

This becomes the numerical solution known as the Verlet algorithm. The system is propagated through a timestep of $\Delta t$. As shown above the Verlet algorithm only generates positions. The velocities can be constructed at any point in the trajectory through the centered difference formula

$$\mathbf{v}(t) = \frac{\mathbf{x}(t + \Delta t) - \mathbf{x}(t - \Delta t)}{2\Delta t} \tag{1.5}$$

## 1.4.2 Velocity Verlet Algorithm

Velocity Verlet algorithm is an improved integrator of the molecular dynamics simulations which takes into account the velocities of the particles into account. Velocities are important in the simulation trajectories because they are necessary to calculate the kinetic energies of the particles at every timestep.

$$\mathbf{x}(t + \Delta t) = \mathbf{x}(t) + \mathbf{v}(t)\,\Delta t + \tfrac{1}{2}\,\mathbf{a}(t)\Delta t^2,$$
$$\mathbf{v}(t + \Delta t) = \mathbf{v}(t) + \frac{\mathbf{a}(t) + \mathbf{a}(t + \Delta t)}{2}\Delta t. \tag{1.6}$$

Velocity Verlet and Verlet algorithm forms the basis of the numerical integration required to calculate the position and velocities at each timestep in the molecular dynamics simulations. These algorithms calculate the forces between particles, updates their velocities based on these forces, and then updates their positions using the updated velocities. This process is repeated for each time step, enabling the simulation to explore the dynamics and behavior of the system over a desired time period.

### 1.4.3 Force Fields

The force field is a mathematical model that describes the interatomic interactions and energy terms governing the behavior of particles in the system. It provides a set of parameters, potential energy functions, and rules to calculate forces acting on particles based on their positions and velocities in MD simulations. The force field parameters are chosen from the experimental observations or through quantum mechanical calculations. The total energy can be expressed as

$$E_{total} = \sum_{bond} k_i^{bonds}(r_i - r_0)^2 + \sum_{angles} k_i^{angle}(\theta_i - \theta_0)^2 + \sum_{dihedrals} k_i^{dihed}[1 + cos(n_i\phi_i + \delta_i)]+$$
$$\left\{ \sum_i \sum_{j \neq i} 4\epsilon_{ij}[(\frac{\sigma_{ij}}{r_{ij}})^{12} - \frac{\sigma_{ij}}{r_{ij}}^6] + \sum_i \sum_{j \neq i} \frac{q_i q_j}{\epsilon r_{ij}} \right\}$$
$$(1.7)$$

The first two terms in the additive potential are used to model the interaction between the bonded atoms, with the quadratic functions that do not allow bond breaking. The third term stands for the dihedral potential involving multiple minima separated by energy barriers of varying heights. These first three terms model the intermolecular energy for the bonded atoms. The last two terms define the nonbonded interactions and the electrostatic interaction between the particles. Interatomic interactions between pairs of atoms are approximated by the 12-6 Lennard-Jones potential which is the fourth term. The Lennard-Jones potential represents the attractive and repulsive forces between pairs of atoms with the equilibrium interatomic van der Waals (VDW) distance of $\sigma_{ij}$ and the potential well depth of $\epsilon_{ij}$. The last term is the Coulombic potential which describes the electrostatic interactions between pairs of atoms which are represented as point charges

The molecular dynamics simulations hence can be described using a simple workflow given below,
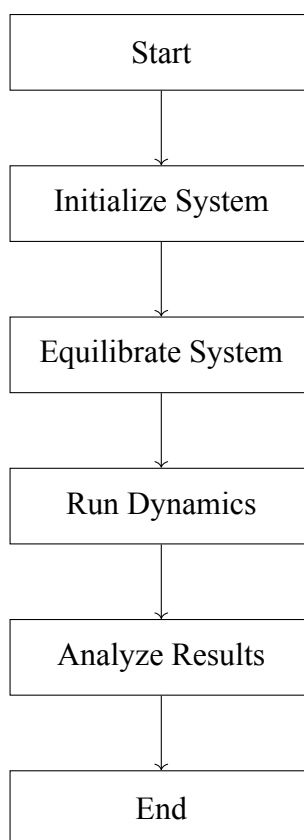
## 1.5 Free energy Calculations

Free energy calculations using MD simulations are a powerful tool to extract the energetics of a system. They provide valuable insights into various processes such as protein-ligand binding, protein conformational changes, and protein-protein interactions. The energetics give us hints whether a process would be spontaneous or not, whether a solute molecule is hydrophilic or hydrophobic. There are several methods available for the free energy calculations, namely:

- Thermodynamic Integration (TI): This method involves perturbing a system from a known reference state to the target state while collecting the potential energy differences along the perturbation pathway. By integrating these energy differences, the free energy change between the two states can be obtained [42].

- Umbrella Sampling: In this method, the potential of mean force (PMF) along a reaction coordinate is calculated by restraining the system at different positions along the coordinate and sampling the potential energy landscape. By reweighting the sampled data, the PMF and the associated free energy profile can be determined [43].

- Metadynamics: Metadynamics is a biased sampling method that enhances the sampling of rare events by adding a history-dependent bias potential. It constructs a free energy landscape by filling the free energy basins and allows the exploration of multiple states or reaction pathways [44].

- Alchemical Free Energy Methods: These methods involve transforming the system from one state to another by gradually changing the parameters, such as the partial charges or force constants. By using statistical mechanical theories and collecting data from multiple simulations, the free energy difference between the two states can be calculated [45].

- Potential of Mean Force (PMF) calculations: PMF calculations involve calculating the potential of mean force along a reaction coordinate or a specific property, such as distance or angle. It provides insights into the energetic barriers and stability of different states or transitions [46].

It's important to note that free energy calculations require careful setup, extensive sampling, and rigorous analysis to obtain accurate results. These methods often involve running multiple simulations, performing extensive data analysis, and applying advanced techniques such as reweighting, bootstrapping, binning, and convergence analysis. Various software packages are available for performing free energy calculations, including GROMACS, AMBER, NAMD, and CHARMM, which provide tools and utilities specifically designed for these calculations [47, 48, 49, 50]. These packages often come with tutorials, documenta-

tion, and user communities to assist in setting up and analyzing free energy simulations.

## 1.6  Choosing the Initial Conditions

Choosing the initial conditions for molecular dynamics simulations is a critical step that directly influences the outcome and reliability of the simulation results. The initial conditions encompass various aspects, including the selection of the system size, the choice of force field parameters, the assignment of atomic positions and velocities, and the inclusion of solvent molecules and ions if relevant.

The system size should be carefully determined to capture the desired level of detail and adequately represent the biological or chemical system of interest. This involves deciding on the number of atoms, the size and shape of the simulation box, and the appropriate boundary conditions.

Selecting an appropriate force field is crucial for accurately describing the interactions between atoms and molecules in the system. Force field parameters, such as bond lengths, angles, dihedral angles, and nonbonded interactions, need to be carefully assigned based on the specific molecular entities involved.

Assigning initial atomic positions and velocities requires careful consideration of the starting conformation. This can involve obtaining experimental structures, performing homology modeling, or using other computational techniques to generate an appropriate starting structure.

If the system includes solvent molecules, they need to be added to mimic the experimental environment. Solvent molecules can contribute to the stability and behavior of the system, affecting properties such as solvation, hydration, and transport.

Incorporating ions into the simulation can be essential for replicating experimental conditions, maintaining charge neutrality, and accounting for the presence of counterions or

cofactors.

Once the initial conditions are defined, an energy minimization step is typically performed to relax the system and remove any steric clashes or unfavorable interactions. This ensures that the system starts in a physically realistic state and minimizes artificial forces.

Overall, choosing the initial conditions for molecular dynamics simulations requires a thorough understanding of the system being studied and a careful balance between accuracy and computational efficiency. It is an iterative process that may involve trial and error, parameter optimization, and validation against experimental data to ensure reliable and meaningful simulations.

## 1.7   Coarse Grained simulations

Usually the starting configurations of the molecular dynamics simulations include the all-atom representation of the systems of interest. In the all atom representation the individual atoms are explicitly represented, and their interactions are considered in the simulation. Each atom is treated as a separate particle, and the forces between atoms are calculated based on their positions and potential energy functions. Coarse-grained simulations refer to a specific approach in which the level of detail and resolution of the system is reduced compared to atomistic simulations. In this context, the biomolecular system, such as proteins, nucleic acids, or lipid membranes, is represented by larger, coarse-grained particles or beads [51].

In a coarse-grained model, multiple atoms are grouped together to form a single interaction site or bead. This grouping is based on physical or chemical properties, spatial proximity, or functional significance. By doing so, the computational complexity of the simulation is significantly reduced, allowing longer time scales and larger systems to be studied compared to atomistic simulations.

Coarse-grained models aim to capture the essential features and behavior of biomolecular systems while neglecting fine details. The interactions between coarse-grained particles are typically described using effective potentials or force fields that are derived from more detailed atomistic simulations or experimental data. The parameters of the force field are often optimized to reproduce specific properties or experimental observables.

Coarse-grained simulations in biomolecular molecular dynamics have been widely used to investigate various biological processes and phenomena, such as protein folding, membrane dynamics, protein-protein interactions, and self-assembly of biomolecular complexes [52]. Coarse-grained simulations are particularly useful for studying longer time scale phenomena and larger length scales, such as protein folding, self-assembly processes, or membrane dynamics, which involve collective behavior and large macromolecular systems. These simulations provide valuable insights into the collective behavior, dynamics, and functional mechanisms of biomolecules and allow for the study of larger and longer time scale processes that are otherwise challenging with atomistic simulations.

# Chapter 2

# Helix-Coil Transition and Conformational Deformity in A$\beta_{42}$-monomer: A Case Study Using the Zn$^{2+}$ Cation

The aggregation of amyloid beta peptides and its progression is regarded as the primary cause for Alzheimer's disease (AD) [53, 54]. AD is one of the most common causes of Dementia which imparts a considerable decline in the cognitive processes of an individual [55, 56]. Amyloid-$\beta$ peptides and their aggregation is deemed as an important problem for the NMR and molecular dynamics (MD) studies [57]. Owing to their hitherto dis-orderedness they are classified as intrinsically disordered proteins or IDPs [58]. The self-aggregation of the amyloid-$\beta$ is triggered as a result of the amyloid precursor protein (APP) being sequentially cleaved by the $\beta$- and $\gamma$-secretase. The AD is characterised by the deposition of amyloid fibrils which are densely packed and aggregated peptide oligomers of the 42 ($A\beta_{42}$) and 40 ($A\beta_{40}$) residue monomers. It has been found that the 42 residue monomer is more prone towards aggregation and hence more toxic to the brain, and also the dominant species in the fibrils that are deposited in the brain.

There is a high prevalence of metal ions ( Fe$^{2+}$, Zn$^{2+}$, Cu$^{2+}$) in the fibrils that are found in the dementia affected parts in the brain [59, 60, 61]. Many studies have reported the interaction of the metal ions with the A$\beta$ monomer and fibrils. These metal ions are the potential hidden actors in the interaction of the APP and the fibril oligomers. Previous studies have found that the H6, H13 and H14 regions are the binding junctions at the N-terminal region to accommodate the Zn$^{2+}$ ion [62, 63, 64, 65, 66]. Structural models of these metal bound peptides are important to understand the fibrillation kinetics and the structural

changes involved. Experiments (such as FRET, dynamic light scattering, mass spectrometry, atomic force microscopy) at times prove to be important in predicting the structural changes of the oligomers involved in the fibrillation [14, 15, 16, 17]. But with the advent of highly effective sampling methods along with the increase of available computational resources, classical MD simulations have provided deep insights on the fibril aggregation mechanism [67, 68, 23, 69]. In many cases short fragments of K16 to E22 or G33 to A42 is modelled to study the aggregation mechanism of the A$\beta$ monomer [70, 71]. In this study, we have taken the entire A$\beta$ monomer with and without Zn$^{2+}$ and estimated the potential of mean force (PMF) for the unfolding of the entire peptide from $\alpha$-helix to coil. Keten and coworkers have analysed the mechanical unfolding of a series of alpha-helical and beta-helical proteins through a number of steered molecular dynamics (SMD) simulations using a variety of pull-rates [72, 73]. In our study, we have pulled the monomer(A$\beta$-42) $\alpha$-helix to the unfolded state to look at the mechanical robustness of the helix monomer. This also provides information of the energetics involved in the folding of the A$\beta$ monomer with the addition of cations (Zn$^{2+}$, Cu$^{2+}$, Fe$^{2+}$ etc).

## 2.1 Methodology and simulation details

The initial structure for the MD simulations was taken from the PDB-id 1Z0Q. The N- and C-terminals are free amino (NH$_3^+$) and carboxyl (COO$^-$) groups and hence have a net charge of -3e. The Zinc ion was initially positioned nearby the Zn-binding residues (H6, H13 and H14). The proteins were solvated in a cubic box using the CHARMM-GUI [74, 75, 76] interface using the parameters from CHARMM-36m [77] force field and TIP3P water model. Potassium ions are added to neutralize the simulation box. The LINCS [78] algorithm was used to constrain the bonds involving hydrogen atoms. The particle mesh Ewald summation [79] was used to describe the long-range interactions with a cutoff of 1.2 nm. For the

van der Waals forces, a cutoff of 1.2 nm was used. The temperature and pressure were controlled using the Nosé-Hoover thermostat[80] and Parrinello-Rahman barostat[81] respectively. Initially, the systems were energy minimized using the method of steepest descent. A timestep of 2.0 fs was used for the simulations. The velocities and coordinates were stored at an interval of 10.0 ps. The peptide was simulated with and without $Zn^{2+}$ ion, starting from four independent configurations. The initial configurations were obtained by simulating the peptide at four different temperatures (400 K, 310 K, 350 K and 380 K) and 1 atmosphere pressure for 10 ns. The simulations were then extended for another 1 $\mu s$ in isothermal-isobaric (constant NPT) ensemble at 310 K and 1 atmosphere pressure. These simulations are termed as sim1, sim2, sim3 and sim4. We have also carried out simulations on another configuration of the multiple configurations deposited in the pdb 1Z0Q, at 310 K, which is referred to as sim5. The cumulative sampling of the equilibrium simulations add up to 9 $\mu$s. The details of the simulations are given in the table 2.1.

The initial equilibration was carried out with the restraints applied on the protein molecules. All the systems were simulated using GROMACS MD engine (5.1.4 version) [47, 82]. The images were rendered using VMD software [83]. To elucidate the changes in the secondary structure content, the DSSP utility in *gmx* was used.

To study the helix to coil transition, we have stretched the A$\beta$ peptide of 42 residues to a coil structure from the $\alpha$-helix. The box dimensions were chosen in such a way to avoid interactions between the periodic images even when the peptide was fully stretched. The box dimensions were taken to be 31.5 nm $\times$ 8.4 nm $\times$ 8.4 nm, with the stretching direction being towards the x-axis. In the first steered MD simulation, the $\alpha$-helix was pulled to the coil structure and the extent of the unfolding was scrutinized using DSSP. In all the pull simulation studies the pull rate and the force constant of the pull spring was 0.2 nm per nanosecond and $10^5$ $kJ/mol/nm^2$ respectively. DSSP algorithm was used to analyse the extent of unfolding in the $\alpha$-helix. A complete coil conformation in the DSSP plot points

to the total unfolded state. The peptide was pulled to a completely unfolded state and the umbrella sampling was done taking successive configurations along the collective variable with the equilibration of 10 ns at each window. The spacing between the umbrella sampling was 0.102 nm for the alpha-helices to coil conversion. In this way, about 100 configurations across the reaction coordinate were generated to account for the entire length of the peptide.

The potential of mean force (PMF) was generated taking the pull profiles from all these configurations using the WHAM module of GROMACS. The equilibration at each window varied between 5 ns per window and 10 ns per window. The analysis were done using perl scripting, *gmx* modules and in-house scripts. A total of 3.1 $\mu$s of steered MD and umbrella sampling simulations have been performed.

To elucidate the $Zn^{2+}$ binding in the A$\beta$ monomer, we have pulled the $Zn^{2+}$ away from the solvation shell of the A$\beta$ monomer towards the y-direction using a harmonic force constant of $10^5 \, kJmol^{-1}nm^{-2}$. WHAM is used to extract the PMF from 30 individual windows being placed across the pulling coordinate. The spacing between the umbrella sampling windows was 0.08 nm. The pulling rate was 0.2 nm/ns with the collective variable being chosen as the distance between the residue E-22 and the $Zn^{2+}$ atom. E-22 was chosen to tether the A$\beta$ monomer from the $Zn^{2+}$ cation as it is close to the center-of-mass of the monomer peptide. The WHAM profiles are extracted through the equilibration of 5 ns at each window and subsequent employment of bootstrapping of histograms [84]. Bootstrapping is very efficient and is comparable to the multiple WHAM computations for the PMF calculation[84].

In all the analyses and discussions, the entire peptide of 42 residues is segregated into four regions or zones owing to their differential structural and dynamical characteristics in accordance with the previous studies. The region having residues from $1-16$ (N-terminus) is termed as zone 1, from $17-21$ (central hydrophobic core) is termed as zone 2, $22-29$ (hydrophilic patch) is termed as zone 3 and C-terminus from residues $30-42$ is termed as

Table 2.1: Details of the simulated systems

| | System | Number of Atoms | Box Length (nm) |
|---|---|---|---|
| | sim1 | 35454 | 7.06 |
| | sim2 | 52659 | 8.06 |
| A$\beta$ monomer | sim3 | 52653 | 8.06 |
| | sim4 | 52659 | 8.05 |
| | sim5 | 58395 | 8.35 |
| | sim1 | 35471 | 7.08 |
| A$\beta$ monomer + Zn$^{2+}$ | sim2 | 52658 | 8.07 |
| | sim3 | 52658 | 8.06 |
| | sim4 | 52658 | 8.07 |

zone 4.

## 2.2 Results and discussion

### 2.2.1 Hydrophilicity/hydrophobicity

There have been many theoretical and experimental studies that demonstrates that the Zn$^{2+}$ binds in the N-terminal region with the amino acid residues H6, E11, H13 and H14. These studies conclude that the central hydrophobic core (CHC) plays a major role in the aggregation process leading to oligomerization. It has been found [69] that the presence of the Zn$^{2+}$ decreases the $\beta$-strand content. Another study has demonstrated the change in hydrophobicity of the whole length peptides upon Zn$^{2+}$ binding [85]. The increased hydrophobicity results in the increased interaction among the hydrophobic residues which facilitates aggregation [86, 87, 88, 89].

In this study, we have investigated the effect of Zn$^{2+}$ incorporation in the peptide in 1:1 ratio. The hydrophobicity is probed using the radial distribution function (RDF) of the water oxygen with the of the C-$\alpha$ of the protein shown in the Figure 2.1 which provides the relative probability distribution of the water oxygen around the protein. The results are

33
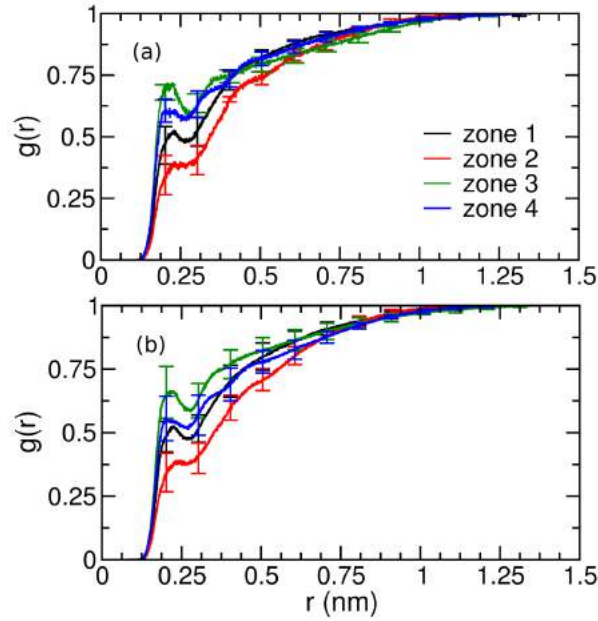
Figure 2.1: The RDFs of two systems across the four different zones for the C-$\alpha$ atoms with water oxygen. (a) for A$\beta$ monomer (b) for A$\beta$ monomer $+$ Zn$^{2+}$

averaged across all the trajectories with and without Zn$^{2+}$. The peptide zones 1, 2, 3 and 4 with and without the Zn$^{2+}$ show differential plots for their relative interactions with the water oxygen, which gives an idea about the relative hydrophobicity or hydrophilicity. The RDFs show differential interaction of various zones; zone 3 (hydrophilic patch between $22 - 29$) shows greater affinity towards the water oxygen and the zone 2 (the hydrophobic core between $17 - 21$) shows least preference towards water. The zone 1 (hydrophilic N-terminal) and zone 4 (hydrophobic C-terminal) shows comparable affinity towards water in the presence and absence of Zn$^{2+}$. Although the RDF peak heights and positions remain consistent, there is a noticeable change in the relative peak intensity differences between zone 1 and zone 4.

Table 2.2: The average number of H-bonds observed across all the trajectories. The standard deviations are given in the parenthesis

| Number of H-bonds | $A\beta$ monomer | $A\beta$ monomer $+$ $Zn^{2+}$ |
|---|---|---|
| intrapeptide | 13.93 (3.32) | 14.89 (3.32) |
| peptide-water | 130.60 (7.76) | 122.38 (7.59) |

## 2.2.2 Hydrogen Bonding

The hydrogen bond is an attractive interaction between a hydrogen atom of a molecule or a molecular fragment $X - H$ in which X is more electronegative than H, and an atom or a group of atoms in the same or a different molecule, in which there is evidence of bond formation. In a strong H bond, the H atom and the acceptor are separated by a distance less than 0.22 nm, and the angle made by the donor, H atom, and the acceptor is within the range $130 - 180°$. The corresponding distance range and angular range are $0.2 - 0.3$ nm and $90 - 180°$, respectively, in a weak hydrogen bond[90]. Thus we have used the weak hydrogen bonding criterion to compare across the results as no strong H-bond is observed in our cases.

The pattern of H-bonding is analyzed across the two representative trajectories with and without $Zn^{2+}$ ion in Figure 2.2. The average number of the intramolecular H bonds in the $A\beta$ monomer system, and the monomer $+$ $Zn^{2+}$ system are 13.93 and 14.89 respectively being averaged out of all the trajectories. However, the number of peptide-water H-bonds shows the opposite trend, with the peptide showing a greater number of H-bonds in the absence of $Zn^{2+}$ ion as shown in table 2.2.

The average number of peptide $-$ water H-bonds in the solution decreases upon the addition of $Zn^{2+}$ cation, due to the increase in the number of intramolecular H-bonds. The increase in the intra-peptide hydrogen bonding is lesser than the decrease in the number of peptide-water hydrogen bonding due to the availability of lesser number of intra-peptide contacts for the hydrogen bond formation. The higher number of intra-peptide hydrogen
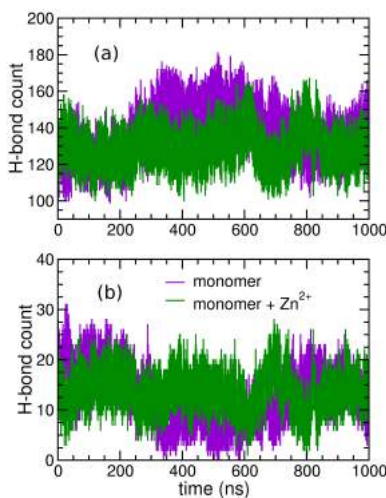
Figure 2.2: The plots for the number of H-bonds observed in the representative trajectories for systems with and without $Zn^{2+}$ ions. (a) peptide – water H-bonds (b) intrapeptide H-bonds.

bonds gives rise to the more favorable interactions within the peptide residues in the presence of the $Zn^{2+}$ ion.

Hence, in the solvent, the $Zn^{2+}$ cation induces more number of intra-peptide H-bonds facilitating the favorable intra-peptide interactions for maintaining the secondary structure, which comes at the cost of reduction in the number of peptide-water H-bonds. Thus $Zn^{2+}$ cation initiates the favorable H-bonded interactions within the peptide, by increasing the favorable interactions to attain a particular secondary structure. The H-bonding profiles in the other trajectories also follow the same trend with the $Zn^{2+}$ cation inducing the relatively higher number of intra – peptide hydrogen bonds and reducing the peptide – water hydrogen bonding.

### 2.2.3 Contact Maps

To explore the structural disparity of the $Zn^{2+}$ bound peptide, we have studied the contact maps for the residue distances. The contact maps elucidate the presence of long-range interactions and the contact probabilities and are shown in Figure 2.3. The presence of

36

$Zn^{2+}$ cation induces the long range interactions between the residues, the most important among them being $H13 - I32$, $F4 - N27$, $I32 - V40$, $Y10 - I31$ and $D7 - K16$. These interactions span major inter-zonal contacts between the core and the terminal residues. Hence, it is evident that the $Zn^{2+}$ cation introduces more inter-zonal side chain contacts and induces more long-ranged interactions leading to a rather folded conformation. This is also consistent with the previous reported results [85].
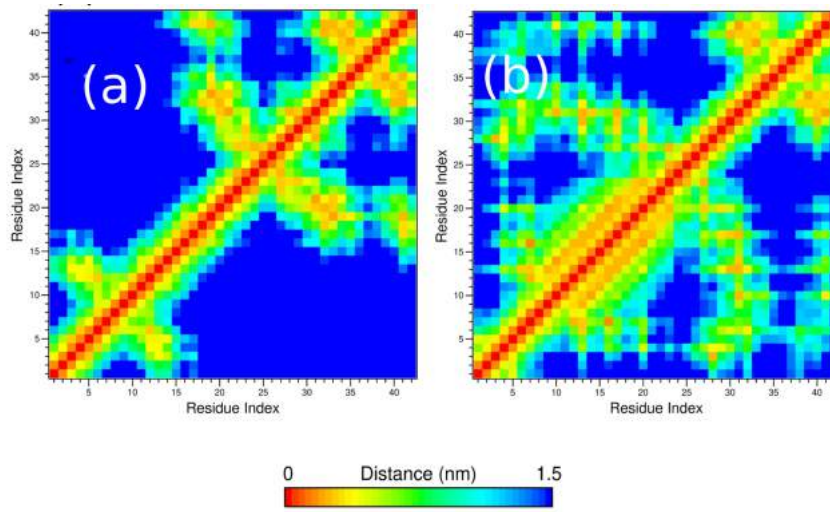


Figure 2.3: The representative contact maps associated with the two trajectories. (a) A$\beta$ monomer and (b) A$\beta$ monomer + $Zn^{2+}$ ion.

Table 2.3: Average percentage of secondary structure content by averaging across all the trajectories.

| | $A\beta_{42}$ | $A\beta_{42} + Zn^{2+}$ | $A\beta_{42}$ | $A\beta_{42} + Zn^{2+}$ | $A\beta_{42}$ | $A\beta_{42} + Zn^{2+}$ |
|---|---|---|---|---|---|---|
| | | overall | | 0-100ns | | 900-1000ns |
| coil | 34.78 | 34.12 | 26.25 | 32.63 | 43.78 | 35.84 |
| $\beta$-sheet | 1.67 | 0.50 | 0.64 | 0.37 | 2.15 | 1.25 |
| $\beta$-bridge | 1.80 | 1.15 | 2.42 | 0.18 | 3.24 | 3.04 |
| $\alpha$-helix | 6.00 | 19.64 | 26.00 | 21.16 | 0.17 | 18.74 |
| 3-10-helix | 0.57 | 0.90 | 1.44 | 0.22 | 0.21 | 1.88 |
| turn | 9.67 | 13.00 | 13.26 | 10.67 | 6.5 | 14.00 |

### 2.2.4 DSSP analysis

The presence of the $Zn^{2+}$ ion can alter the secondary structure content which has been traced by the direct secondary structure prediction algorithm. The table 2.3 shows the average secondary structure content of the two trajectories in two intervals, one at the beginning and another at the end of the simulation. The average over all the 1 $\mu$s simulations is also shown in the table.

Overall the average $\alpha$-helix content is increased and the $\beta$-sheet, $\beta$-bridge content is decreased with the addition of the $Zn^{2+}$. The increase in the overall $\alpha$-helix content is balanced by the turn content. The decrease of the $\beta$-sheet, $\alpha$ helix and $\beta$-bridge content of the secondary structure compensates for the increase in the coil structure in the first 100 ns for the $A\beta$ monomer system with the $Zn^{2+}$ ion. For the final 100 ns the $\alpha$-helix content predominates over the other secondary structures with the inclusion of $Zn^{2+}$. It can be said that there is a strong penchant for the coil conformations in all the trajectories. The $\beta$-sheet, $\beta$-bridge and 3-10 helix strutures are less pronounced. The secondary structure propensity of residues for the two trajectories over the entire 1 $\mu$s is shown in Figure 2.4. The top plot shows the DSSP timeline for the trajectory without the $Zn^{2+}$ cation. In case of the $A\beta$ monomer, the beta sheet region is steadily observed at the C-terminal region. There is
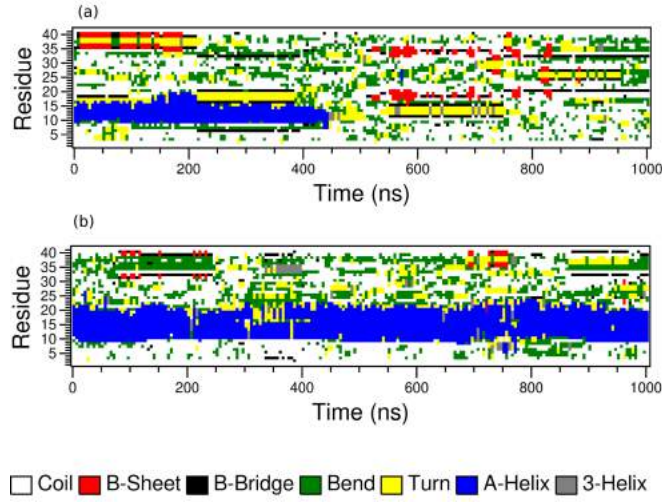
Figure 2.4: The representative timeline of DSSP plots for (a) A$\beta$ monomer and (b) A$\beta$ monomer + Zn$^{2+}$.

also an increase in the alpha helix content with time between the residues $10 - 20$ in the N-terminal and the CHC region. In the trajectory of the A$\beta$ monomer with Zn$^{2+}$, there are some sporadic accounts of beta sheet at the C-terminal zones along with the overall predominance of the $\alpha$-helix. The $\alpha$-helix is found throughout the microsecond run in the presence of the Zn$^{2+}$ cation. Previous studies on the metal amyloid interactions at a different ion concentration have found that the fraction of the $\beta$-sheet content decreases under the influence of the metal ions [91, 92]. The improved stability of the $\alpha$-helix with the Zn$^{2+}$ ion has been shown elsewhere that Zn$^{2+}$ cation can increase the propensity of an existing $\alpha$-helix conformation in Clavanin A peptide[93].

The representative structures generated from the simulations are shown in Figure 2.5. In case of the A$\beta$ monomer + Zn$^{2+}$, there is a clear predominance of $\alpha$-helix, 3-10 helix, $\pi$-helix and coil, but without the Zn$^{2+}$ there is $\beta$-sheet, coil and $\alpha$-helix. The helix structure of the A$\beta$ monomer + Zn$^{2+}$ is maintained both at 500 ns and 1 $\mu$s.
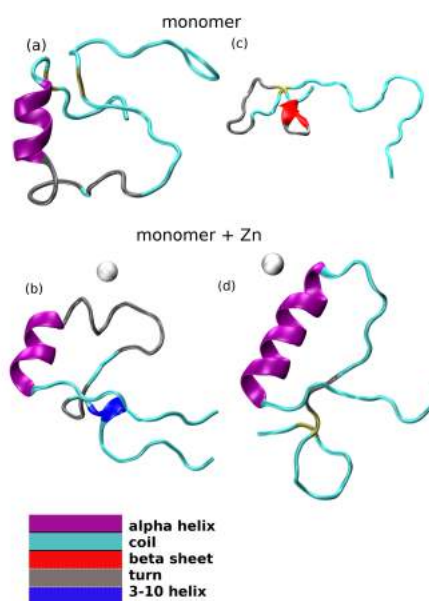
Figure 2.5: The structures (a) and (b) are the peptide configurations obtained at the 500 ns and structures (c) and (d) represent the configurations at $1\mu$s.

## 2.2.5 Internal Rotational Dynamics

The influence of $Zn^{2+}$ cation on the structure and dynamics of the protein is significant as discussed earlier. Experimentally, it is found that the $Zn^{2+}$ binding sites are toward the N-terminal side. However, $Zn^{2+}$ ion exerts an appreciable influence over the entire stretch of the peptide. To examine the dynamical fluctuations, we have analysed the mean internal correlation time for all the backbone NH dipoles of the peptide residues. The internal motions of the protein backbone can be investigated by the NMR relaxation parameters. The spin relaxation rates have been used to validate the molecular dynamics (MD) simulations. The analysis is executed by separating the internal rotational fluctuations from the overall rotational fluctuations. It has been assumed that the motions related to the overall Brownian fluctuations are independent of the internal conformational fluctuations. The rotational correlation function is written as

$$C(t) = C_i(t) \cdot C_o(t) \qquad (2.1)$$

where $C_i(t)$ is the internal rotational correlation function and $C_o(t)$ is the overall rotational correlation function. The internal rotation is removed from the overall rotation by using the *gmx* fit option. The internal rotational correlation functions are then expressed as the dipole correlation functions of the NH bond vectors across the trajectory.

$$C_i(t) = \langle P_2(\hat{\mu}_i(t + \tau) \cdot \hat{\mu}_i(\tau)) \rangle \qquad (2.2)$$

where $P_2(x) = \frac{1}{2}(3x^2 - 1)$ is the second order Legendre polynomial. $\tau$ is the time step for the computation of the correlation function and the angular brackets denote the average over the trajectory. The average lifetime is calculated by integrating over the entire time period using the formula,

$$\langle \tau_e \rangle = \int_0^\infty C_i(t) \, dt \qquad (2.3)$$

The evaluated $\langle \tau_e \rangle$ may be used to link the internal peptide backbone correlation time to the fluctuations in the peptide backbone.

The mean rotational correlation time for the residual backbone NH dipole moment are shown in Figure 2.6. From the Figure, it can be noticed that the difference between the correlation time is more pronounced for the residues G-9 to F-19 and between I-31 and M-35 residues. This observation supports the earlier reports that conclude that the CHC (zone 2) and zone 3 are the aggregation prone segments in the full length A$\beta$ peptide[94]. A$\beta$ $(29 - 42)$ and the region, K-16 to E-22 are the aggregation prone regions which are independently capable of aggregation [95, 96].

The mean lifetime (averaged over all the trajectories) with and without the Zn$^{2+}$ cation are found to be 0.52 ns and 0.47 ns respectively. The Zn$^{2+}$ cation not only imparts local

changes in the residue binding site, but also alters the overall mean peptide internal corre-

lation time. One can deduce that the changes in the H-bond network is responsible for the

considerable changes observed in the backbone rotational correlation lifetimes.
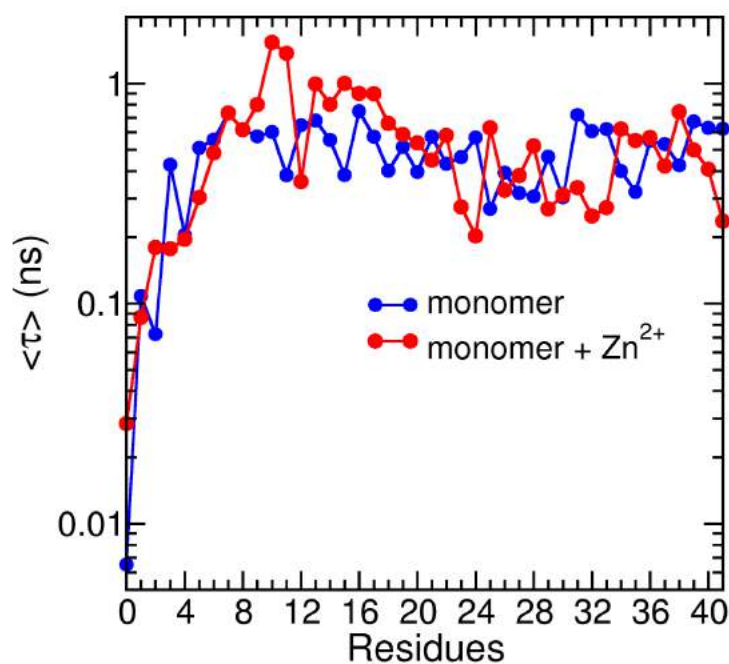


Figure 2.6: The mean rotational correlation time for each of the residual backbone -NH dipole moment obtained by averaging over all the trajectories.

### 2.2.6  Steered Molecular Dynamics and End-to-End Pull

The potential of mean force (PMF) is the free energy computed across the specified degree of freedom with the other degrees of freedom being Boltzmann-averaged and is exclusive of that specific reaction coordinate. Thus PMF succinctly reveals the free energy preferences in many biologically relevant processes such as stretching the proteins, RNA, DNA [97, 98, 99, 100, 101], pulling small molecules or ions through ion channels[102, 103] and crown ethers[104]. Jarzynski has put forward an equality which connects the non-equilibrium steered MD with the equilibrium property, PMF for a particular system [105, 106]. It connects the equilibrium free energy with the work done through the non-equilibrium (or pseudo-equilibrium) processes.

$$\langle \exp^{-\beta W} \rangle = \exp^{-\beta.\Delta F} \tag{2.4}$$

where $\beta$ is $1/k_B T$, $\Delta$F is the change in free energy, W is the work done and $\langle \cdots \rangle$ denotes the average over the conformations. The other method is the weighted histogram analysis method (WHAM) [107] to extract the equilibrium data from the non-equilibrium steered MD trajectory. The Jarznyski's method involve the generation of the PMF profiles using multiple steered MD simulations whereas the WHAM method involves the generation of the PMF using a single steered MD simulation. We have used the latter method here. Two snapshots of the pulling is shown in the Figure 2.7.

### 2.2.7  Pull DSSP Profile

The terminal C-$\alpha$ carbon atoms were pulled away from each other to obtain an entirely unfolded peptide structure having a coil conformation. We have taken the A$\beta$ monomer pdb file and pulled across the end-to-end degree of freedom. Then, by storing the subsequent conformational states across this chosen degree of freedom we have extracted the PMF results.
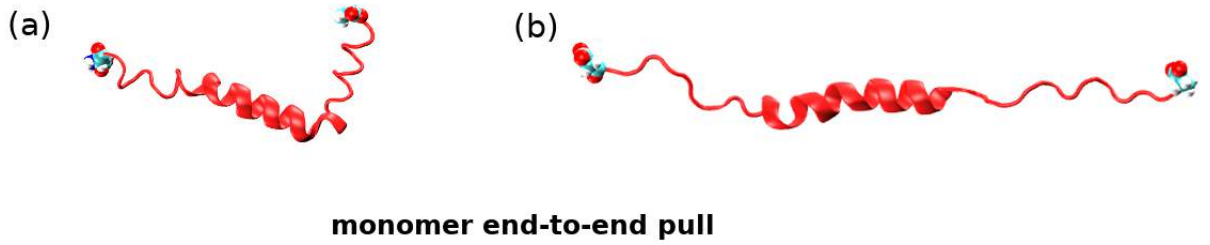
Figure 2.7: An $\alpha$-helix A$\beta_{42}$-monomer during the pulling simulation across the terminal residues. (a) is the initial starting configuration and (b) is the structure during the course of the pulling simulation.
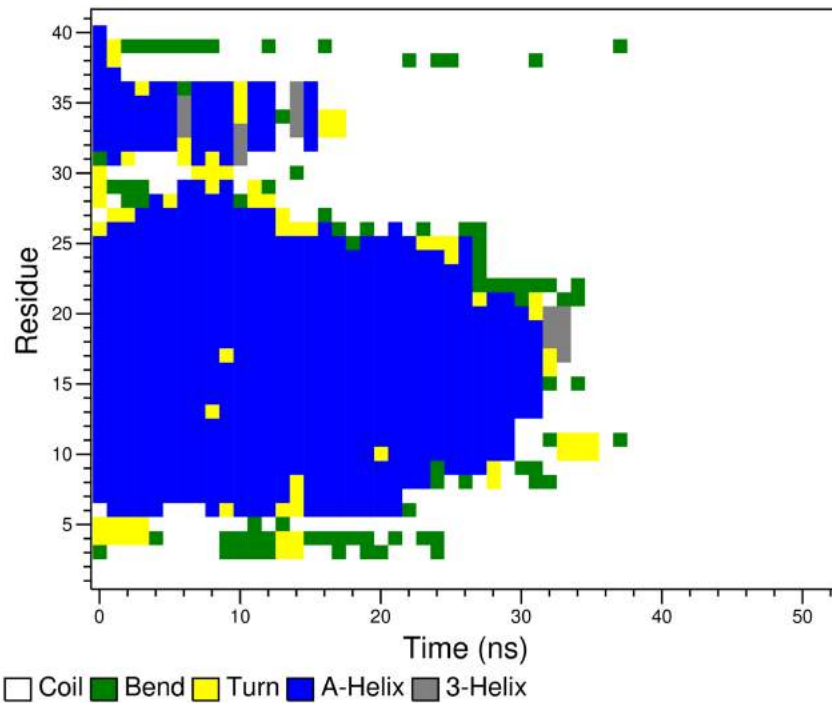


Figure 2.8: The pull DSSP profile of the A$\beta$ monomer $\alpha$-helix to coil

44
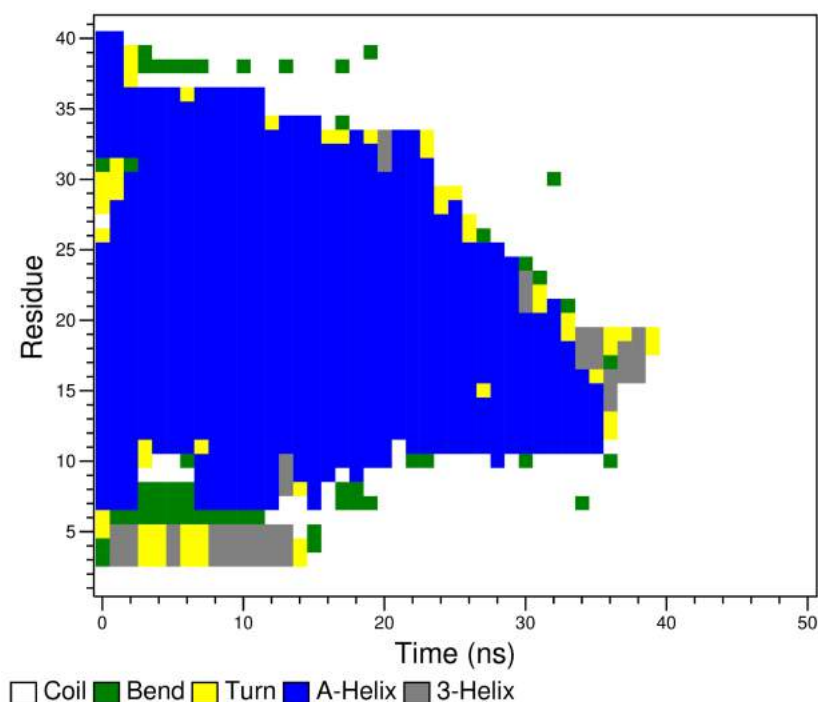
Figure 2.9: The pull DSSP profile for the A$\beta$ monomer $+$ Zn$^{2+}$

The pull DSSP profiles in Figures 2.8 and 2.9 show a few notable observations. The DSSP profile without the Zn$^{2+}$ ion is shown in Figure 2.8. We find that all the alpha helical zones are transformed to the turn conformation and subsequently to the coil conformation with some trace of 3-10 helix and bend coming up sporadically. Secondly, the C-terminal region (zone 4 according to our convention) is less rigid with respect to other parts of the peptide. The total uncoiling of the C-terminal $\alpha$-helix happens within the first 20 ns of pull simulation with a few traces of the turn, bend and 3- 10 helix conformation. For the other region, the uncoiling took longer time, with the maximum time taken for the uncoiling near the zone 1 (N-terminal) and the zone 2 (CHC) being nearly 38 ns. Thus, the C-terminal undergoes unwinding readily compared to the other regions.

In the A$\beta$ monomer the unwinding pattern appears to proceed along two regions simultaneously, characterized by the uncoiling of the $\alpha$ helices across the two different regions (one from D-7 to S-26 and the other from I-31 to V-40) that are separated by a turn por-

45
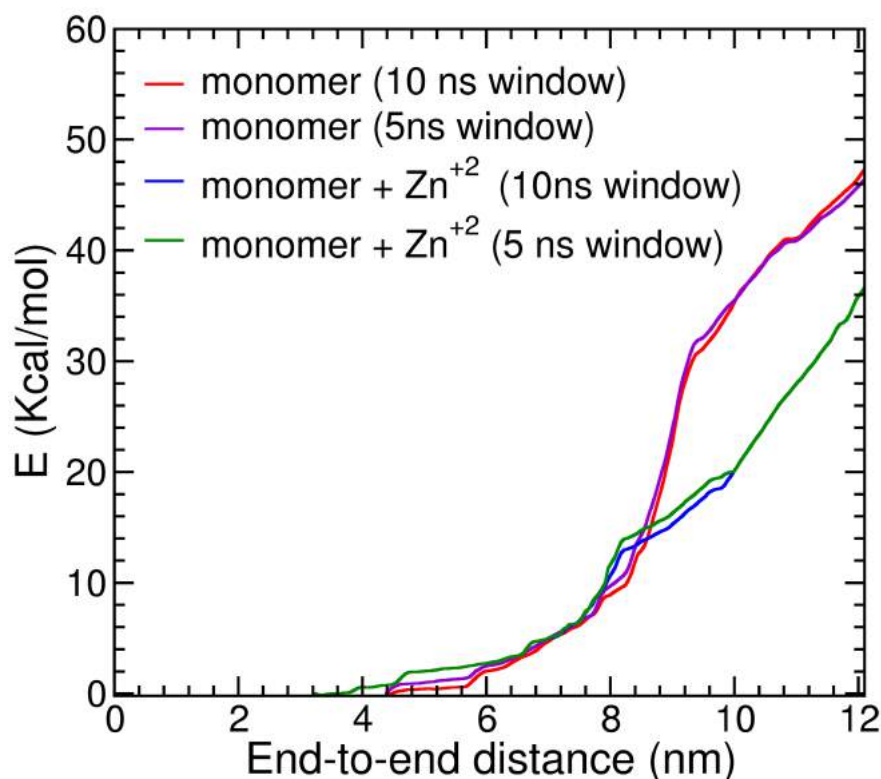
Figure 2.10: The PMF calculated from the stretching of the $\alpha$-helix to the coil structure.

tion. For the unwinding of the A$\beta$ monomer + Zn$^{2+}$, the DSSP profile in Figure 2.9 shows some significant changes. With the Zn$^{2+}$ ion, the unwinding is continuous, characterized by the smooth transformation of $\alpha$-helix to the coil structure. There is no distinction of the pull profile of the $\alpha$-helix at the two terminal regions. Thus, end-to-end pulling reveals the distinction in the nature of the $\alpha$-helices being found in the A$\beta$ monomer structure, both inclusive and exclusive of the Zn$^{2+}$ cation.

The PMF is then extracted by taking the conformations across the stretching co-ordinate. We have taken two sets of WHAM data, one by simulating 5 ns per window and another with 10 ns per window. The PMF for the A$\beta$ monomer with and without Zn$^{2+}$ is shown in Figure 2.10.

The evolution of the secondary structure across the $\alpha$-helix pull has been quantified

using the DSSP profile shown in Figure 2.8 and Figure 2.9. The free energy profiles are shown in the Figure 2.10. The corresponding free energy is calculated to be 46.64 kcal/mol in case of the $\alpha$-helix A$\beta$ monomer without Zn$^{2+}$ cation and 37.09 kcal/mol in case of the A$\beta$ monomer + Zn$^{2+}$. Literature studies have shown that the PMF calculations for the helix-coil transition of the alanine deca-peptide gives a value of nearly 22 kcal/mol in vacuum and nearly 7 kcal/mol in explicit solvent [100, 46]. In another study using the adaptive steered molecular dynamics (ASMD) the deca-alanine PMF for the helix to coil stretching has been calculated[108]. The pull distance in those cases are also defined with respect to the C-$\alpha$ atoms of the terminal atoms. The computational complexity in our case stems from the fact that the end-to-end distance of the A$\beta$ peptide is larger and hence the corresponding box dimensions.

## 2.2.8 Hydrogen Bonding profiles

The hydrogen bonding profiles for the helix to coil transition gives interesting information about the unfolding of the amyloid monomer [108]. The H-bonding profiles along with the PMF profiles help in detailed understanding of the H-bond rupture taking place during the course of the pull simulations. The i $-$ i+4 ($\alpha$-helix) contacts (where i refers to the residue index) are thoroughly disrupted in the course of the pulling simulation. The i $-$ i+4 contacts are ruptured along with the i $-$ i+3 (3$-$10 helix), i $-$ i+5 ($\pi$-helix) contacts, with the tearing of the residue contacts being different in the presence and absence of Zn$^{2+}$. The intra-helical contact distances (i $-$ i+j distance where j $\in$ 3 to 5) are traced to account for the H-bond breaking. The monomer + Zn$^{2+}$ system shows a more slow or delayed breaking of the H-bonds which is evident from both the intra-helical distance and the H-bond count profile shown in Figure 2.11. The A$\beta$ monomer + Zn$^{2+}$ system takes longer time to reach the coil conformation due to the increased network of H-bonding.

The i $-$ i+5 contacts ($\pi$-helix) are slightly more prominent inclusive of the Zn$^{2+}$ unlike
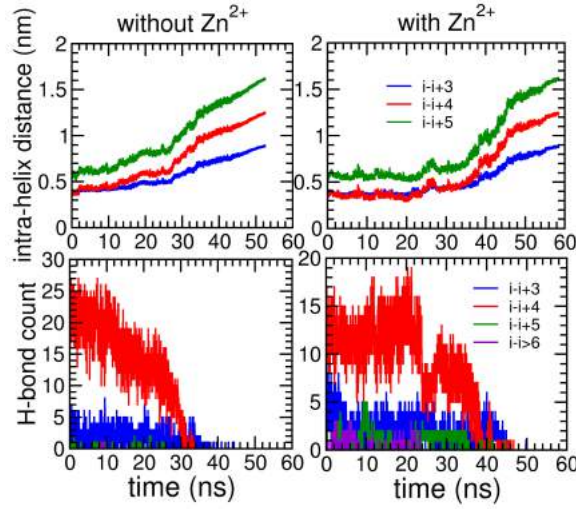
Figure 2.11: The intra-helix distance and H-bond count for the A$\beta$ monomer in absence and presence of Zn$^{2+}$ during the pull simulations.

for the A$\beta$ monomer. For the higher contacts i $-$ j (j $>$ i+6) the hydrogen bonding is more prominent in case of the A$\beta$ monomer $+$ Zn$^{2+}$ but the overall H-bond count for the i $-$ i+j (for j $=$ 3, 4, 5, 6) is less with the inclusion of Zn$^{2+}$. From the Figure 2.11, it is clear that the change in the H-bond count for i $-$ i+3 and i $-$ i+5 contacts is more in presence of the Zn$^{2+}$ ion which further proves the presence of more intra-peptide contacts. Hence, along with the DSSP profile, the H-bond profiles also show the differential rupturing preference of the amyloid peptide. Thus, it is evident from the helix to coil transition that the Zn$^{2+}$ cation influences the dynamics and structural properties.

The profiles of the intra-helical distances also show a clear difference upon the addition of the A$\beta$ monomer $+$ Zn$^{2+}$ (Figure 2.11). The i to i+j (j $=$ 3, 4, 5) distance which is defined as the intra-helix distance increases along the course of the pulling simulation as seen in the Figure 2.11. Increase in the intra-helical distance is observed to be faster in case of A$\beta$ monomer compared to the A$\beta$ monomer $+$ Zn$^{2+}$ ion. The breaking of the H-bonds (intra-peptide) for the A$\beta$ monomer $+$ Zn$^{2+}$ occurs at around 40 ns during the course of pulling. However, in case of A$\beta$ monomer, the intra-peptide H-bonds are broken earlier

48

which is seen as a steady increase of the intra-helical distance in the Figure 2.11. Hence, the influence of $Zn^{2+}$ ion on the intra-peptide H-bonding is evident. The rupture of the intra-peptide H-bonds disrupts the secondary structure, and these H-bonds are replaced by new peptide-water H-bonds formed in the solution. The rupture of the favorable intra-peptide H-bonds leads to the formation of a totally coiled state in going from $\alpha$-helix to coil.

The coiled conformation has no intra-peptide H-bonding to have the stability and it forms more peptide-water H-bonds for its stability in the solution. We define the change in the number of H-bonds as $\Delta N_{HB}^{peptide-water}$ which denotes the difference between the final and the initial number of H-bonds (peptide-water). For the helix-coil transition for $A\beta$ monomer the $\Delta N_{HB}^{peptide-water}$ is 88 and for the $A\beta$ monomer + $Zn^{2+}$ it is 74. The $\Delta N_{HB}^{peptide-water}$ being positive for both the cases show that the number of peptide-water H-bonds are increasing during the course of the helix-coil transition. The $A\beta$ monomer + $Zn^{2+}$ requires less number of peptide-water H-bonds in the solution for the stability. This is due to the fact that the $Zn^{2+}$ cation increases the number of intra-peptide contacts with the presence of more number of $i - i+j$ contacts as observed in Figure 2.11. The contact map in the case of the unbiased simulations also prove the case. The net lowering of the PMF values with the $Zn^{2+}$ ion can be attributed to the increased co-operativity of the H-bond breaking during the alpha helix unfolding. The earlier reports show that the alpha helices break the hydrogen bonds in a cooperative manner [109, 110, 111]. We assume that with the inclusion of the $Zn^{2+}$ ion, the co-operativity of the hydrogen bond breaking increases and hence the work done for the unfolding decreases. From the fact that there are more number of intra-peptide hydrogen bonds and more number of intra-peptide contacts in the contact map, in the presence of $Zn^{2+}$ ion, we can conclude that the $Zn^{2+}$ ion leads to the formation of more intra-peptide networks in the solvent. This increase in intra-peptide networks leads to the increased possibility of co-operativity in the hydrogen bond breaking, resulting in the decrease in net work done for unfolding in the presence of $Zn^{2+}$.
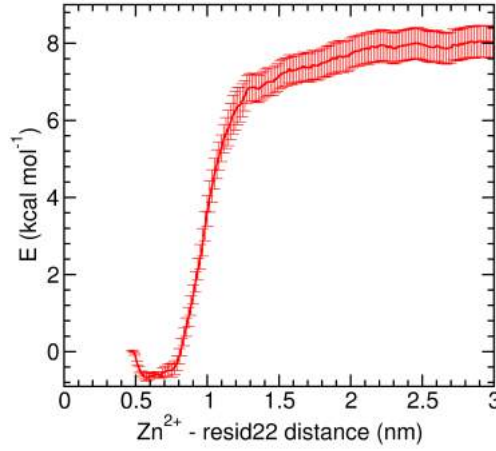
Figure 2.12: PMF for the pulling of the $Zn^{2+}$ cation away from the peptide

If we consider the overall difference of the number of intra-peptide H-bonds, $\Delta N_{HB}^{intra-peptide}$ (defined as number of intra−peptide H-bonds in final coil configuration minus the initial $\alpha$ helix ), it is $-33$ in case of A$\beta$ monomer and $-27$ for the A$\beta$ monomer + $Zn^{2+}$. The negative $\Delta N_{HB}$ shows that the number of the H-bonds are decreasing during the course of the transition. The number of intra-peptide H-bonds is higher in case of the A$\beta$ monomer compared to the A$\beta$ monomer + $Zn^{2+}$. The difference in the number of peptide-water H-bonds is higher in case of the A$\beta$ monomer (88) than that in the A$\beta$ monomer + $Zn^{2+}$ (74). Thus there exists an interplay of the intra-peptide and peptide-water H-bonding network in the solution for the stability during the course of the helix-coil transition. This observation has also been found consistent with the rat amylin peptide and also for the deca-alanine pull that is reported elsewhere [112, 113, 100].

The well depth for the binding of the $Zn^{2+}$ is calculated to be -9.11 $\pm$ 0.10 kcal/mol given in Figure 2.12. The PMF proves the significant binding of the $Zn^{2+}$ cation in the peptide.

## 2.3   Conclusion

All-atom molecular dynamics simulations of A$\beta$ monomer with and without the Zn$^{2+}$ ion were carried out to study the effect of Zn$^{2+}$ binding on an intrinsically disordered protein.

Unbiased simulations reported here shows the differential hydrophobicity/hydrophilicity with the presence of the Zn$^{2+}$ cation. The interplay of the discriminating affinity of water from zone 1 to zone 4 are evident from the corresponding RDFs. The structural differences can also be attributed to the Zn$^{2+}$ binding to the A$\beta$ monomer, where an increasing number of the long ranged contacts are established upon binding. The NH backbone dipoles show a longer mean lifetime in the presence of Zn$^{2+}$ and more variation at the N-terminal region. For the steered molecular dynamics simulations, the unfolding of the complex A$\beta$ monomer to the coil state gives us an idea of the relative flexibility and intra-peptide H-bonding in the presence of metal ion. The N-terminus of the A$\beta$ monomer is more rigid compared to the C-terminus. The difference in the mobility among the terminal residues is reduced with the inclusion of the Zn$^{2+}$ cation. The competitive intra-peptide and peptide-water H-bonding stabilizes the peptide in the protic solvent medium. Further studies using varying pull rates and pull force are underway in our group.

# Chapter 3

# The Effect of Lipid Composition on the Dynamics of Tau Fibrils

Tauopathies comprises of a set of central nervous system diseases such as Alzheimer's disease (AD), frontotemporal lobar degeneration, Pick's disease, and progressive supranuclear palsy, characterized by abnormal aggregation of the microtubule-associated protein tau (MAPT) [114]. Tau protein polymerizes tubulin to form microtubules (MT) and provides axonal support to MTs. Tau is an intrinsically disordered protein (IDP) that is soluble in normal conditions but can form insoluble aggregates. In a healthy brain tau proteins undergo phosphorylation which is 2-3 moles of phosphate per mole of tau protein. Hyper-phosphorylation in tau is when the phosphate mole ratio is almost 3 fold more than a normal brain tau [115]. Hyper-phosphorylation of tau makes it difficult for it to associate with MTs, and causes aggregation of tau and formation of paired helical filament (PHF) and neurofibrillary tangles (NFT) [116].

AD is characterized by gradual accumulation of amyloid plaques consisting of aggregates of A$\beta$ peptides and aggregates of tau. Research on AD was majorly focused on A$\beta$ peptides but due to failures of A$\beta$ targeting treatments in clinical trials, tau proteins are getting the attention of researchers [117]. A total of six tau protein isoforms are expressed in AD brain, ranging from 352 to 441 amino acids. The six isoforms of tau can be distinguished based on the presence or absence of inserts of 29 or 58 amino acids in the N-terminal half, and the inclusion or absence of the 31 amino acid microtubule-binding repeat in the C-terminal half. In general tau can be said to have four broad domains, the N-terminal domain, the proline rich domain, repeat domain region and the C-terminal domain [118].

Fetal brain has only three repeat domains (R3 tau) while the adult human brain has four repeat domains (R4 tau). The repeat domains R3 and R4 form the core structure for the paired helical filaments (PHF) and straight filaments (SF) [119]. PHFs and SFs both are composed of two protofilaments with C-shaped subunits [119]. Cryo-electron microscopy structures of tau filaments from the individuals with AD were determined by Fitzpatrick and coworkers which serves as a good starting point for MD simulations [120]. Studies have shown that tau interacts with plasma membrane through its amino projection domain [121]. Interaction of tau with plasma membrane is observed to promote tau aggregation in vitro, however, the exact mechanism is unknown [122]. Anionic lipid membranes facilitates the fibrillation of tau and A$\beta$ proteins [123, 124, 125]. Single molecule experiments have paved the way to explain the tau morphology across the series of lipids with varying lipid packing and net charge respectively [126, 127]. In the microtubule binding (MTB) region of tau, three segments (253-261, 315-323 and 346-355) have been observed to bind to lipids and take up a helical structure that facilitates protein aggregation [128, 129, 130]. Membrane lipids like phosphatidylcholine (PC), cholesterol, and sphingolipid have been observed to be associated with the tau proteins [131]. Membrane interactions with tau proteins show that the membranes play an important role in fibrillation and associated toxicity as reported in case of PHF6 hexapeptide [132].

Molecular dynamics simulations help in characterizing the intrinsically disordered proteins (IDPs) which do not possess any particular three dimensional structure [133]. IDPs possess seemingly dynamic conformation ensemble that are usually characterised by small angle neutron/X-ray scattering (SANS/SAXS), nuclear magnetic resonance (NMR), circular dichroism, fluorescence resonance energy transfer (FRET) etc [134, 135, 136, 137]. The data from the experimental techniques mentioned above are usually scarce for a complete structural and dynamical characterisation of the IDPs [138]. Recent development of the optimized force fields for the IDPs along with compatible water models [77, 139, 140]

have further improved their computational modeling. The interaction of lipid membrane with the amyloid fibrils are studied using both the coarse-grained and the all-atom models [141, 142]. Computer simulations have shown that in case of zwitterionic bilayers, fibril-membrane binding is dominated by coulombic interactions [143, 144]. Jang and coworkers have shown the possible fibril conformations along the pathways for the membrane insertion [141]. The increased cholesterol level also hints at the improved binding of the monomeric A$\beta$-42 to the bilayers [144]. In a different study using the replica exchange molecular dynamics (REMD), it was found that the cholesterol prevents the penetration of the A$\beta$-40 monomer into the lipid bilayer [145]. The hexapeptide $^{306}VQIVYK^{311}$ (PHF6) is used as a template in a number of MD simulations due to its similarity to the tau fibrils in vitro and also because its omission is found to prevent tau assembly [146, 147]. Few other MD simulations describing the conformational states of the tau helical filaments have been reported recently [148, 149, 150]. To the best of our knowledge, there are no reports of comprehensive computational study of the entire stretch of tau proteins with various lipid compositions. In this study, we elucidate the interaction of tau fibril (straight filament structure) at various lipid compositions using both all-atom and coarse grained MD simulations. The schematics of the straight filament structure of tau fibril along with the model bilayer are shown in Figure 3.1. In Alzheimer's disease the paired helical filaments predominate, whereas the straight filaments predominate in Pick's disease [151].

## 3.1 Methodology and simulation details

### 3.1.1 Coarse-grained simulations

The protein structure of the pdb id – 503T was coarse grained using the Martini representation. Martini version 2.0 and 2.2 have been used to model the lipids and proteins respectively [152, 153]. CHARMM-GUI was used to generate the initial configurations for the
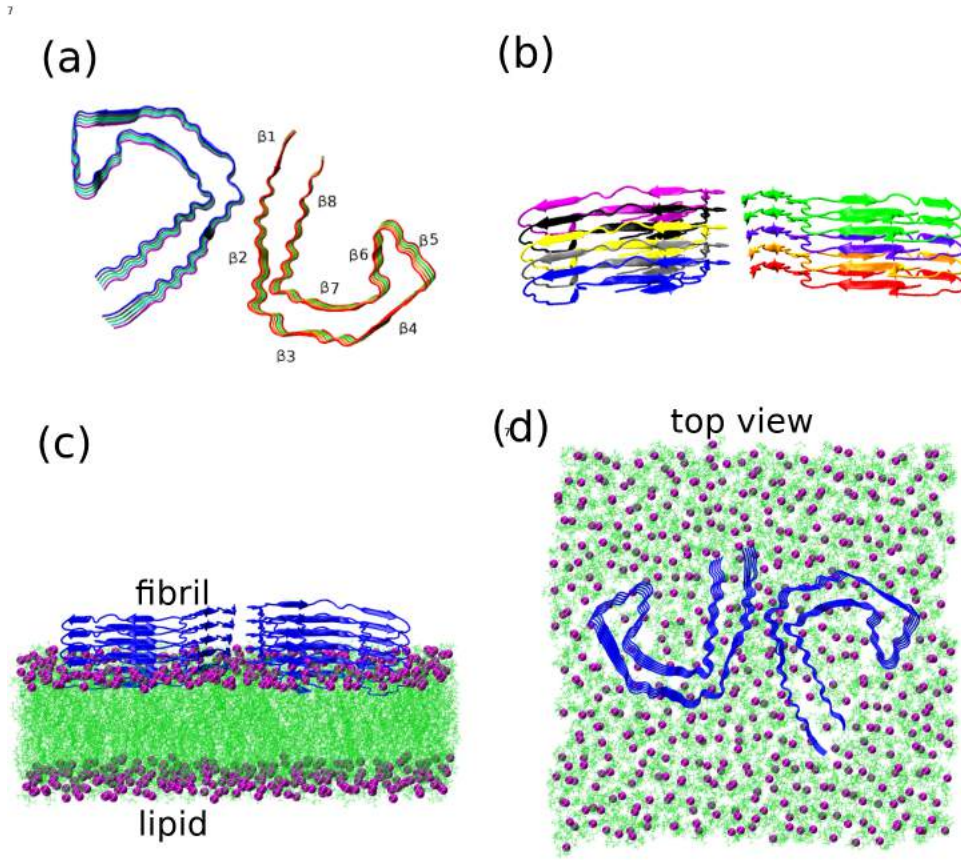
Figure 3.1: (a) The tau straight filament (SF) structure (PDB id- 503T) as seen from the top with each of the chains shown in different color. The strands of $\beta$-sheet regions are named sequentially from $\beta1$ to $\beta8$. (b) The individual chains of the tau-fibril are shown in different colors. (c) The fibril-lipid arrangement used in our simulations. The phosphorus atoms in the lipid head group are shown in purple, the lipid chains are shown in green and the fibril is shown in blue. (d) The fibril-lipid arrangement as viewed from the top.

fibril and lipids [154]. The simulations were performed using the parallelized GROMACS molecular dynamics code (version 5.1.4) [155]. The system was equilibrated after the initial energy minimization. The initial equilibration was done for the systems in six steps, restraining the proteins and lipids sequentially, according to the CHARMM-GUI protocol. Electrostatic and Lennard-Jones interactions were modeled up to 1.1 nm. The system was coupled to a thermostat at 310 K with a coupling constant of 1.0 ps using the v-rescale thermostat [156]. Pressure was maintained at 1 bar with a coupling constant of 5 ps us-

ing the semi-isotropic Berensden algorithm [157]. Production runs were performed using a time step of 20 fs for a duration of 10 $\mu$s. Electrostatic interactions were modeled using the reaction field method using dielectric constant of 15, following the recommended simulation parameters for coarse-grained Martini. The potential shift Verlet scheme was used for the Lennard-Jones cutoff at long distances. The initial velocities for the systems were chosen from a Maxwell distribution at 310 K. Final production runs were performed using the v-rescale thermostat and Parrinello-Rahman barostat with coupling constants of 1 ps and 12 ps respectively [81]. The details of the studied systems are presented in Table 3.1.

## 3.1.2 All-atom simulations

The initial structure of the fibril was taken from the pdb id − 503T for the all atom simulations with CHARMM-36m parameters [77]. The fibril was placed in the pre-equilibrated bilayer using the CHARMM-GUI module [154]. Water and chloride ions were added to solvate and neutralize the system. TIP3P was used to model the water molecules [158]. Additional 0.15(M) of KCl was added to maintain the physiological salt concentration. The lipid molecules and cholesterol were modeled using the CHARMM-36 parameters by Klauda et al [159, 160]. Energy minimization was performed to avoid steric clashes. The temperature was maintained at 310K using the Nosé-Hoover thermostat [161] with the coupling constant of 1.0 ps. The equilibration of the lipid bilayers were performed at subsequent steps using the CHARMM-GUI protocol by applying restraints on the proteins and lipids. The final production runs were performed in the NPT ensemble for 400 ns using a time step of 2 fs. The pressure was maintained at 1 bar using the semi-isotropic Parrinello-Rahman barostat [81]. The long range electrostatics were treated using the particle mesh Ewald (PME) [79]. Lennard-Jones interactions were calculated up to a cutoff distance of 1.2 nm with a force-switch function. The bonds involving hydrogen atoms were constrained using the LINCS algorithm [162]. All-atom simulations were carried out using the GROMACS

(version 5.1.4) MD code [155].

The analyses have been done using the in-house codes and GROMACS tools. The $\beta$-sheet content was analyzed using the DSSP utility in GROMACS. Clustering analysis was done using the Gromos algorithm implemented by Daura *et. al* [163] with the RMSD cutoff of 0.2 nm.

### 3.1.3   System Description

We have simulated 14 systems comprising of 1-palmitoyl-2-oleoyl-sn-glycero-3-phosphocholine (POPC), 1-palmitoyl-2-oleoyl-sn-glycero-3-phosphatidylethanolamine (POPE), 1-palmitoyl-2-oleoyl-sn-glycero-3-phosphatidylglycerol (POPG) along with cholesterol (CHOL) at seven different compositions. The composition of POPC/POPG/POPE + CHOL at the 7:3 ratio is taken according to the earlier study by the Sansom group [164]. Additionally, we have simulated the tau protein in a water box. Throughout our study, we have used symmetric composition of lipids in the upper and the lower leaflet of the bilayer. In case of the pure POPC system 255 POPC molecules are randomly placed both on the upper and lower leaflet with the tau peptide being placed on the membrane surface. In case of the POPC/POPE+CHOL systems, 179 POPC/POPE + 77 CHOL molecules are randomly placed on the upper leaflet and 178 POPC/POPE + 76 CHOL molecules are placed on the lower leaflet and are then packed by placing the tau-peptide over the membrane surface. In POPG+CHOL, the upper leaflet comprises of 193 POPG and 83 CHOL, and the lower leaflet comprises of 192 POPG and 82 CHOL. To account for the smaller surface area of the POPG lipids over the POPC lipids according to the default setting of CHARMM-GUI membrane builder, 550 lipids are taken for the POPG+CHOL systems to cover the entire area spanned by the tau fibril. Finally, in the POPC+POPE systems the upper and the lower leaflet comprises of 128 POPC + 127 POPE molecules respectively along with the tau peptides. The simulation details are given in Table 3.1.

Table 3.1: Details of the fibril and lipid systems used in the study.

| System description | Number of lipids | Number of waters | Production run (ns) | Number of atoms |
|---|---|---|---|---|
| All-atom (protein and lipids) | | | | |
| POPC | 510 | 46400 | 400 | 219248 |
| POPE | 510 | 40692 | 400 | 197500 |
| POPG | 510 | 42358 | 400 | 203938 |
| POPC + CHOL (7:3) | 510 | 41478 | 400 | 195424 |
| POPE + CHOL (7:3) | 510 | 31334 | 400 | 161569 |
| POPG + CHOL (7:3) | 550 | 42463 | 400 | 200461 |
| POPC + POPE (1:1) | 510 | 44309 | 400 | 210666 |
| protein (no-lipids) | — | 106819 | 40 | 332515 |
| All-atom (pure lipids) | | | | |
| System description | Number of lipids | Number of waters | Production run (ns) | Number of atoms |
| POPC | 200 | 12300 | 40 | 63764 |
| POPE | 200 | 10856 | 40 | 56812 |
| POPG | 200 | 11116 | 40 | 59004 |
| POPC + CHOL (7:3) | 200 | 10819 | 40 | 55713 |
| POPE + CHOL (7:3) | 200 | 9652 | 40 | 50946 |
| POPG + CHOL (7:3) | 200 | 10040 | 40 | 52532 |
| POPC + POPE (1:1) | 200 | 11488 | 40 | 60422 |
| Coarse-grained (protein and lipids) | | | | |
| System description | Number of lipids | Number of water beads | Production run ($\mu$s) | Number of beads |
| POPC | 510 | 12078 | 10 | 20162 |
| POPE | 510 | 9822 | 10 | 17846 |
| POPG | 510 | 10410 | 10 | 18864 |
| POPC + CHOL (7:3) | 510 | 10309 | 10 | 17739 |
| POPE + CHOL (7:3) | 510 | 9697 | 10 | 17468 |
| POPG + CHOL (7:3) | 550 | 10132 | 10 | 18273 |
| POPC + POPE (1:1) | 510 | 11154 | 10 | 19214 |

58

## 3.2   Results and discussion

### 3.2.1   Area per lipid and Bilayer Thickness

We have modeled different systems to study the effect of the net charge of the lipid molecules and the effect of cholesterol on the tau fibril. Neutral 1-palmitoyl-2-oleoyl-sn-glycero-3-phosphocholine (POPC)/ 1-palmitoyl-2-oleoyl-sn-glycero-3-phosphatidylethanolamine (POPE) and negatively charged 1-palmitoyl-2-oleoyl-sn-glycero-3-phosphatidylglycerol (POPG) are used to form the bilayer. In addition to that, a mixed composition of POPC and POPE is also used to build the bilayer in accordance to the earlier MD studies [165, 166]. In this way seven compositions of the bilayer are included in our study. Further details of the simulation setup is included in System Description. For the subsequent analyses, the abbreviations PC, PC+CL, PE, PE+CL, PC+PE, PG, PG+CL are used to refer to POPC, POPC+CHOL, POPE, POPE+CHOL, POPC+POPE, POPG and POPG+CHOL lipid composition respectively. All-atom simulations are done upto 400 ns for the large system size (nearly 200 thousand atoms). Coarse-grained simulations are done for 10 $\mu$s accounting for a better sampling. Cholesterol is known to induce changes in the properties of the bilayer. Cholesterol is necessary for the formation of lipid rafts and microdomains, and it adds stability to membrane proteins by increasing the membrane thickness and membrane lipid rigidity [167]. The adsorption and the interaction of the tau proteins with the bilayers are the initial steps in the structural changes initiated over the cell membrane. Anionic lipids are proven to induce the tau aggregation [123]. PC consists of zwitterionic headgroups whereas the PE consists of ethanolamine headgroup. PG is an anionic lipid with a net charge of (-1). Negatively charged PG lipids are found to influence the structure and conformation of other membrane proteins [168]. To analyse the effect of tau peptide on the lipid membrane, we have computed the area per lipids (APL) and the membrane thickness at all the lipid compositions with and without the presence of the tau protein. The mean bilayer thickness and

Table 3.2: Variation of the bilayer properties with and without the tau protein.

| Bilayer | Area per Lipid ($nm^2$) | Bilayer thickness (nm) |
|---|---|---|
| POPC | 0.64 | 3.92 |
| POPC + tau | 0.60 | 3.88 |
| POPE | 0.56 | 4.28 |
| POPE + tau | 0.52 | 4.15 |
| POPG | 0.69 | 3.70 |
| POPG + tau | 0.63 | 3.64 |
| POPC + CHOL | 0.48 | 4.48 |
| POPC + CHOL + tau | 0.43 | 4.40 |
| POPE + CHOL | 0.46 | 4.56 |
| POPE + CHOL +tau | 0.40 | 4.53 |
| POPC + POPE | 0.60 | 4.11 |
| POPC + POPE + tau | 0.54 | 4.09 |
| POPG + CHOL | 0.50 | 4.29 |
| POPG + CHOL + tau | 0.45 | 4.23 |

the area per lipids (APL) are given in Table 3.2. The area per lipid is calculated using the x and y dimensions of the box length and dividing the area by the total number of lipids in a leaflet. The bilayer thickness is computed using the average intra-phosphate distance in the bilayer. Figure 3.2 shows the change in bilayer properties depicted in a box and whisker plot. The presence of tau protein decreases both the APL and the bilayer thickness across all the lipid compositions. The significant decrease in the APL ($0.06$ $nm^2$) is observed in the PG, PC+PE and PE+CL systems and the largest change (0.13 nm) in the membrane thickness is seen in the PE systems. The bilayer thickness for our model systems increases upon the tau fibril binding whereas the area per lipids decreases across the simulation time with the binding of tau fibril. The value for the area per lipids and the bilayer thickness given in Table 3.2 is the average value across the simulation timescale.

To describe the local deformations of the lipid bilayers with the tau-protein, we have calculated the variation of the bilayer thickness in the system. The variation of bilayer thickness describing the local perturbations of the bilayer around the tau peptide in systems with PG and PG+CL in the presence of tau peptide is shown in Figure 3.3.
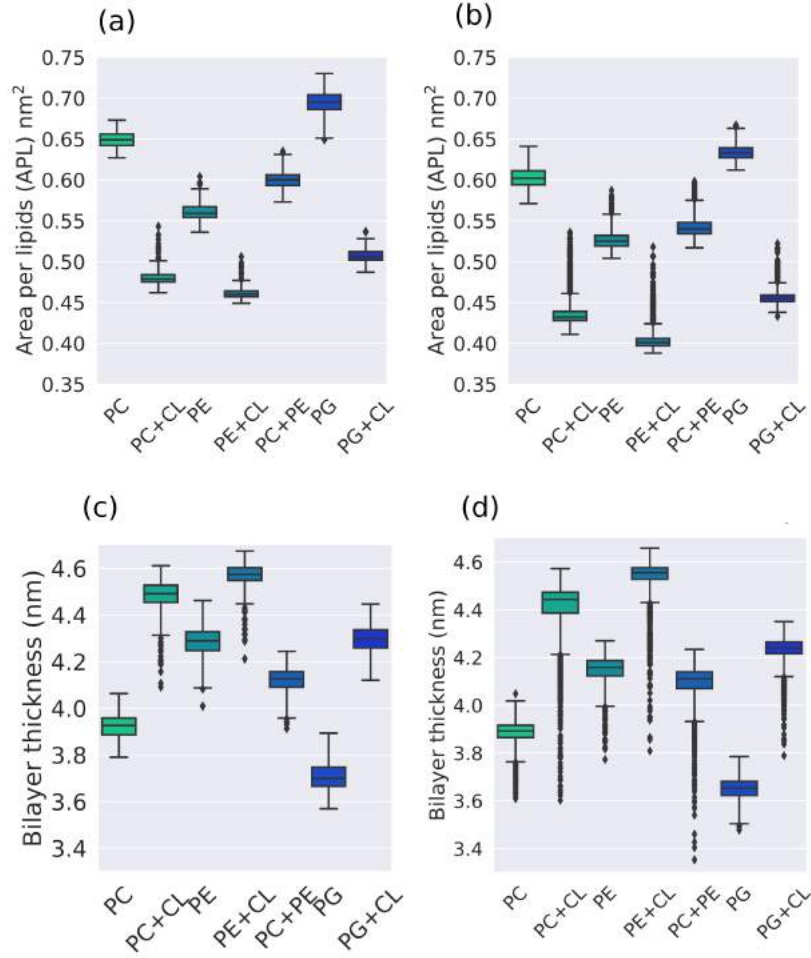
Figure 3.2: Box and whisker plots of the area per lipid and the bilayer thickness in case of the pure bilayers and bilayers with tau fibril. (a) and (b) Area per lipids (APL) for the pure lipids and the lipids with tau fibril respectively. (c) and(d) Bilayer thickness for the pure lipids and the lipids with tau fibril respectively.

### 3.2.2 Deuterium Order Parameter ($S_{CD}$)

The order parameter ($S_{CD}$) is important to quantify the structural deformation and flexibility of lipids in bilayers. Experimentally, the order parameters are derived from the NMR. The carbon atoms near the headgroup have higher order parameter, which decreases down the length of carbon chain since the movement of head groups are restricted and the tail regions
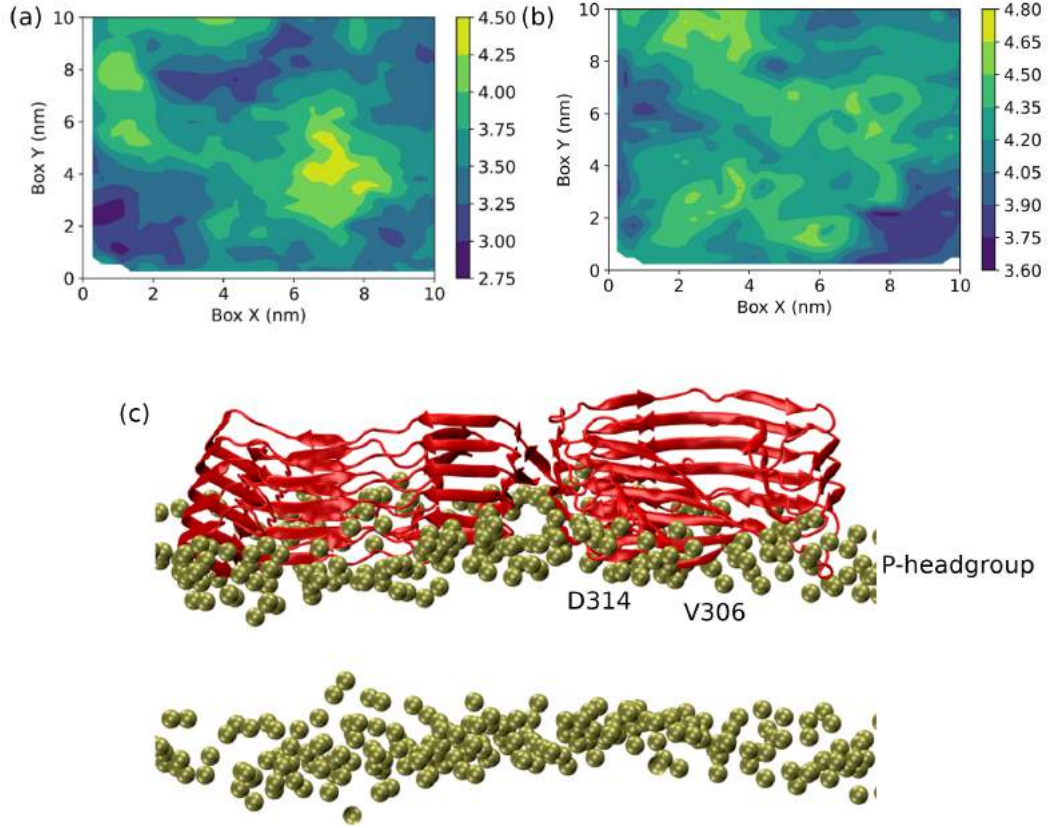
Figure 3.3: (a) and (b) are two dimensional thickness plots in the PG and PG+CL respectively, in the presence of tau-proteins. The thickness is shown in [nm] units in the color bar. (c) The representative snapshot of the tau-protein perforating the lipid bilayer in case of the POPG system. Only the head groups are shown for clarity.

are relatively free to move in the bilayer. $S_{CD}$ is determined using the equation

$$|S_{CD}| = \left( \frac{3}{2} \cos^2 \theta - \frac{1}{2} \right) \tag{3.1}$$

where $\theta$ is the angle between the C-H bonds in the lipid tail and the bilayer normal.

The presence of tau fibril leads to the decrease in the lipid order parameters as seen in case of PE systems shown in Figure 3.4. The order parameters of the pure PE lipids match with the earlier simulation and experimental results [169, 170, 171]. The decrease in the order parameter is observed in both sn-1 and sn-2 chains. The decreasing $S_{CD}$ order parameter correlates with the membrane thickness of the lipids in presence of tau protein
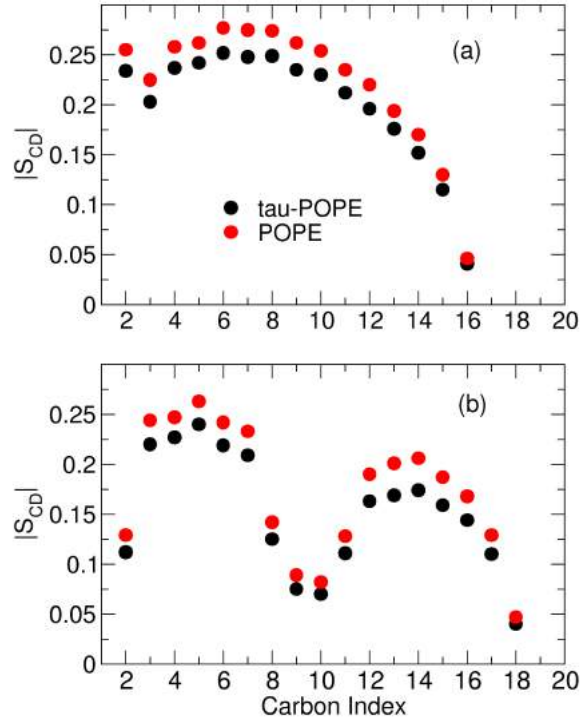
Figure 3.4: Deuterium order parameter ($S_{CD}$) for the (a) sn-1 chains and (b) sn-2 chains in case of pure POPE and POPE with tau protein.

and the pure lipids. The decreasing order parameter translates to the decreases in the bilayer thickness for lipid bilayers in presence of tau proteins. Higher order parameter indicate linear lipid chains which in turn leads to increase in bilayer thickness of the pure lipids.

The addition of cholesterol in the bilayer leads to an increase in the membrane order parameters in case of both the pure lipids and lipids with tau, in accordance with the trend observed in the bilayer thickness.

### 3.2.3 Tau Fibril Stability

The structural differences of the tau fibril in various lipid membranes are studied using the root mean square deviations (RMSDs) and the root mean square fluctuations (RMSFs) of the tau protein. The RMSD and RMSF are calculated from the 400 ns of all-atom trajectory

of the peptide – bilayer systems. The RMSD and RMSF plots are given in Figure 3.5.
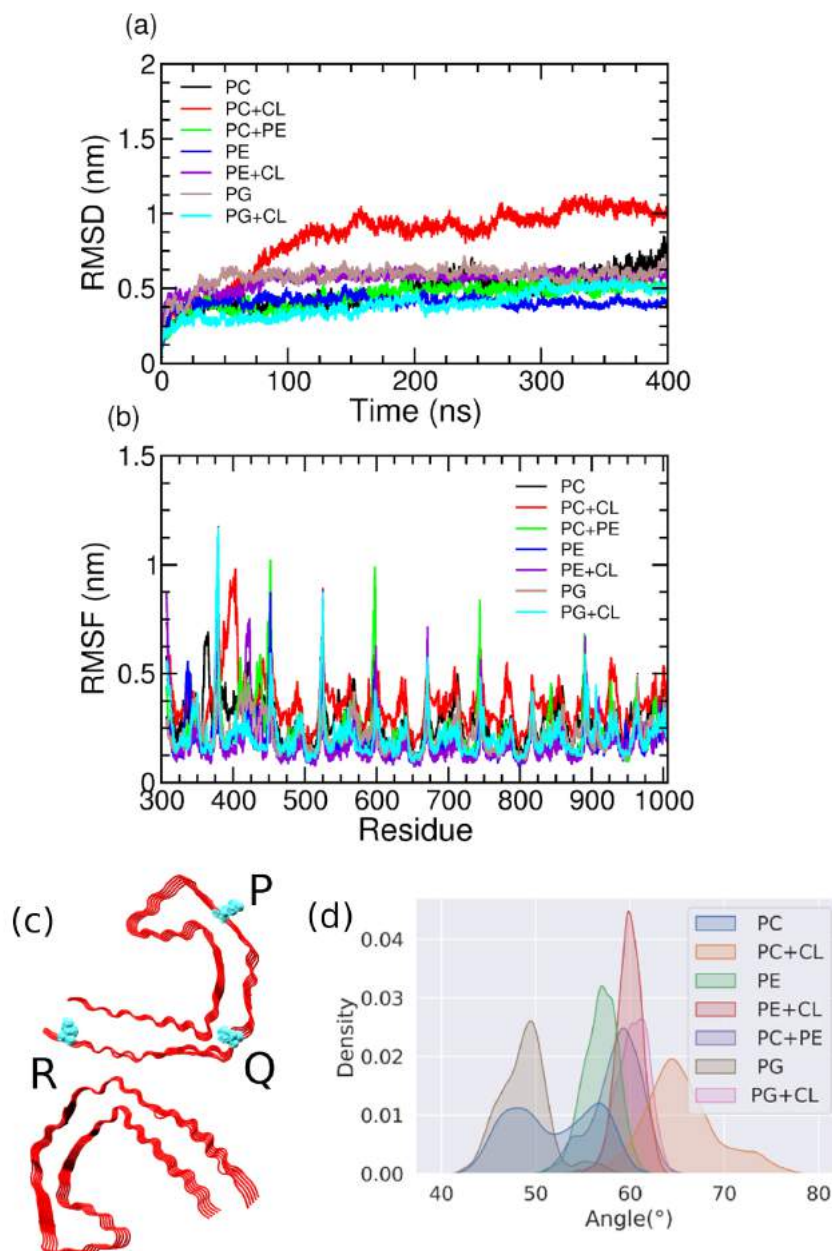


Figure 3.5: (a) RMSD of the C-$\alpha$ atoms of the tau peptides in the systems used in our study. (b) RMSF of the residues in the tau-peptide across all the systems (c) Pictorial representation of the angle of coverage (PQR) used in the discussion. Three reference C-$\alpha$ residues are shown as blue VDW spheres. (d) The distribution of the corresponding angle in various bilayer systems.

RMSDs show that the MD simulations are converged after 30 ns. The tau proteins in the PE+CL and PG+CL systems are the most stable as seen from the RMSF plots. Tau-peptides in the PC+CL show the most fluctuations, followed by the those in pure PC. Hence it is evident that the charge of the lipids and the incorporation of the cholesterol regulate the structural fluctuations of the tau peptide.

To further analyze the dynamics of the tau proteins, we calculated the angle of coverage which is defined by the position of C-$\alpha$ residues as shown in the Figure 3.5(c). The angle of coverage defines the characteristic "C"-letter of the tau peptide from the cryo-EM structure. This angle is an important criterion to study the dynamics of the tau protofilament core and describes the area spanned by the tau-protein over the membrane plane. The cryo-EM angle for the reference structure is found to be 57° and the corresponding angle in the water box simulation is found to be 54°. The distribution of this angle in all the studied systems are shown in Figure 3.5(d). We found that the angle of coverage depends on the lipid composition, and the incorporation of cholesterol increases the angle of coverage.

### 3.2.4 $\beta$-sheet content

Composition of the lipid membranes have an effect on the secondary structure content of the intrinsically disordered $\beta$-fibrils. The secondary structures of the intrinsically disordered proteins in turn effect their percolation within the lipid membranes. We have analysed the effect of the composition of the lipid membrane on the tau-structure. Previous MD simulations have given important insights into the secondary structures of amyloid fibrils interacting with lipid bilayer [172]. The distribution of the number of residues present as $\beta$-sheets are shown as violin plots in Figure 3.6(a). The negatively charged PG lipids are found to increase the $\beta$-sheet content. Cholesterol decreases the $\beta$-sheet content of the tau fibril in case of PC and PE but increases in the case of PG lipids. The mixed PC – PE lipids also increase the $\beta$-sheet content with respect to the pure PE and PC lipids. The number

of $\beta$-sheet residues in case of the bulk water, with a mean value of $430 \pm 12$, is higher than in presence of any lipids. The per-residue propensity of the secondary structures in the interacting chains of these systems are shown in Figure 3.6(b)-(c). The C-terminal residues lose significant $\beta$-sheet in the PC+CL. The decrease in the number of $\beta$-sheet residues is more in case of the PC+CL compared to the pure PC system. The $\beta$-sheet residues near the terminal chains of the fibril are transformed to random coil and bend structures. The PG+CL lipids only restore a significant amount $\beta$-sheet content of the tau fibril across the simulation timescale, whereas in case of all the other systems the $\beta$-sheet content decreases.

It is evident that the presence of the charged membranes and the incorporation of the cholesterol modulate the $\beta$-sheet content in the tau fibrils.

### 3.2.5 Hydrogen Bonding

We have classified the hydrogen bonding according to the geometric criteria [90]. In a strong hydrogen bond, the hydrogen atom and the acceptor are separated by a distance less than 2.2 Å, and the angle made by the donor, hydrogen atom, and the acceptor is within the range $130° - 180°$. The corresponding distance and angular range are $2.0 - 3.0$ Å and $90° - 180°$, respectively, for a weak hydrogen bond. We found no strong hydrogen bonding in any of the trajectories. Inter- and intra molecular hydrogens bonds calculated from the simulations are useful in determining the structural properties of the bilayer at molecular level. The hydrogen bonding information of different systems (both intra- and inter-fibril) are given in Figure 3.7.

The probability of intra-fibril hydrogen bonding is found to correlate with the charge of the lipid and the presence of cholesterol as shown in the correlation matrix in Figure 3.7(c). Correlation matrix is an easy way to summarize the correlation between all the variables in a dataset. It is calculated through the Pearson correlation coefficient with -1 meaning a negative correlation, +1 meaning a positive correlation and 0 meaning no correlation. Each
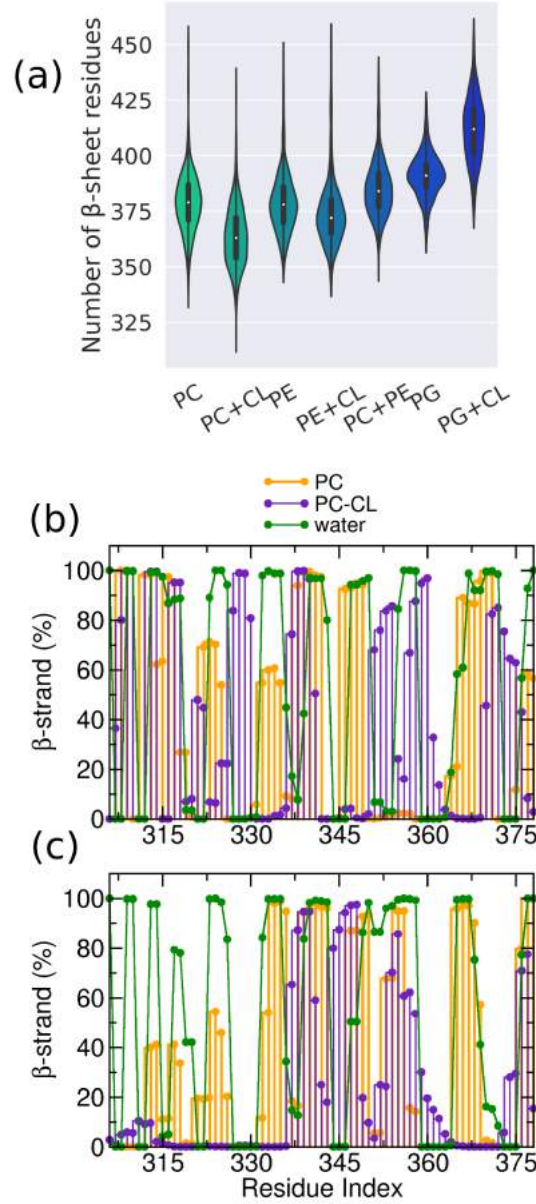
Figure 3.6: (a) Violin plots of the distribution of the number of residues of tau fibril present as $\beta$-sheet across all the lipid compositions. (b)-(c) are the per residue propensity of $\beta$-strand in the chain A and chain B of tau fibril respectively.

element of the matrix is the correlation coefficient ($c_{ij}$) of the intra-fibril hydrogen bonding across the systems. The correlation matrix is defined as follows

$$c_{ij} = \sum_n \frac{(z_{ni} - \bar{z}_i)(z_{nj} - \bar{z}_j)}{\sigma_i \sigma_j} \tag{3.2}$$

67
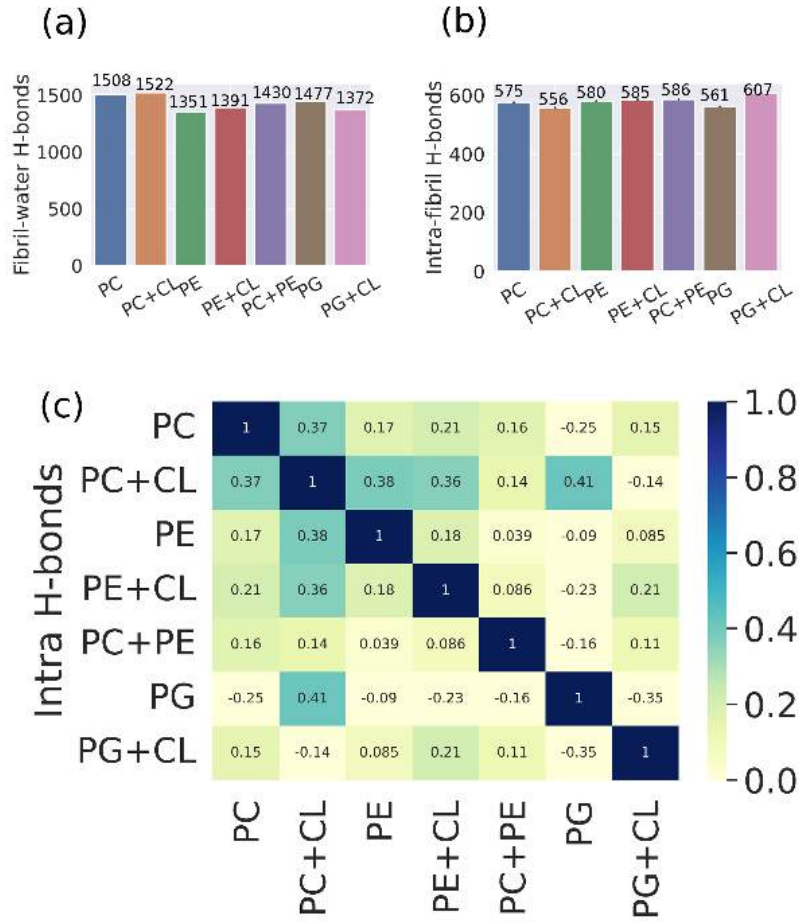
Figure 3.7: (a) The fibril-water hydrogen bonding and (b) intra-fibril hydrogen bonding across all the systems. (c) The probability to form intra-fibril hydrogen bonding shown through a correlation matrix for all the lipids. The scale for the magnitude of the correlation is shown in a color bar.

where $c_{ij}$ denotes the $ij$-th element of the correlation matrix, $(i, j)$ are the two different sets of data points across which the correlation is calculated, $z_{ni}$ is the number of intra-fibril hydrogen bonds in the n-th frame of the system $i$, $\bar{z}_i$ and $\bar{z}_j$ are the mean number of intra-fibril hydrogen bonds over all the frames in the system and $\sigma_i$, $\sigma_j$ are the standard deviations of intra-fibril hydrogen bonds in the system $i$, $j$ respectively.

The negatively charged PG and PG+CL are inversely correlated whereas the systems with PC/PE lipids are directly correlated with PC+CL/PE+CL. The trend is similar to the

variation of the number of residues of tau present as $\beta$-sheets in the bilayer with cholesterol, as the intra-fibril hydrogen bonds keep the $\beta$-sheet structure of the tau protein. In presence of cholesterol, $\beta$-sheets are stabilized in negatively charged PG+CL system due to the increase in the number of intra-fibril hydrogen bonds.

For the intermolecular hydrogen bonding between the tau and water, no clear trend is observed. The cholesterol increases the tau-water hydrogen bonding in the PE, decreases the hydrogen bonding in PG and shows negligible difference in the PC.

### 3.2.6 Number of Contacts

We calculated the number of lipid contacts with fibril to characterize the fibril–lipid interaction. The timeline for the number of contacts are given in Figure 4.8(a). The coarse grained (CG) trajectories are used to model the long timescales of the binding of proteins to the lipids. The CG cutoff for the contacts are taken to be 0.7 nm according to the $\alpha$-synuclein binding work by Sansom group [164]. The highest number of contacts are observed in the system with PG lipids, and the least number of contacts in system with PC lipids. Due to the higher number of lipids in the PG+CL system, we have also checked the number of fibril-lipid contacts per lipid molecule that still follows the same trend as the total number of contacts. Cholesterol increases the number of contacts in both zwitterionic and anionic lipids. The number of contacts is reduced in mixed PC+PE and is comparable to the PC lipids. Thus the negatively charged lipids increase the binding propensity of the tau-peptides to the membrane. The principal structures obtained by the clustering algorithm (shown in Figure 4.8) also reveal that the tau-fibril show differential mode of interaction with the lipids. Clustering algorithm reveals the major binding modes of the tau fibril with our model lipid bilayers. We find that the binding of the tau fibrils on the lipid bilayers coincide with the loss of $\beta$-sheet zones across the tau filament along with disrupting the lipid bilayers. For the most probable structure in the PC lipids, the tau fibril disrupts the bilayer causing
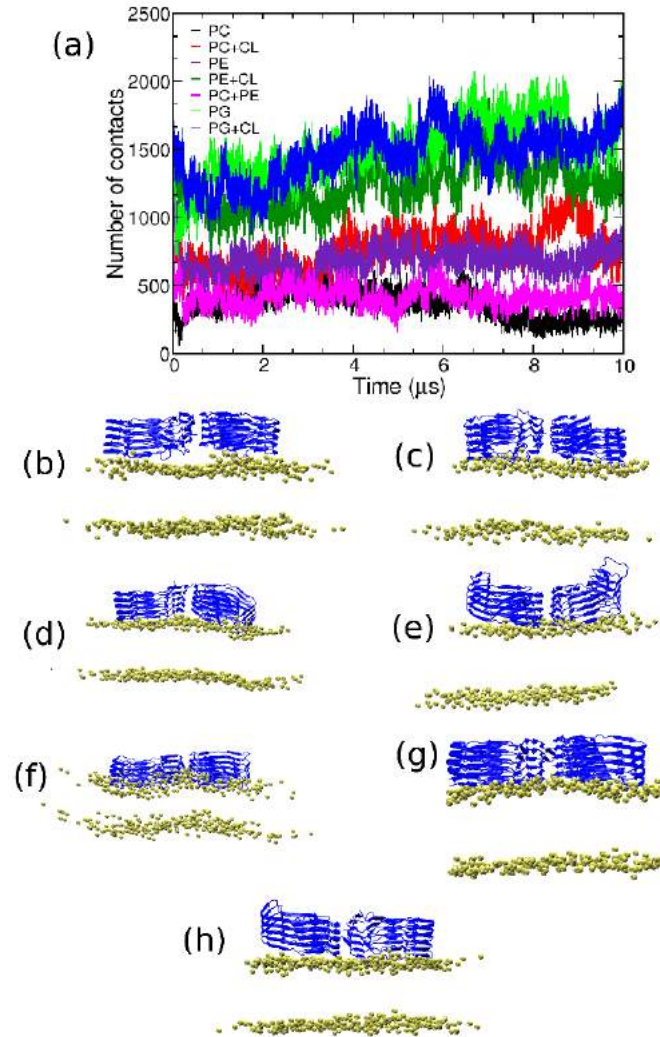
Figure 3.8: (a) Number of fibril – lipid contacts across all the trajectories. (b)-(h) are the most probable structures obtained through the clustering algorithm. The peptide is shown in new cartoon representation in color blue and the phosphorus atoms are shown as VDW spheres.

the $\beta$-sheet regions of the $\beta7$ region of the tau fibril (according to Figure 3.1(a)) changing to random coil configurations. With the PC+CL lipids the $\beta$-sheet regions are disrupted for larger portions across the $\beta1$-$\beta4$ and $\beta7$ zones of the fibril. For PE lipids the $\beta4$ shows the most prominent loss of $\beta$-sheet. In case of PE+CL the $\beta$-sheet regions are lost across the $\beta5$-$\beta7$ regions. In case of PG lipids the $\beta3$ and $\beta8$ zones lost the $\beta$-sheet content. With the cholesterol in case of PG+CL lipids the tau fibril shows most conserved $\beta$-sheet zones across the residues as explained earlier from the section describing the secondary structure. For PC+PE lipids the $\beta3$ zone shows most significant loss of the $\beta$-sheet structure. Thus we describe the local changes induced by the bilayer binding on the tau fibril structure. The single molecule experiments using the Forster resonance energy transfer (FRET) and fluorescence correlation spectroscopy (FCS) have shown that the tau proteins upon binding to negatively charged DMPS bilayers lead to the opening of the N and C-terminal domains [127]. Our results show that the negatively charged PG lipids show most conserved $\beta$-sheet regions, with the inclusion of CL further mediating the conservation. The PG and PG+CL lipids thus form most suitable binding with the tau fibrils explaining the stability of the tau fibrils in the negatively charged membranes. On the contrary the secondary structure of the tau fibrils are lost in the zwitterionic membranes hampering the effective intra-fibril hydrogen bonding. Moreover the tau binding on the lipid bilayers impact the secondary structure content of the terminal residues of the tau protein which has been earlier shown to mediate the liquid liquid phase separation (LLPS) of tau [173].

## 3.3 Conclusion

The knowledge of the interaction of the tau proteins with the lipid membranes is pivotal to the study of the effect of tau peptides on the cell membrane. The detailed molecular level interaction of the tau proteins with lipids and their effect in the tauopathy is still un-

available. This is due to the complex lipid compositions and the difficulty in characterizing the tau-peptides experimentally. The MD simulations of the tau-peptides in seven different lipid systems, comprising of zwitterionic and charged lipids have been carried out. The tau proteins are found to preferentially bind to anionic lipids than to the neutral lipids in agreement with the experimental reports [122, 125]. The binding of the tau fibrils with the model bilayers lead to the loss of $\beta$-sheet structures across the fibril residues. The tau binding also induce membrane perturbations as explained from area per lipids, bilayer thickness and order parameter calculations with respect to the pure lipid. Lipid packing and lipid phase seperation has earlier been found to induce the changes in the tau construct K18 using the atomic force microscopy (AFM) [126]. The addition of cholesterol leads to an increase in the thickness of the bilayer and the lipid tail order, but decreases the area per lipid. Cholesterol infused lipids in our model bilayers induce definite changes in the tau-conformational states. The changes induced by the cholesterol also differs between the anionic PG and the zwitterionic PC/PE membranes. Hence, our study illustrate that the composition of lipids in the cell-membrane influences the interaction and binding of tau-peptides.

# Chapter 4

# Interaction of the Tau Fibrils with the Neuronal Membrane

The tau protein plays an important role in microtubule stabilization and aggregation [174]. In diseased neurons, tau loses the capacity for microtubule binding and forms toxic aggregates [175]. These toxic aggregates are the causative agents for a series of neurodegenerative diseases collectively known as tauopathies [114]. Tauopathy comprises a set of neurodegenerative diseases like Alzheimer's Disease, Pick's disease, frontotemporal lobar degeneration, etc. Hyperphosphorylated tau has a positive effect on the progression of Alzheimer's disease (AD). Tau is an intrinsically disordered protein (IDP) that shows a diverse conformational ensemble [176]. Tau and the other disease-forming aggregates have been shown to evolve through the liquid – solid and liquid – liquid phase transition of the proteins [130]. The conformational dynamics of the tau fibrils has a significant role in the pathogenesis of tauopathy as shown from the earlier molecular dynamics studies [146, 150, 177]. Owing to the failure of the amyloid-beta as the drug-binding target for Alzheimer's disease (AD), the current focus is mostly on the tau fibrils and their underlying conformational changes in regulating the concurrent tauopathies [117, 178]. The interaction of the lipid bilayers with the tau is pivotal in understanding the mechanism of toxicity of the tau fibrils [179]. Our earlier MD study was focused on the effect of the net charge of the lipids and the effect of cholesterol in determining the tau conformational changes [34]. It has been widely accepted that the negatively charged lipids influence the tau aggregation [125, 122].

The emergence of single molecular techniques has further enhanced our knowledge

related to tau aggregation and conformational states of IDPs [180]. Single-molecule Fluorescence resonance energy transfer (smFRET) and fluorescence correlation spectroscopy (FCS) have shown that the tau proteins bind to the DMPS membrane in a concentration dependent manner. At low DMPS concentrations the tau proteins form oligomers. At high DMPS concentration the tau proteins inhibit amyloid formation due to the stable binding with DMPS [127]. Atomic Force Microscopy (AFM) study has explained the effect of $PIP_2$ lipids on the Tau microtubule-binding construct K18 [181]. Intrinsically disordered proteins (IDPs) have also been characterized using molecular dynamics simulations with the emergence of the optimized force fields and compatible water models [176, 138, 182, 183]. The dynamical changes in the IDPs are experimentally derived using the small angle neutron/X-ray scattering (SANS/SAXS), nuclear magnetic resonance (NMR), circular dichroism (CD), fluorescence resonance energy transfer (FRET), etc which are usually insufficient to obtain complete dynamical information of the IDPs [135, 136, 137, 134]. Thus, molecular dynamics simulations have been widely used to characterize the IDPs responsible for AD pathogenesis, especially the amyloid-beta peptide and amyloid fibrils [184, 165, 164, 142, 141]. Strodel et al. have studied the interactions of the amyloid-beta dimer with the axonal membrane [33]. In the pursuit of gaining atomic level insights into the interaction between the tau fibril and neuronal membrane, we have modeled the paired helical filaments (PHF) and straight filaments (SF) in the presence of model neuronal membrane for a cumulative sampling of 4 microseconds. To the best of our knowledge, this is the first comprehensive computational work on the tau fibrils in presence of the neuronal membrane.

The starting configuration of the lipid bilayer along with the tau fibril polymorphs are shown in Figure 4.1. The proportion of the individual lipid molecules is shown as a pie chart in Figure 4.1(b). We have taken the same starting configurations of the tau fibril over the neuronal membrane. We elucidate the differences in the tau morphology in the solution phase and the neuronal membrane from the atomistic simulations. The computa-

tional modeling presented here only accounts for the early stages of the tau interaction with the neuronal membrane. The entire event of the tau permeation through the neuronal membrane is beyond the scope of this study due to the limitations of the computational resources required for all-atom simulations using explicit solvation.

## 4.1 Methodology and simulation details

The systems modeled are composed of the PHF and SF tau fibrils taken from the PDB id 503L and 503T respectively, and were simulated in the aqueous phase and the neuronal membrane [118]. The cryo-EM structures are having a resolution of 3.4 – 3.5 Å and are derived from the brain of an individual having Alzheimer's disease. The SF and PHF fibrils are having eight zones of $\beta$-sheet regions with similar protofilament cores. The amino acid residues in the R3-R4 stretch are

[306]VQIVYKPVDLSKVTSKCGSLGNIHHKPGGGQ[336]

VEVKSEKLDFKD RVQSKIGSLDNITHVPGGGN[368]KKIETHKLTF[378]. The difference in the structure of PHF and SF stems from the difference in the lateral contacts at the dimer interface. The initial configuration of the tau fibrils over the neuronal membrane are choosen in accordance to the experimental and computational reports taking into consideration the affinity of the positively charged residues to bind over the anionic lipids [185, 186].

Hence, computational modeling of the dimer tau fibrils become important to account for the tau polymorphism. The PHF and SF fibrils are also simulated in the water box to compare with the neuronal membrane simulations. The neuronal membrane comprises 38% 1-palmitoyl-2-oleoyl-sn-glycero-3-phosphocholine (POPC), 24% 1-palmitoyl-2-oleoyl-sn-glycero-3-phosphoethanolamine (POPE), 5% 1-palmitoyl-2-oleoyl-sn-glycero-3-phospho-L-serine (POPS), 20% cholesterol (CHOL), 9% palmitoylsphingomyelin (PSM) and 4% monosialotetrahexosylganglioside (GM1) [187, 188, 189]. The ganglioside concentration

75
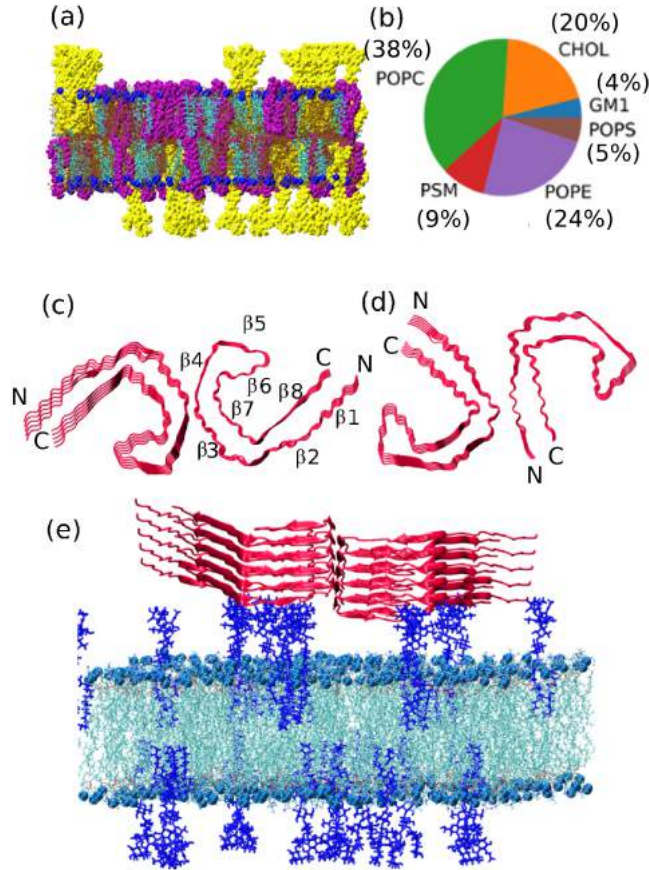
Figure 4.1: (a) The neuronal membrane with the phosphorus atoms, GM1 and PSM shown as blue, yellow and purple vdw spheres respectively, and cholesterol and other lipids shown as cyan and brown lines respectively. (b) the pie chart showing the composition of different lipids in the neuronal membrane, (c) the PHF structure shown in new cartoon representation with the different zones of $\beta$-sheet regions marked, (d) the SF structure, (e) the starting configuration of the PHF fibril above the neuronal membrane, where the GM1 lipids are shown as blue licorice, phosphorus atoms and other lipids are shown in blue and cyan respectively.

of the neuronal membrane used by Nguyen et al. [190] is lower by 3-4%. Though the neuronal membrane composition used by Nguyen at al. had five lipid components, we used six lipid components in line with the neuronal membrane composition used by Strodel et al. The tau fibrils are modeled using the CHARMM-36m force field which is shown to perform best for the IDPs [191]. The neuronal membrane composition of symmetric lipid bilayers in the PHF structure is 247 POPC, 156 POPE, 130 cholesterol, 60 PSM, 33 POPS, and 26 GM1 molecules. The corresponding symmetric bilayers in the case of SF structure comprise of 209 POPC, 132 POPE, 110 cholesterol, 49 PSM, 28 POPS, and 22 GM1 molecules. We have modeled the neuronal membrane taking 550 lipids for SF and 652 lipids for PHF because the PHF fibril required larger number of lipids for packing. To alleviate this discrepancy in the number of lipids used for the tau polymorphs we have normalised our results per number of lipid molecules. The bilayers are generated using the CHARMM-GUI membrane builder [154]. The membranes are comprised of layers of water molecules above and beneath the upper leaflet and lower leaflet of the bilayer.

The fibrils are modeled using the CHARMM-36m force field and the lipids are modeled using the CHARMM-36 force field [77, 159]. The all-atom simulations have been performed using the GROMACS molecular dynamics software (version -5.1.4) [155]. The systems were initially energy minimized using the steepest descent algorithm to negate the unfavorable contacts. This was followed by the six steps of equilibration as prescribed in the default CHARMM-GUI input generation. Finally, systems were equilibrated in the NPT ensemble and the production runs were carried out for 1 $\mu$s. The pressure is maintained using the semi-isotropic Parrinello-Rahman pressure coupling scheme [81]. The temperature is maintained using the Nosé-Hoover thermostat [161]. The periodic boundary condition (PBC) is applied in all directions. Particle Mesh Ewald (PME) is used to model long-range electrostatics [79]. The van der Waals and coulombic cutoff are set to 1.2 nm. The van der Waals interactions are modeled using the force switch algorithm. All the bonds involving

hydrogen atoms were restrained using the LINCS algorithm [162]. Water and chloride ions were used to dissolve and neutralize the protein-lipid systems. The water molecules have been modeled using the TIP3P water model [158]. Additional 150 mM of KCl was added to model the physiological salt concentration. Two additional simulations of 100 ns each have been performed in case of both the PHF and SF systems. Control simulations of 500 ns were performed in the water phase with PHF and SF. These simulations are also complemented with two independent simulations of 100 ns each. Similarly, neuronal membrane without the tau fibril is simulated taking 200 lipids in total. The pure neuronal membrane simulations have been performed for 500 ns each with two independent starting configurations. Further details of the simulated systems are given in Table 4.1.

Table 4.1: The details of the simulated systems

| System | Number of lipids | Composition of lipids | Number of atoms | Simulation time |
|---|---|---|---|---|
| SF neuronal membrane | 550 | 22GM1 + 110 CHOL + 209 POPC +49 PSM + 132 POPE + 28 POPS | 293204 | $1\mu s$ $2 \times 100$ ns |
| PHF neuronal membrane | 652 | 26 GM1 + 130 CHOL + 247 POPC + 60 PSM + 156 POPE + 33 POPS | 369949 | $1\mu s$ $2 \times 100$ ns |
| pure neuronal membrane | 200 | 8 GM1 + 40 CHOL + 76 POPC + 18 PSM + 48 POPE +10 POPS | 69580 | $2 \times 500$ ns |
| SF water | – | – | 332578 | 500 ns $2 \times 100$ ns |
| PHF water | – | – | 393430 | 500 ns $2 \times 100$ ns |

All the analyses have been carried out with the data from the entire span of 1 $\mu$s or 500 ns unless mentioned otherwise.

The analysis codes have been written using MDAnalysis python library and *gmx* tools. Clustering analysis was done using the GROMOS algorithm with the RMSD cutoff of 0.2 nm [163]. Bilayer thickness is calculated from the average position (perpendicular to interface) of the phosphate groups in both the leaflets. The number of contacts are calcu-

lated between the tau fibril residues and each of POPC, POPS, POPE, PSM or GM1 lipid. A contact is defined when the distance between any two non-hydrogen atoms from the residue and lipid in question is within 1.0 nm.

## 4.2 Results and Discussion

### 4.2.1 Structural Features

The polymorphic tau fibrils show differential stability due to the change in the environment in going from the neuronal membrane to the water medium. SF-neuron and PHF-neuron refers to the neuronal membrane simulations and SF-water, PHF-water refers to the simulations in the water medium. To characterize the structural stability, we have calculated root mean square fluctuations (RMSFs) of the C-$\alpha$ residues of the tau fibril, which are shown in Figure 4.2(a).

The neuronal membrane decreases the structural fluctuations of both the PHF and the SF polymorphs of the tau fibril when compared with the simulations in water. The compaction of the tau proteins in the lipids when compared to the water medium is in accordance with the experimental reports published on the model lipids [123, 192]. The RMSF of the PHF is less than that of the SF structure conforming to the fact that the PHF structures are more stable than the SF structures [148]. We have also calculated the angle of coverage, subtended by the three residues as shown in Figure 4.2(b). The angle defines the characteristic 'C' shape of the PHF and SF structures of tau as shown earlier [34]. The most probable angle of coverage for PHF in the water medium is 56°, and in the neuronal membrane it is 53° with a small distribution at 88°. In the neuronal membrane with SF, the angle of coverage is peaked at 57° with a smaller distribution at 106°. In case of SF in water medium, the peak is observed at 39° with a small distribution at 48°. The corresponding angle for the PHF and the SF structures in the cryo-EM structures are 58° and 57° respectively. Thus we infer that

79
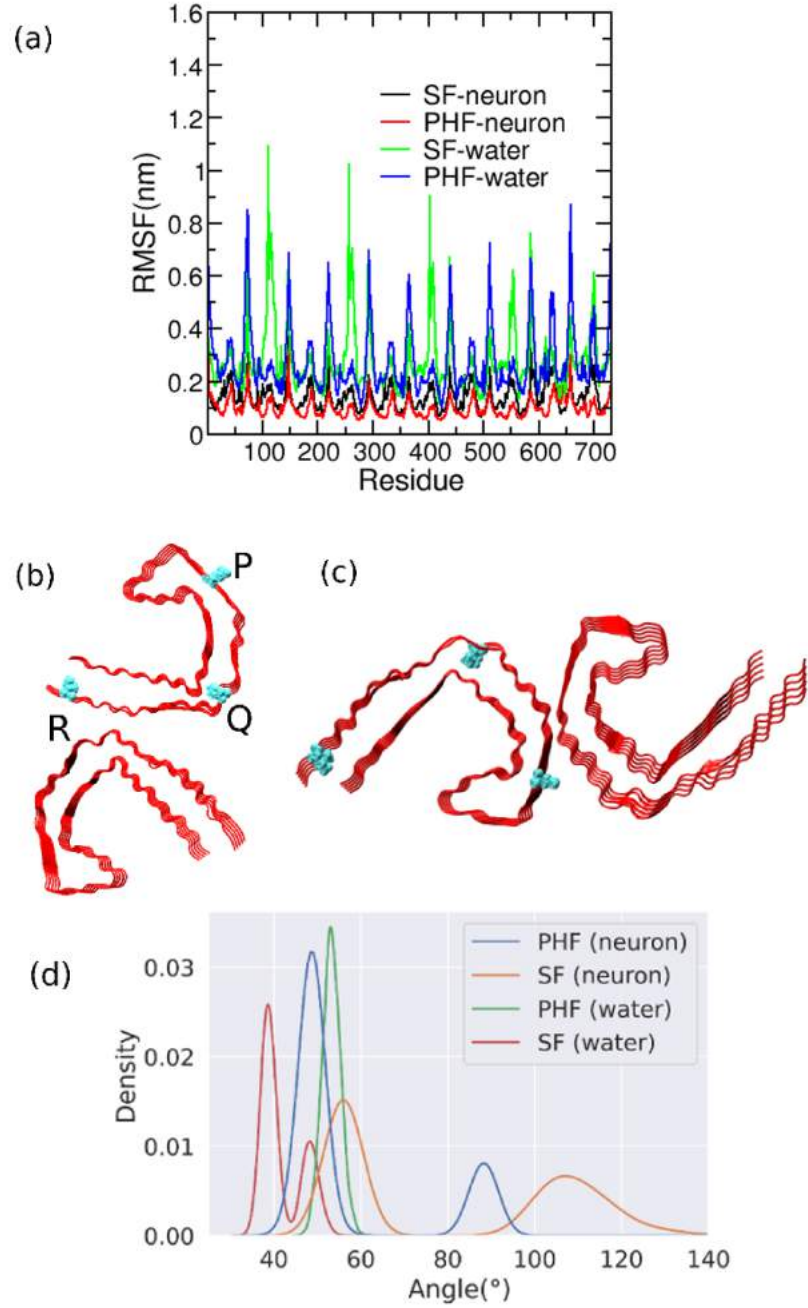
Figure 4.2: (a) RMSF of the C-$\alpha$ atoms of the residues of the tau fibril in the presence of neuronal membrane and in the water medium. (b)-(c) Pictorial representation of the angle of coverage ($\angle$PQR) and (d) the distribution of the angle of coverage in various systems.

the PHF structures conserve their "C"-shaped structure more than the SF strutures in going from the neuronal membrane to the water medium. The identification of the characteristic "C"-shape of in-vitro tau assemblies using cryo-EM is important for studying a multitude of tauopathies as pointed by Goedert and Scheres group [193, 194].

The positively charged residues interacting with the lipid bilayers are shown to be important for the fibril-membrane interaction. This has been established in the earlier studies related to the A$\beta$ protofilament [143], model peptides [195] and the hIAPP fibrils [165]. The coulombic interactions are found to be important factors for fibril-lipid headgroup binding. It has also been found experimentally that the negatively charged DMPG membranes show differential binding with the charged and acetylated N-terminus of the tau hexapeptide [132]. Also, the attachment of the human tau on the human brain lipid membranes are dependent on the cation present providing evidence of the electrostatic forces governing the interaction [125]. Sodium (Na$^+$) is found to facilitate the attachment, whereas potassium (K$^+$) inhibits the process. Hence, it has been proven that the coulombic interactions are pivotal to the tau-membrane interactions and the associated toxicity.

The distance profile of the positive charged residues with the P atoms of the bilayer as a function of time are shown in Figure 4.3. The positively charged residues are shown in blue surface representation. The mean distances of the positively charged PHF residues with the P atoms of the headgroups are shown to be less than that of the SF structures. T

To study fibril membrane interaction, we calculated the two-dimensional profiles for the fibril – lipid and intra-fibril contacts to the fibril approach distance, which is shown in Figure 5.10. The fibril – lipid contacts are normalised with respect to the total number of lipid molecules. The approach distance is calculated as the distance along z-axis between the center of mass of the membrane and that of the fibril. PHF is more closer to the neuronal membrane than the SF structure. The average number of fibril-lipid contacts are found to increase with closer approach of the fibril to the bilayer. The PHF approaches closer to the
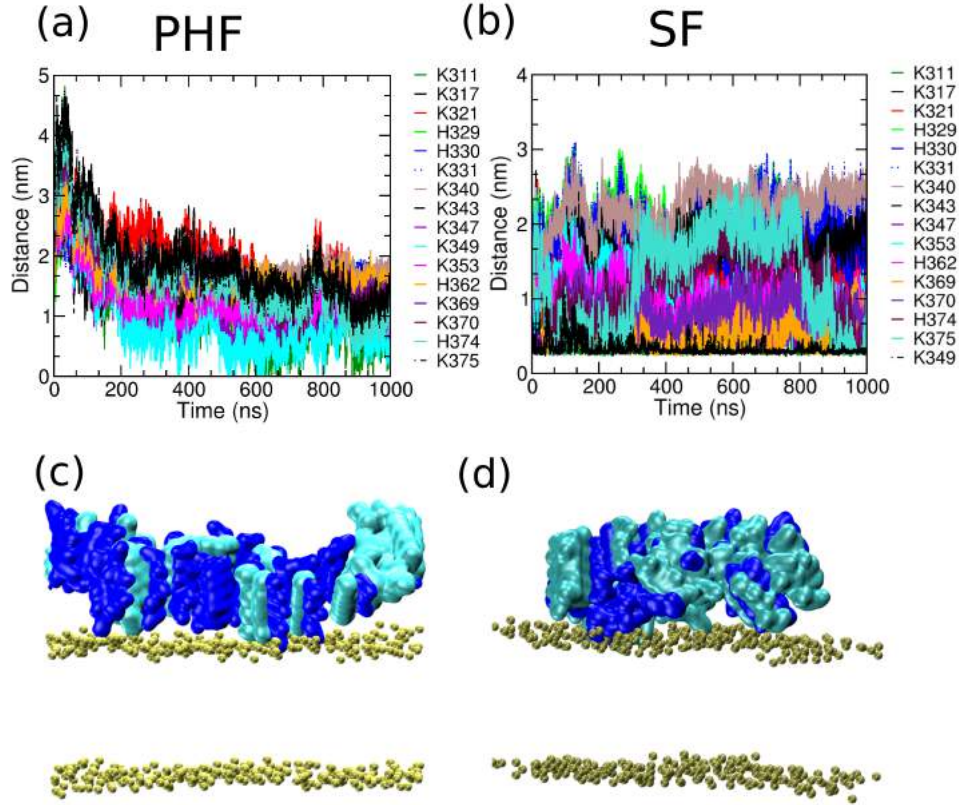
Figure 4.3: (a)-(b) are the distance profiles of the positively charged residues of the tau fibril with the phosphorus atoms of the lipid head groups. (c)-(d) are the representative tau fibril conformations showing positively charged residues in blue surface representation and other groups in cyan surface representation.

bilayer than the SF fibril. In the SF structure, the distribution of the fibril-lipid contacts and the approach distance are broader. Thus, we infer that in the timescale of our simulations, PHF has more fibril-lipid contacts, which results in the closer approach to the membrane. PHF also shows a higher number of intra-fibril contacts at a smaller approach distance compared to the SF structure. The higher number of intra-fibril contacts suggests higher stability of PHF structure with respect to the SF structure with the concomitant approach of the tau fibril towards the neuronal membrane.
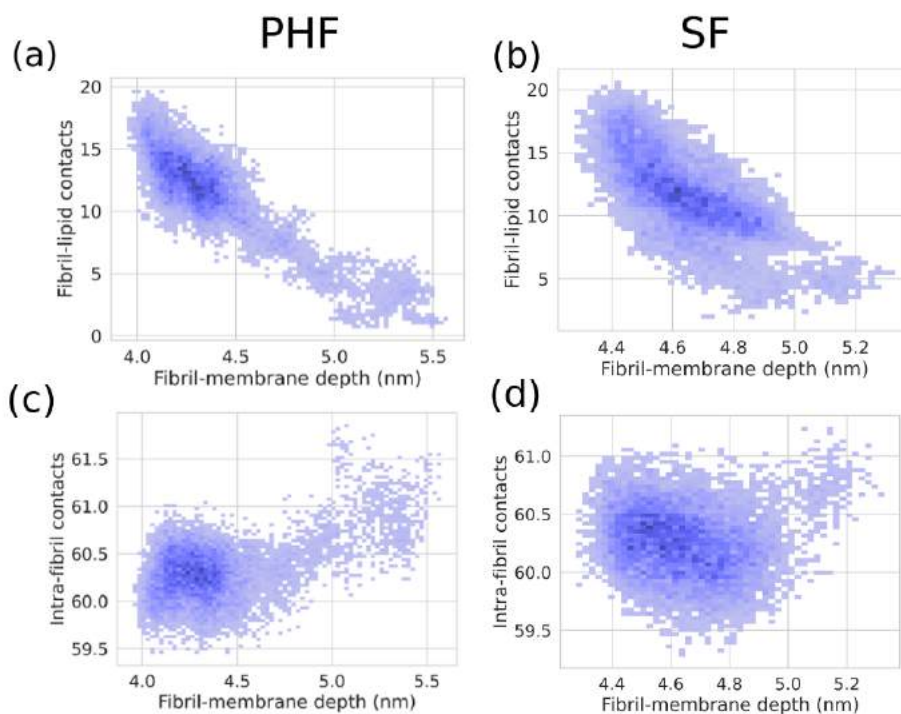
Figure 4.4: The two dimensional depth profile of the fibril center of mass along the z-axis and the fibril – lipid and intra-fibril contacts. (a) and (c) are the profiles of fibril – lipid and intra-fibril contacts respectively with the approach distance for PHF and (b) and (d) are corresponding graphs for the SF structures.

## 4.2.2 Radius of Gyration ($R_g$) and Solvent Accessible Surface Area (SASA)

To further characterize the conformational dynamics of the tau fibrils over the neuronal membrane and in the water medium, we have studied the radius of gyration ($R_g$). The distribution of the radius of gyration for the tau structures in the neuronal membrane and the water medium are shown in Figure 4.5. The straight filament structures show a larger deviation in the radius of gyration values in the water medium compared to the neuronal membrane. In comparison, the paired helical filaments show a more conserved conformational ensemble in the neuronal membrane and the water medium. This is in accordance with the results obtained in the earlier RMSF values which show that the PHF structure is

more stable than the SF structure. The higher flexibility of the SF structure in turn leads to the increase in the radius of gyration ($R_g$) compared to the PHF structure.

The solvent accessible surface area (SASA) is calculated using a probe radius of 0.14 nm to trace the effect of neuronal membrane on the tau fibril polymorphs. The distribution of the SASA values are shown in Figure 4.5(b). The SF structure is more soluble than the PHF structure in the presence of the neuronal membrane. The SF structure is also marginally more soluble in the water medium than the PHF structure. The distribution of the SASA values is broader in the water medium than in the neuronal membrane. The difference of the SASA values of SF structure in water and neuronal membrane are minimal with the mean value of SASA being 355.51 nm$^2$ in water and 353.33 nm$^2$ in neuronal membrane. The corresponding values for the PHF structures are 345.90 nm$^2$ and 344.61 nm$^2$ respectively, in the water medium and the neuronal membrane. Thus, the influence of the neuronal membrane on the SASA values compared to the pure water medium is negligible. The SF structure has higher SASA with respect to the PHF structure.

### 4.2.3 Dimer Interface and Cation-$\pi$ contacts

The core residues of the PHF and SF structures are the same. The polymorphism arises from a difference in the dimer interface. The dimer interface of the PHF and SF fibrils is stabilized by a few specific amino acid residues. The important amino acid residues with the intra-residue distances between them are shown in Figure 4.6(a)-(b). The residues L315, K317, K321 are the primary residues at the SF dimer interface. In the PHF dimer interface, the saltbridge interactions between K331–E338 and the residues G334 play important role in stabilizing the fibril. The distance profiles between the dimer residues are shown in Figure 4.6. The cation $-\pi$ interactions between the I308–Y310 residues play an important role in the tau stabilization and self-assembly as shown from the earlier experimental reports [196, 197]. As a key residue of the steric zipper PHF6 fragment, Y310 plays an
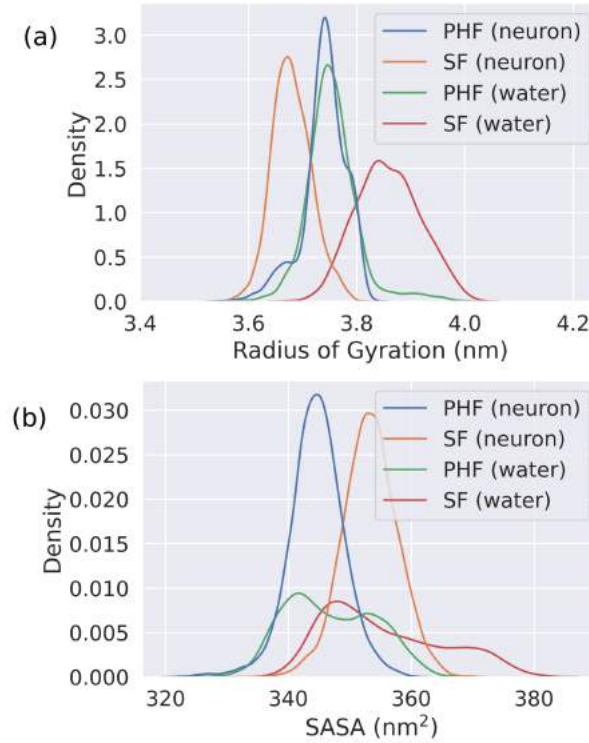
Figure 4.5: Distribution of (a) radius of gyration ($R_g$) and (b) solvent accessible surface area (SASA in $nm^2$) for the tau fibrils in the neuronal membrane and water medium.

important role in tau fibrillization [198, 146, 199]. The cation $-\pi$ contact is defined if the distance between the isoleucine and tyrosine residue is within 0.6 nm.

Our results have shown that in the case of the SF dimer, the dimer interface consisting of L315–K321 has a distance of 0.935 nm in the cryo-EM structure. The average L315–K321 distance changes from 0.860 nm in the neuronal membrane to 0.783 nm in the water medium. The distance between K317–K321 also decreases in going from the neuronal membrane (1.31 nm) to the water medium (1.26 nm). The corresponding cryo EM distance in the pdb structure is 1.213 nm. Hence, the cryo EM distances for the interface residues change in the MD simulations both in the neuronal membrane and water medium. The L315–K321 distance decreases whereas, the K317–K321 distance increases from its value in the cryo EM structure.

In the PHF structures, G334–G334 distance in the cryo EM structure is 0.599 nm, whereas the distance in the neuronal membrane and water medium are 0.458 nm and 0.484 nm, respectively. That is, G334–G334 distance decreases both in the case of the neuronal membrane and the water medium. For the salt bridge interactions between K331–E338 residues, the distance between the $NH_3^+$ and $COO^-$ groups in the cryo EM structure is 0.693 nm which changes to 0.423 nm in the neuronal membrane and 0.371 nm in the water medium. Thus, the saltbridge interaction increases in both the neuronal membrane and the water medium. Hence, in the MD simulations in both the neuronal membrane and the water medium; the intra-residue distances in the dimer interface change in both the tau polymorphs. Moreover, the PHF dimer interface is strengthened by the decrease in the intra-residue distance in the neuronal membrane and the water medium compared to the cryo EM structure.

## 4.2.4 Secondary Structure Content

The molecular dynamics simulations of the IDPs shed light on the secondary structure content [184]. The choice of the appropriate force field along with the choice of the water model used in molecular dynamics simulations influence the secondary structure of the IDPs [200, 201, 202]. As shown from the earlier studies with regards to the A$\beta$ monomer and fibril structures, secondary structure content is dictated by the nature of the interaction with the bilayer membranes[33, 142, 203, 204]. In the neuronal membrane, the $\beta$-sheet structures are reduced in the case of SF structures whereas $\beta$-sheet content increases in the case of PHF structures as shown in Figure 4.7A. There is nearly a 8% decrease in the $\beta$-sheet content in case of PHF structures in the water medium compared to the neuronal membrane whereas in case of SF structure, the $\beta$-sheet content increases nearly 8% in going from neuronal membrane to the water medium. The cryo-EM structure of the tau fibril cover the residues V306–K311 in $\beta$1, V313–C322 in $\beta$2, N327–K331 in $\beta$3, Q336–S341 in $\beta$4, K343–K347 in $\beta$5, R349–I354 in $\beta$6, S356–V363 in $\beta$7 and N368–F378 in $\beta$8. Thus, these
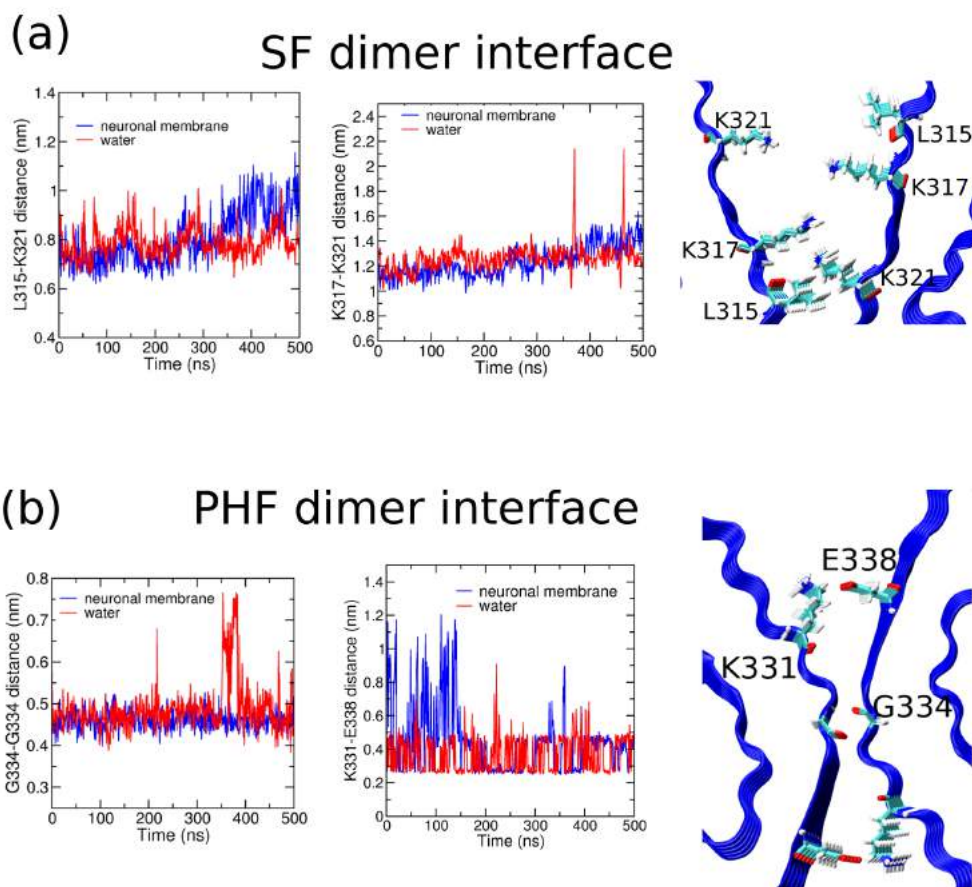
Figure 4.6: The primary amino acid residues at the dimer interface of the (a) SF and (b) PHF fibrils.

eight zones of $\beta$-sheet residues are studied using the DSSP utility in $gmx$. The residue-wise propensity of the secondary structures are shown in Figure 4.7B(a-d) for the tau structures in the neuronal membrane and aqueous medium. The decrease in the $\beta$-sheet content in the water medium for the PHF structure is seen prominently at the C-terminal regions. This decrease of the $\beta$-sheet content leads to the concomitant increase in the coil conformations. Similarly, in the SF structures, the $\beta$-sheet content is increased in the C-terminal region along with the increase of the coil conformations. It is to be noted that the C-terminal region is spanned by the $\beta$8 region of the tau between N368–F378 residues in the cryo-EM structures which shows maximum changes in going from the neuronal membrane to the

87

aqueous medium.

The experimental results show contrasting behavior regarding the secondary structure content on tau fibril binding to the lipid membranes. The tau K19 protein interacting with vesicles show the formation of helices in the R3–R4 domain [205]. The formation of the $\alpha$-helix conformations might be observed at much larger timescales, or the absence of R1 region might be limiting the biophysical modeling. On the contrary, the hexapeptide fragment (PHF6) shows the formation of the $\beta$-sheet structures in complexation with the dissolved lipids containing negatively charged DMPG lipids[132].

## 4.2.5 Number of Contacts

To characterize the fibril – lipid interactions, we have calculated the number of contacts per lipid molecule in the neuronal membrane which is shown in Figure 4.8(a)-(b). The contact is defined using a cutoff of 1.0 nm between the atoms of the protein molecule and the lipid molecules. The GM1 lipids show most number of contacts with PHF structure. The second highest contacts with PHF are observed for POPC lipids. In case of the PHF structure, the number of contacts between the fibril, and POPC and GM1 lipids are 64.93 and 72.61 respectively. PSM and POPS lipids have the least and second lowest number of contacts with the PHF fibril with the values of 10.19 and 13.17 respectively. The most number of contacts in SF structure are found in case of negatively charged GM1 lipids (53.61), followed by POPC lipids (57.80). The number of contacts for the zwitterionic PSM and negatively charged POPS are 18.94 and 17.08. Thus, the GM1 and POPC lipids preferentially interact with both the tau polymorphs in the neuronal membrane.

To further resolve the interaction of the tau fibrils with the GM1 lipids, the number of contacts between the neuraminic acid and the sugar molecules were determined and are shown in Figure 4.8(e). The number of contacts for the neuraminic acid and the sugar groups are normalised with respect to the total number of GM1 lipids present in the two systems.
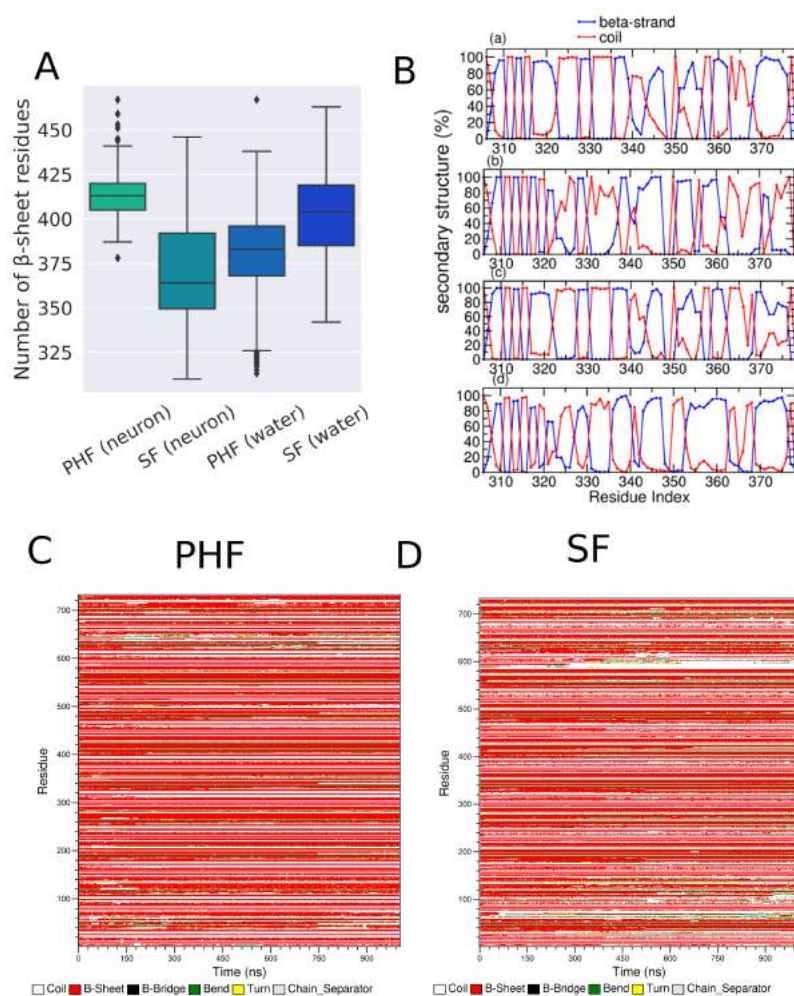
Figure 4.7: (A) The total number of $\beta$-sheet residues in the four systems, shown in a box and whisker plot. (B) (a)-(b) are the plots showing the average residue-wise secondary structure propensity in case of PHF and SF structures in neuronal membrane and (c)-(d) are the average secondary structure propensities for the PHF and SF structures in the water medium. (C)-(D) are the DSSP timelines for the PHF and SF structures in the neuronal membrane.

The representative snapshot of GM1 lipid showing the sugar molecules and the neuraminic acid is given in Figure 4.8(f). The sugar molecules show only a small increase (nearly 10 %) in the number of contacts with the tau polymorphs compared to the neuraminic acid. The large number of contacts in case of the GM1 lipids are due to its protein localization ability through the formation of suitable carbohydrate-amino acid interactions. The GM1

lipids with their sugar groups can anchor the tau filaments over the membrane thus inducing higher number of contacts as shown in Figure 4.10(d)-(e). Our findings are also consistent with the earlier reports related to the role of GM1 lipids in the amyloid $\beta$ and $\alpha$-synuclein aggregation [206, 207, 208, 32].

The most populated structure generated from the simulation trajectories through clustering algorithm are shown in Figure 4.8(c)-(d). The PHF and SF structures are seen to interact with the neuronal membrane in a different manner. In the PHF structure, S324 is seen to interact with the phosphorus head group of the bilayer, whereas in the SF structure, positively charged R349 is found to interact with the phosphorus head group.

## 4.2.6 Hydrogen Bonding

To characterize the interactions between the tau fibril and the neuronal membrane, we have calculated the number of hydrogen bonds in all the systems. We have classified the hydrogen bonding according to the geometric criteria [90]. In a strong hydrogen bond, the hydrogen atom and the acceptor are separated by a distance less than 0.22 nm, and the angle made by the donor, hydrogen atom, and the acceptor is within the range $130° - 180°$. The corresponding distance and angular range are $0.2 - 0.3$ nm and $90° - 180°$, respectively, for a weak hydrogen bond. We did not find strong hydrogen bonding in any of the systems.

The hydrogen bonding numbers in the studied systems are given in Table 4.2. The intrafibril hydrogen bonding stabilizes the fibril and helps conserve the $\beta$-sheet. Thus, the variation in the tau fibril hydrogen bonding among the two polymorphs and in the two media follows similar trend as the number of $\beta$-sheet residues. The number of intrafibril hydrogen bonds decreases in going from the neuronal membrane to the water medium in the case of PHF structure, whereas it increases in the case of SF structure. The changes in the number of intramolecular hydrogen bonds are small in both the systems (3.38% and 0.47% in the PHF and SF structures respectively). The fibril-GM1 hydrogen bonding is predominant
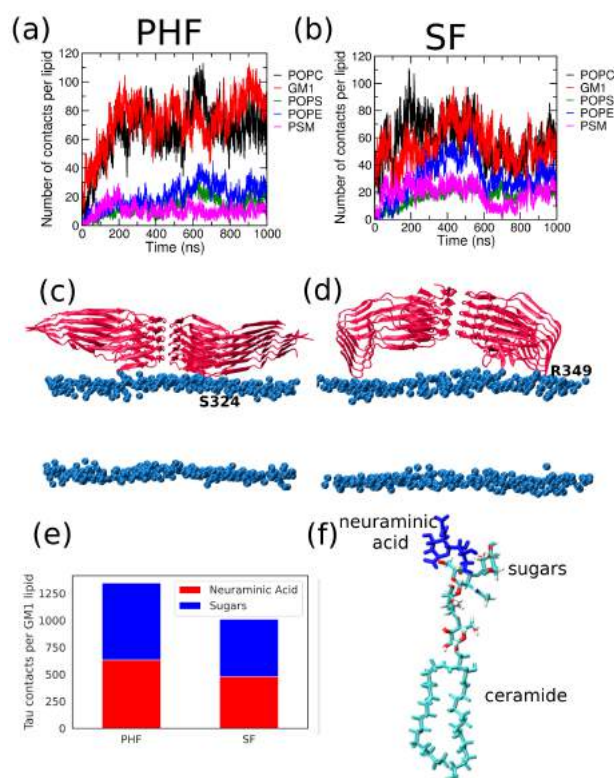
Figure 4.8: (a)-(b) are the number of contacts per lipid molecules for the PHF and SF structures. (c)-(d) are the most populated cluster for the tau fibril over the neuronal membrane obtained using the clustering algorithm. The protein is shown in new cartoon representation and the phosphorus headgroups are shown as blue VDW spheres. The interacting residues are marked in the figure for the two structures. (e) is the bar plot showing the number of contacts of the GM1 lipid groups with the fibrils per GM1 molecule. (f) show the individual groups within the GM1 lipids. The ceramide tail and neuraminic acid are shown in cyan and blue respectively.

91

which stabilizes the fibril-membrane interaction.

To further characterize the stability of the neuronal membrane, we calculated the hydrogen bonding between the lipid molecules which are shown in Table 4.3. The number of hydrogen bonds is averaged over all the lipid molecules. The pure membrane lipid molecules have less number of intra-lipid hydrogen bonds with respect to the tau fibril incorporated neuronal membranes. The intra-PSM hydrogen bonds are higher in number than the intra-POPS, intra-POPC and intra-POPE hydrogen bonds. This increase of hydrogen bonding within the PSM lipids in mixed membranes is also illustrated earlier [209].

Table 4.2: Number of hydrogen bonds observed in the studied systems. Fibril – lipid hydrogen bonds have been normalised with respect to the number of individual lipid components.

| | PHF | | SF | |
| --- | --- | --- | --- | --- |
| | Neuronal membrane | Water | Neuronal membrane | Water |
| intra-fibril | 613.54 | 592.79 | 582.98 | 585.75 |
| Fibril – GM1 | 0.462 | – | 0.385 | – |
| Fibril – POPS | 0.215 | – | 0.360 | – |
| Fibril – POPC | 0.018 | – | 0.021 | – |
| Fibril – POPE | 0.028 | – | 0.062 | – |
| Fibril – PSM | 0.008 | – | 0.042 | – |

Table 4.3: Number of intra-species hydrogen bonds among the lipid species for the different systems calculated per number of lipid molecules.

| | GM1 – GM1 | POPS – POPS | POPE – POPE | PSM – PSM | POPC – POPC |
| --- | --- | --- | --- | --- | --- |
| PHF | 4.12 | 0.28 | 0.37 | 0.96 | 0.44 |
| SF | 4.16 | 0.19 | 0.39 | 0.98 | 0.43 |
| pure membrane | 3.88 | 0.18 | 0.36 | 0.94 | 0.40 |

## 4.2.7 Contact Map

The analysis of the contact map of the residues are shown in Figure 4.9 for the water medium and the neuronal membrane in case of both the polymorphs. The contact maps are calculated through the intra-residue distances with the distance being shown in a colorbar. The residue contact maps show the difference between the tau ensemble conformation in the two
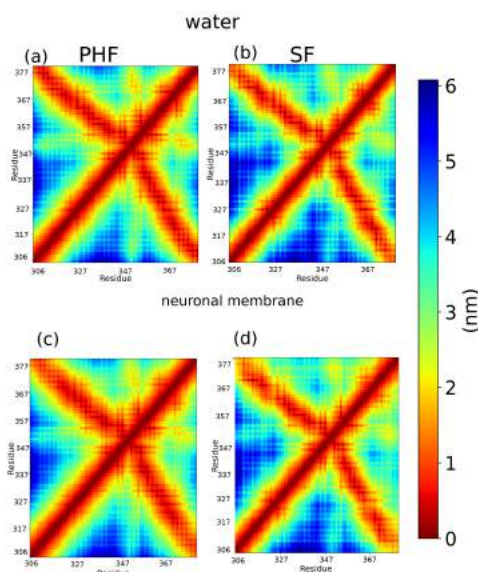
Figure 4.9: (a)-(b) are the residue-residue contact maps for the PHF and SF structures in the water medium. (c)-(d) are the contact maps in the neuronal membrane.

different environment. The structures are stabilized by the contact between far separated residues. The contact map show signature of the antiparallel $\beta$-sheet arrangement involving residues I308–F347 and residues K348–K370. These regions are dominated by the $\beta$-sheet regions in both the media. Additional V354–I372 contacts of the tau fibrils are less in the neuronal membrane compared to those in the water medium.

## 4.2.8   Bilayer Properties

It is difficult to study the effect of intrinsically disordered proteins on the membrane bilayer using conventional experimental techniques. Thus molecular dynamics simulations helps to elucidate the membrane protein interactions at an atomic resolution. To characterize the perturbations in the neuronal membrane due to the presence of the tau fibril over it, we have calculated the bilayer properties. The bilayer thickness in case of the tau incorporated membranes are similar to those of the pure membrane as shown in Table 4.4. The bilayer thickness is calculated by taking the headgroup to headgroup distance of the P-atoms in

Table 4.4: Bilayer thickness (nm) and the area per lipid ($nm^2$) in the neuronal systems and the pure neuronal membrane.

| | Bilayer thickness (nm) | Area per lipid ($nm^2$) |
|---|---|---|
| PHF | 4.497 | 0.573 |
| SF | 4.495 | 0.569 |
| Pure membrane | 4.496 | 0.641 |

POPC, POPS, POPC, and PSM. The two dimensional bilayer thickness projected over the bilayer plane is shown in Figure 4.10(a)-(b). The area per lipid of the tau incorporated membranes is lower than that in pure membrane system. The change in bilayer thickness is negligible upon the incorporation of the tau fibrils. The cholesterol tilt angle is calculated taking the angle subtended by the C3–C17 carbon atoms of cholesterol with the bilayer normal.

The bilayer thickness has more uniform distribution in the presence of tau fibrils. In comparison, the bilayer thickness for the amyloid $\beta$ dimer over the neuronal membrane is calculated to be 4.65±0.03 nm by Fatafta *et.al* [33]. In general, we find that the bilayer properties like the bilayer thickness, cholesterol tilt angle show negligible change with the presence of the tau filaments. The relatively higher change in the bilayer properties is found in the area per lipid (APL). This result is found to be correlating with the earlier study concerning the amyloid $\beta$ dodecamer and fibril over the neuronal membrane [190].

### 4.2.9  Density Profile

The number density of the lipid components in the presence and absence of the tau polymorphs is shown in Figure 4.11. The density of the individual lipid molecules is projected over the bilayer plane and shown in a colorbar. Even without the tau fibrils the lipid molecules are distributed heterogeneously. GM1 tails (ceramide), POPS and PSM show distinct islands of high density. POPE and POPC lipids have a more uniform distribution. In case of POPE and POPC lipids, we observe large areas of high lipid distribution which
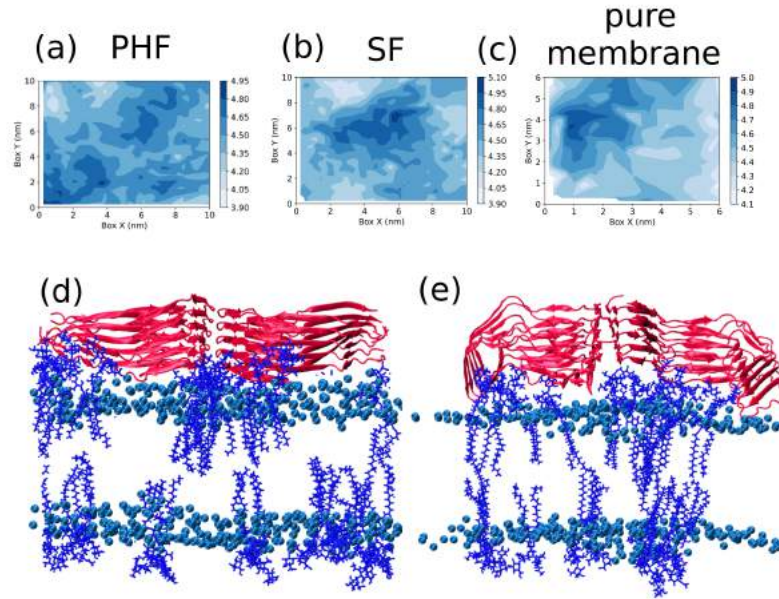
Figure 4.10: (a), (b), (c) are the two dimensional bilayer thickness projected over the bilayer plane for PHF, SF and pure membrane respectively. (d) and (e) are the final snapshots of the PHF and SF structures over the neuronal membrane respectively. The GM1 lipids are shown in blue licorice representation, phosphorus atoms are shown as VDW spheres and the tau fibril is shown in new cartoon representation.

results in uniform distribution of lipid molecules in the bilayer membrane.

With the incorporation of tau fibril, the distribution of the lipid molecules is altered especially of the GM1 tails and POPS lipids. GM1 tails tend to cluster more in the absence of tau fibril. The distribution of cholesterol (CHOL) becomes even with the incorporation of tau fibril. The distribution of the lipid molecules is different in case of the PHF and SF structures. For the GM1 tails, the distribution is more widespread in the case of the PHF fibrils than the SF fibrils. The interaction of the tau fibrils with the neuronal membrane decreases the relatively broader distribution of the lipids. Hence, we conclude that the distribution of the lipid molecules over the bilayer changes in the presence of the tau polymorphs. Our results are consistent with the earlier studies related to the $A\beta$ proteins over the neuronal membrane.[33, 190]
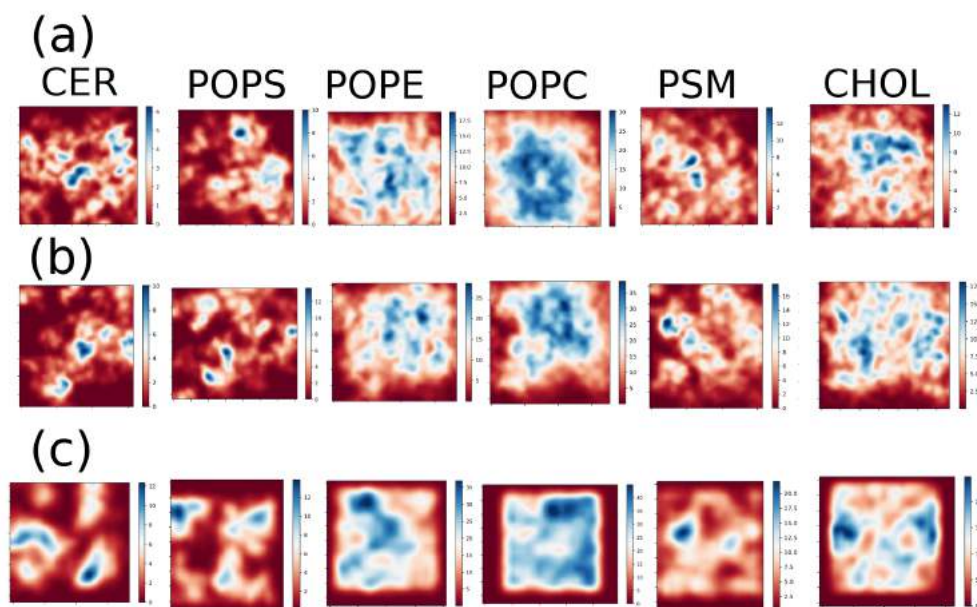
Figure 4.11: The density distribution of the lipid molecules projected over the bilayer plane in case of neuronal membrane with (a) PHF polymorph and (b) SF polymorph, and (c) pure neuronal membrane. The relative density is shown as a colorbar.

## 4.3 Conclusions

Tau proteins have emerged as the important contributors to the tau pathogenesis. The impact of the tau fibrils on the neuronal membrane is pivotal to the understanding of the neuronal toxicity. We aim to understand the effect of tau fibril polymorphs on the neuronal membrane through all-atom molecular dynamics simulations. Control simulations have been performed on the pure neuronal membrane and the tau fibrils in water box. This is the first report of computational modeling aspiring to study the effect of tau fibrils on three or more lipid molecules forming the bilayer. The paired helical filament (PHF) in general show higher stability in the neuronal membrane compared to the straight filament (SF) structure as shown from the structural analyses. The tau binding over the neuronal membrane is predominantly due to the GM1 lipid molecules interacting with the tau fibril. The PHF structure is also found to be more compact in both the neuronal membrane and the water

medium. The use of the entire cryo-EM structure for the initial configuration helps us to understand the changes that occur in the fibril interface of the PHF and the SF structures in aqueous solution and neuronal membrane. PHF and SF structures in the neuronal membrane show distinct differences in the number of $\beta$-sheet residues when compared with the simulations in the water medium. In the timescale of our simulations, we find that among PHF and SF, the PHF approaches closer to the neuronal membrane. There is a marked difference in the distribution of the lipid molecules in the presence of PHF and SF structures over the neuronal membrane. Overall, our study helps to describe the atomistic interactions responsible for the tau fibril binding to the neuronal membrane. Even though more extensive computational sampling starting with different initial conformations are required to unravel the fibril insertion into the membrane, the current study captures the disparate behavior of the tau polymorphs over the neuronal membrane. This in turn leads to pertinent questions like how the various set of polymorphs cause different tauopathies, which will require further studies despite a plethora of published literature on this field.

# Chapter 5

# Phosphatidylinositol (PI) Lipids Modulate the Binding of Tau Fibrils on Lipid Bilayers

Neurodegenerative diseases like Alzheimer's disease (AD), Pick's disease, frontotemporal lobar degeneration, and progressive supranuclear palsy are all characterized by aggregation of tau protein [210, 114]. The collective term for all such diseases is tauopathies. The tau protein polymerizes tubulin into microtubules (MTs) and provides axonal support to the microtubules [211]. Tau protein undergoes phosphorylation in post-translational modification, but sometimes hyperphosphorylation occurs when the concentration of phosphates is almost three times that of a healthy brain [212, 115]. The abnormal increase in phosphate concentration hinders the association of tau protein with microtubules and results in the aggregation of tau into paired helical filaments (PHF) and neurofibrillary tangles (NFT) [116].

ADs are characterized by the formation of plaques which contain aggregates of amyloid beta peptides and aggregates of tau in the form of NFTs. Research on AD is now being focussed on tau after amyloid beta targeting treatments failed in clinical trials [117, 213]. Broadly tau has four domains, the N-terminal domain, the proline rich domain, repeat domain region and the C-terminal domain. Adult brain has four repeat domains (4R tau) and the R3 and R4 repeat domains form the core of for paired helical filament (PHF) and straight filament (SF) [119]. PHFs and SFs comprise of two protofilament cores with C-shaped subunits in different conformation, as elucidated by the cryo-EM structure by Fitzpatrick and coworkers [118].

Studies suggest that tau interacts with the plasma membrane (PM) from its N-terminal

and aggregation of tau is promoted by the PM in vitro, however, the mechanism is un-known [121, 214, 122, 192]. Membrane lipids like phosphatidylcholine (PC), cholesterol, and sphingolipid have been observed to be associated with tau proteins [131, 215]. Stud-ies suggest that anionic lipid bilayers have a greater possibility of fibril formation in tau and A$\beta$ proteins [216, 217, 123]. Phosphatidylinositol 4,5-bisphosphate (PIP$_2$), which is an anionic lipid, is of great interest in the study of aggregation of tau proteins. In an ear-lier work, tau and PIP$_2$ binding has been reported, though structural information regarding the binding of tau over PIP$_2$ lipid was absent [218]. A more recent experimental study has shown that PIP$_2$ induces aggregation of repeat domains of the tau protein and increases the random coil content in the tau protein [181]. Phosphorylation of the phosphatidylinositol (PI) molecule at the 3, 4, and 5 positions of the inositol gives rise to seven different phos-phoinositide derivatives. PIP$_2$, a major form of phosphorylated PI, is a signaling lipid that facilitates the binding of intracellular proteins to membranes. PIP$_2$ has a negatively charged inositol headgroup which can accommodate a negative charge of up to (-5), although (-3) or (-4) charge is observed in some cases [219]. The mammalian cell membrane has around 5-10% of PIs and even though it is not a major component, it serves many important biolog-ical purposes like controlling the cell death [220]. PIP$_2$ is also involved in the generation of messenger molecules, membrane trafficking and membrane protein interaction, protein-protein interactions and protein oligomerization [221, 222, 223, 224]. PI lipids are found to significantly influence the dynamics and the structure of the PC membranes [225]. An experimental study has shown that PIP$_2$ induces aggregation of repeat domains of the tau protein and an increased number of random coil content in the tau protein [181].

Molecular dynamics simulations have paved the way to study the interaction of interac-tion of lipid bilayers with amyloid fibrils [141]. MD studies also show that in zwitterionic lipids, the interaction of bilayer and protein is mostly coulombic [143]. However, most of the works on protein-membrane have been done on amyloid beta fibrils. MD simulation

studies on tau fibril are still lacking involving the lipid bilayers. MD study of the full-length tau fibril was done by Nussinov group but without any lipid bilayer [148]. In our earlier work, we studied the effect of cholesterol in lipid bilayer on the interaction of tau fibril with differently charged lipid molecules [34]. Also we have studied the effect of tau polymorphs on the model neuronal membrane comprisiong of six different lipid components [226]. But due to the lack of study on the effect of PI lipids on the interaction of tau fibril with the lipid bilayer, we carried out all-atom and coarse-grained molecular dynamics simulations taking a similar starting configuration.

# 5.1  Methodology and simulation details

## 5.1.1  Coarse-grained simulations

Martini is used to model the lipids and tau protein for coarse graining. Martini model 2.0 and 2.2 is used to model the lipids and the proteins respectively, using CHARMM-GUI [154]. The simulations are run using the parallelized GROMACS (v-2019.4). The systems were initially energy minimized and then subsequently equilibrated in six steps restraining the proteins and lipids. Electrostatics and Lennard Jones cut-off was set upto 1.1 nm with the reaction field method and potential shift Verlet method respectively. The initial velocities of the simulations were choosen from a Maxwell distribution at 310K. The temperature and the pressure for the production run was kept constant using v-rescale thermostat and Parrinello-Rahman barostat. The coupling constant of v-rescale thermostat was 1 ps and the coupling constant of the Parrinello-Rahman barostat was 12 ps. The production runs were performed for 5 $\mu$s with a time step of 20 fs. Electrostatic interaction was modelled using the reaction field method using the dielectric constant of 15. The inital velocities are taken from the Maxwell distribution at 310 K. The final production runs were run using the v-rescale thermostat having a coupling constant of 1 ps and Parinello-Rahman barostat with

a coupling constant of 12 ps.

## 5.1.2   All-atom simulations

The initial structures of the protein were taken from the pdb ids 5O3T and 5O3L. The proteins have been modelled using the CHARMM-36m force field. CHARMM-36m is shown to perform best for the PHF6 motif of the tau peptides among a series of force fields [77, 191]. The simulations were performed using the GROMACS MD code (version-5.1.4) [155]. The fibril was initially placed above the lipid bilayers containing $PIP_2$ in the ratio of 9:1 lipid:$PIP_2$. The water model TIP3 is used along with the additional 0.15(M) KCl to maintain the physiological conditions. The lipid molecules and $PIP_2$ were modelled using the CHARMM-36 parameters developed by Klauda et al [227, 159]. Lipids were subjected to six steps of equilibration (by applying restraints on proteins and lipids subsequently) after the initial energy minimization following the CHARMM-GUI protocol [154, 228]. The final production runs were performed at the temperature of 310K using the Nosé-Hoover thermostat using the coupling constant of 1.0 ps. Production runs were performed in the NPT ensemble for 200 ns using the time step of 2 fs. Long ranged electrostatics were modelled using the Particle Mesh Ewald (PME) with a cut-off of 1.2 nm [79]. Force switch function was used to model the long range interactions. The bonds with the hydrogen atoms were restrained using the LINCS algorithm [162].

For the water box simulations, the polymorphs (SF and PHF) of the tau fibrils are packed in a cubic box with edge length of 1.4 – 1.5 nm. The water box simulations are also run using GROMACS (v-2019.4).

Pure lipid systems without the protein are modelled using 200 lipid molecules in the ratio of 9:1 of the POPC/POPG and PI lipids. The lipids are packed symmetrically with 100 lipids in both the upper and the lower leaflet. The bilayer models were generated using the CHARMM-GUI Membrane Builder. 200 ns of trajectory was generated from the

production runs in the NPT ensemble at 310 K and 1 bar. All the analyses were done using *gmx* tools and using in-house scripts invoking MDAnalysis python module using the entire length of the trajectory [229]. The PI clusters are calculated using DBSCAN (Density-based spatial clustering of applications with noise) algorithm from *sklearn.cluster* library. The distance cutoff of 1.5 nm is choosen to calculate the clusters.

### 5.1.3 System Description

We have simulated symmetrical lipid bilayers consisting of POPC/POPG + PI lipids. The tau lipids are placed above the lipid bilayers consisting of PI lipids in accordance with the earlier studies [34]. To increase the configurational sampling we have replicated the simulations twice. The results are calculated as the average of these two simulations. Further details of the simulated systems are given in Table 5.1. The lipids are having a composition of POPC/POPG and PI lipids in the ratio of 9:1. In the subsequent discussion, PC, PG and PI are used to refer to POPC, POPG and $PIP_2$ lipids, respectively. The structures of straight filament and paired helical filament are shown in Figure 5.1 (a)-(b) respectively. The fibril-lipid starting configuration is given in Figure 5.1(c), and the schematics of the lipid molecules used in our study are shown in Figure 5.1(d)-(f).
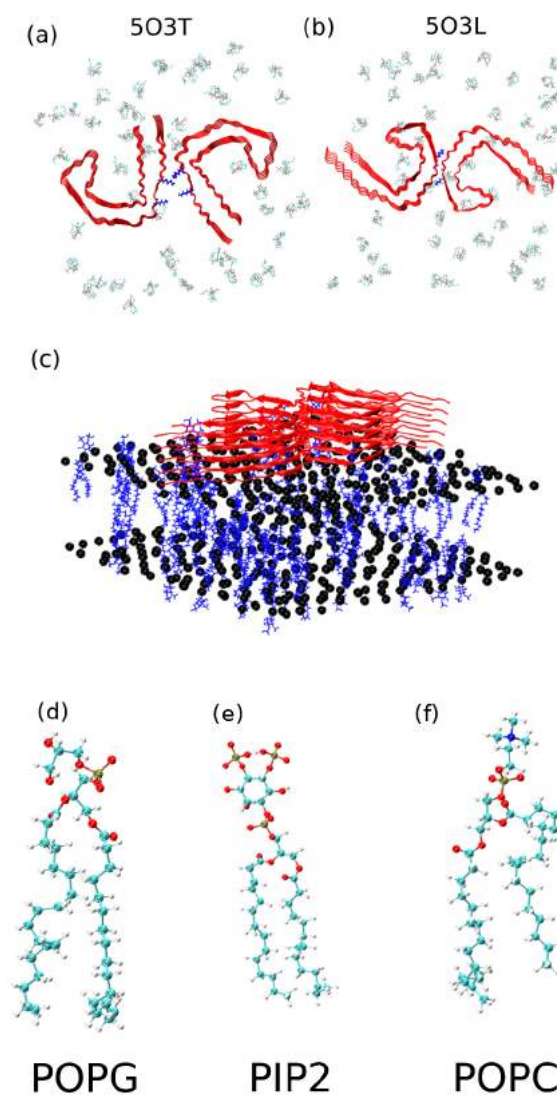
Figure 5.1: (a) and (b) are the straight filament (SF) and paired helical filament (PHF) corresponding to the PDB ids 5O3T and 5O3L respectively, along with the PI lipids as viewed over the top. The PI lipids are shown in lines representations in VMD. Residues K317, K321 of SF and the residues G334, Q336 of PHF are shown in blue. (c) is the initial configuration with the fibril and the PI lipids. The PI lipids are shown as blue sticks and the phosphorus headgroups of the POPC lipids are shown in black. (d)-(f) The schematics of the bilayer molecules used in our all-atom study. The nitrogen, phosphorus, carbon and oxygen atoms are shown in blue, grey, cyan and red, respectively.

Table 5.1: Summary of the simulations of tau fibrils in PI-containing and PI-depleted membranes.

| System description | Number of lipids | Number of waters | Production run | Number of atoms |
|---|---|---|---|---|
| All-atom (protein and lipids) | | | | |
| POPC+PIP$_2$ | 510 | 48414 | 200 ns $\times$ 2 | 225094 |
| | 600 | 94099 | 200 ns $\times$ 2 | 374443 |
| POPG+PIP$_2$ | 510 | 66184 | 200 ns $\times$2 | 275756 |
| | 600 | 30000 | 200 ns $\times$ 2 | 178524 |
| Pure Lipids | | | | |
| POPC+PIP$_2$ | 510 | 12088 | 400 ns | 63086 |
| POPG+PIP$_2$ | 510 | 11006 | 400 ns | 58754 |
| Tau-protein (water box) | | | | |
| — | — | 106819 | 500 ns | 332515 |
| — | — | 137356 | 500 ns | 424302 |
| Coarse-grained (protein and lipids) | | | | |
| POPC+PIP$_2$ | 510 | 15368 | 10 $\mu$s | 54972 |
| | 510 | 15562 | 10 $\mu$s | 56060 |
| POPG+PIP$_2$ | 510 | 14056 | 10 $\mu$s | 51463 |
| | 510 | 13904 | 10 $\mu$s | 51539 |

## 5.2 Results and Discussions

### 5.2.1 Tau Fibril Stability

The root mean square fluctuations (RMSFs) of the C-$\alpha$ atoms of the tau fibrils are given in Figure 5.2(a). The angle of coverage as defined in our earlier work is shown in Figure 5.2(d). RMSF provides information about the mobility and flexibility of atoms or residues within a protein. High RMSF values indicate higher flexibility and greater deviation from the average position, suggesting dynamic regions or regions undergoing conformational changes. Conversely, low RMSF values suggest more rigid or less mobile regions. If the distribution of the C shape angle of coverage is narrow and centered around a specific value, it suggests that the tau fibril adopts a stable and well-defined C-shaped conformation. This indicates that the fibril structure is relatively rigid and maintains its characteristic shape throughout the simulation. If the distribution of the C shape angle is broad, it suggests that the tau fibril exhibits conformational flexibility. The PHF residues exhibit greater stability compared

to the SF structures. The difference between the RMSF values in the PC and PG with PI is greater in the SF structure compared to the PHF structure. Also, the residues are more flexible in the presence of the PC+PI lipids in the SF structure. This is due to the lower affinity of the tau fibril to bind with the bilayer in PC+PI systems, which is discussed in a later section.

The angle of coverage is defined by the residues as shown in Figure 5.2(b)-(c). The increase in the angle of coverage is correlated with the stability of the tau residues in case of the PHF fibril in PG+PI systems. The angle of coverage increases from $53°$ in the SF structure in PC+PI lipids to $59°$ in the PHF structure in PG+PI lipids. We infer that the increase in the angle of coverage is due to the higher affinity of the fibril to bind with PI infused lipid bilayer. Moreover, the increase of the angle of coverage correlates with the increase of fluctuations.

## 5.2.2 Bilayer Properties

### Area per lipids and Bilayer thickness

The bilayer thickness refers to the distance between the two leaflets of the lipid bilayer. It is typically measured as the distance between the phosphate groups of the two lipid layers. Bilayer thickness is affected by several factors, including the length and saturation of the lipid tails, the size and shape of the lipid headgroup, and the presence of cholesterol or other membrane proteins [230, 40]. The thickness of the bilayer can influence the diffusion of small molecules and the conformational dynamics of membrane proteins [231].

The area per lipid refers to the amount of area that each lipid occupies in the bilayer. It is typically measured as the total area of the lipid bilayer divided by the number of lipids in the bilayer. Area per lipid is influenced by the size and shape of the lipid headgroup and the length and saturation of the lipid tails. The area per lipid can affect the packing and fluidity of the membrane, which can impact the diffusion of small molecules and the

105
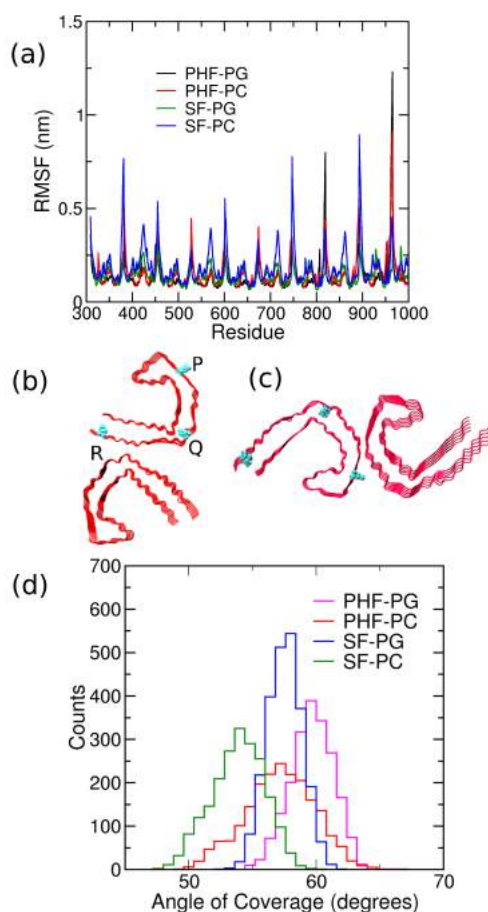
Figure 5.2: (a) RMSF of the C-$\alpha$ residues of the tau fibrils. (b)-(c) are the angle of coverage PQR used in the discussion. (d) The distribution of the angle of coverage in different systems. PHF/SF-PC/PG stands for the PHF or SF structures in POPC/POPG + PIP$_2$ bilayers.

activity of membrane proteins [232, 40, 233]. In general, changes in bilayer thickness and area per lipid can alter the physical properties of the lipid bilayer, which can have important biological consequences.

To elucidate the fibril lipid interactions, we have looked at the changes in the bilayer properties. The area per lipids (APL) and the bilayer thickness in the systems shed light on the effect of the fibrils on the bilayers. The bilayer thickness is calculated by taking the average distance between the phosphate groups on either leaflets. The APL for the systems along with the bilayer thickness are shown in Figure 5.3. The bilayer thickness and APL

describe the membrane deformations induced by the tau binding. The tau binding leads to membrane thinning and also leads to the decrease of APL compared to the control systems comprising of pure lipid bilayers.
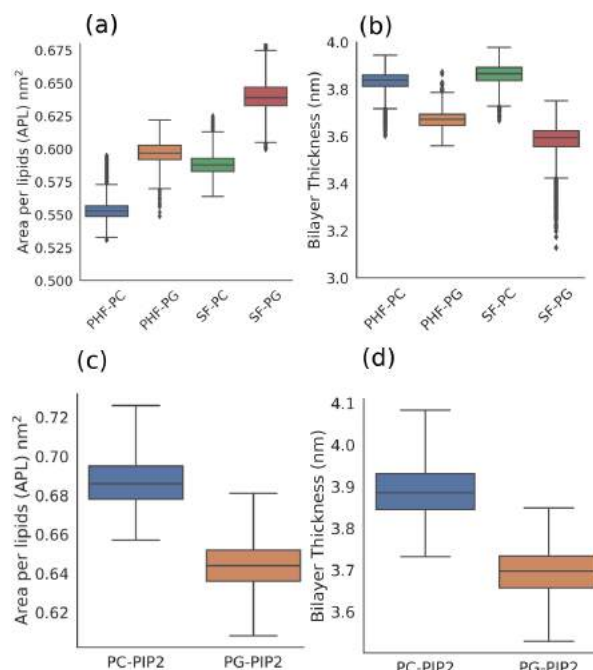


Figure 5.3: (a)-(b) are the box plots for the area per lipids and bilayer thickness averaged over the entire trajectory. The APL and bilayer thickness for the control systems without the tau fibrils are shown as box plots in (c) and (d), respectively.

The two-dimensional bilayer thickness in various bilayers and the control system without the tau fibril are shown in Figure 5.4. The thickness is projected over the bilayer plane and is shown as a colorbar. We find that the inclusion of tau fibrils induces local deformations in the membrane surface. The local thinning of the bilayer is most important to decipher the binding of tau fibrils. In case of the PHF structure in PC+PI lipid the bilayer thickness is high and is distributed throughout the bilayer. In comparison, the SF structure in PC+PI lipid shows two distinct islands of lower thickness seperated by higher thickness. The PHF strcuture in the PG+PI lipids show a comparatively thinner bilayer surface with respect to the PC+PI system, while in the case of SF structure in the PG+PI lipids there are

107
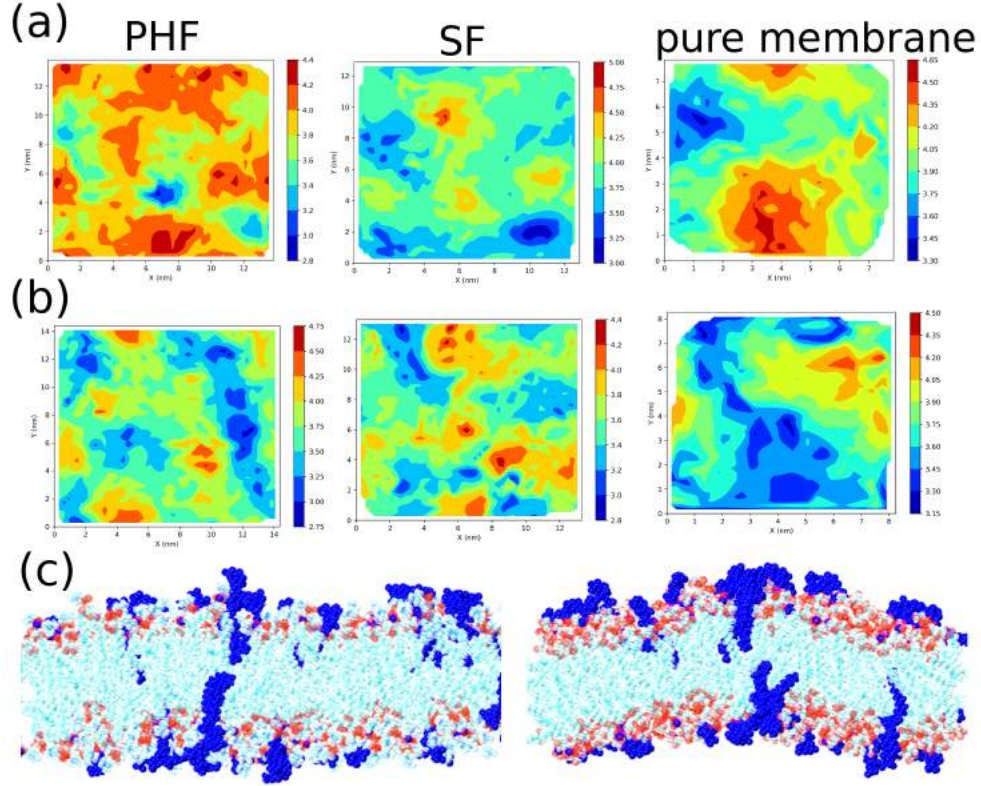
Figure 5.4: (a)-(b) are the bilayer thickness for the systems projected over the bilayer plane for the PC+PI and PG+PI systems respectively. The bilayer thickness (nm) is shown in a colorbar. (c) shows the snapshots of the tau incorporated PC+PI (left) and PG+PI (right) systems.

certain smaller regions of higher thickness in comparison to the SF structure in the PC+PI lipids. Overall we find that the PG+PI bilayer in presence of PHF structure show the largest decrease in the bilayer thickness in the tau-incorporated membrane.

**Order Parameter**

Order parameter ($S_{CH}$) of the lipid tails signify the time-averaged C–H bond angle, with respect to the bilayer normal. The Order Parameter of the acyl chains is defined as follows

$$S_{CH} = \left\langle \frac{3cos^2\theta - 1}{2} \right\rangle \tag{5.1}$$

Table 5.2: Mean value of the area per lipid ($nm^2$) and bilayer thickness (nm) of tau incorporated systems and control systems.

| | Area Per Lipid ($nm^2$) | Bilayer Thickness (nm) |
|---|---|---|
| Pure PI-PC | $0.644 \pm 0.01$ | $3.888 \pm 0.06$ |
| Pure PI-PG | $0.686 \pm 0.01$ | $3.695 \pm 0.05$ |
| PHF-PC | $0.554 \pm 0.009$ | $3.832 \pm 0.05$ |
| PHF-PG | $0.597 \pm 0.008$ | $3.671 \pm 0.03$ |
| SF-PC | $0.588 \pm 0.008$ | $3.862 \pm 0.04$ |
| SF-PG | $0.649 \pm 0.008$ | $3.527 \pm 0.02$ |

The $S_{CH}$ value of 1 corresponds to completely ordered acyl chains, and $S_{CH}$ value $\rightarrow 0$ signifies randomly oriented acyl chains. The $S_{CH}$ values of the sn-1 chains and the sn-2 chains in all the systems are shown in Figure 5.5 for PC and PG lipids. For both chains, the first seven carbon atoms show larger $S_{CH}$ values than atoms in the membrane core region, suggesting higher membrane fluidities near the lipid core. The highest values of the acyl chains are found for the pure PC-PI systems followed by SF-PC system. The least ordering of the acyl chains are found in the SF fibril with PG+PI lipids. Incorporation of PHF and SF tau fibrils decreases the lipid ordering as found from the earlier studies [34, 123]. Yet, there is only negligible change (approximately 2%) in the PC+PI systems in going from the pure membrane to the tau-infused membrane. On the other hand, there is a significant decrease in the order parameter in going from the pure PG+PI lipids to the fibril-infused lipid membrane with the highest decrease in the PHF structure (nearly 16%). Hence, we conclude that the PHF fibril perturbs the PG+PI more effectively compared to the SF fibril. Also, the negatively charged PG lipids are more affected by the tau fibrils compared to the PC lipids.

**Tilt Angle**

The tilt angle of the lipid molecules is important to decipher the lipid packing in the bilayer [234, 235]. The tilt angle is defined as the angle between the bilayer normal and the
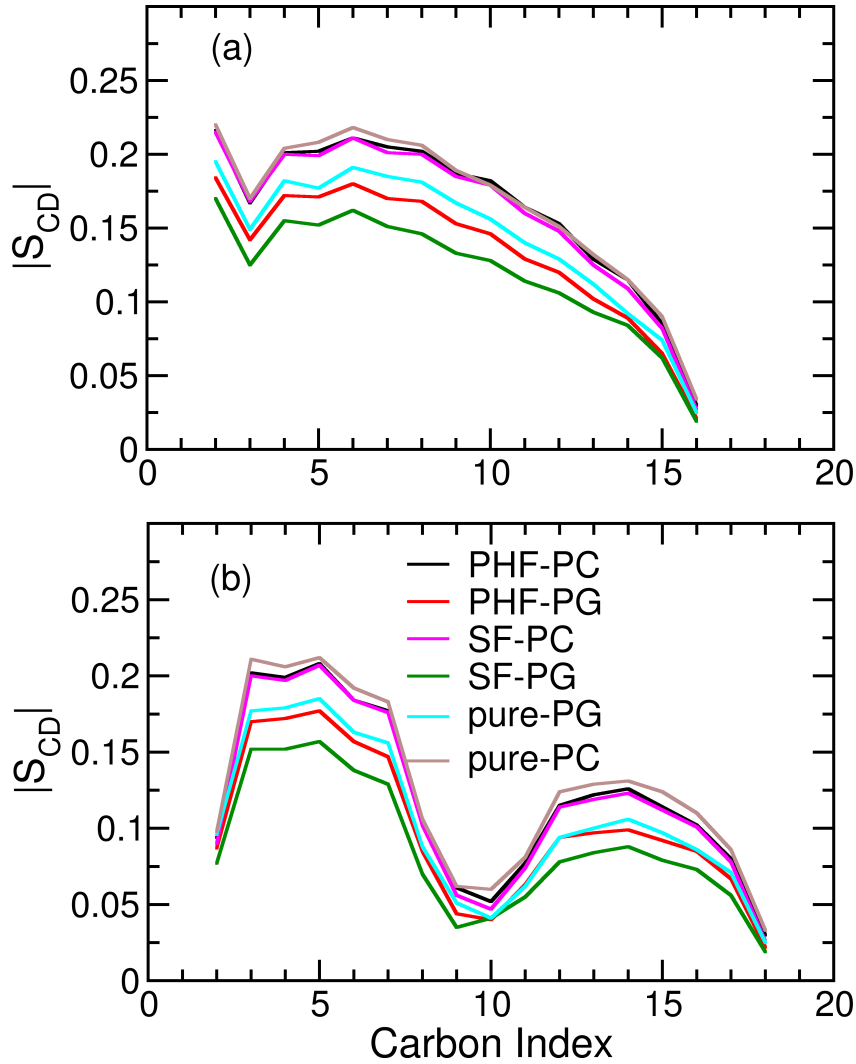
Figure 5.5: (a)-(b) are the order parameters of the lipid tails of PC/PG for the sn-1 and sn-2 chains of respectively.

individual vectors of P $\rightarrow$ C2 in PG lipid, P $\rightarrow$ C14 in PI lipid, and P $\rightarrow$ N in PC lipid [236]. If the tilt angle of the lipid is too large or too small, the membrane may become more rigid or more permeable [237, 238]. The tilt angle of the lipid molecules discerns the impact of the lipid packing and ordering of the bilayers. The earlier studies have found that the interdigitation, lipid order along with the lipid tilt angle is interrelated [239]. The increase in the lipid tilt angle leads to the decreasing lipid order due to the increase of the kink of the acyl chains. The phosphorylated inositol ring of the PI lipids are important to regulate the

110

Table 5.3: Tilt angle (°) for the lipid vectors for all the systems.

| System | PI | PC | PG |
|--------|-------|-------|-------|
| pure PI-PC | 59.78 | 88.28 | – |
| pure PI-PG | 48.09 | – | 40.61 |
| PHF-PC | 52.53 | 89.66 | – |
| PHF-PG | 51.63 | – | 37.74 |
| SF-PC | 23.96 | 91.5 | – |
| SF-PG | 52.12 | – | 40.58 |

specificity of the protein binding through electrostatic interactions [240]. It has also been observed that when the inositol rings move away from the membrane, the clustering of PI lipids is favoured [241]. The presence of the negatively charged PS lipids is also found to influence the inositol tilt angle in deciding the hydrogen bonding strength [225]. The mean tilt angle for all the systems is given in Table 5.3.

In general, the tilt angle of the PI molecules decrease in the presence of the both SF and PHF fibrils in the PI-PC system. On the other hand, the tilt angle increase in the presence of tau fibrils in the PI-PG system. The tilt angle can influence the accessibility and exposure of the PI headgroup, which in turn can affect protein binding specificity. Understanding the relationship between PI tilt angle and protein binding specificity can provide insights into the molecular mechanisms underlying protein-lipid interactions and the regulation of cellular processes involving PI signaling pathways [242].

**Membrane Roughness**

Membrane roughness is defined by the following equation [236]

$$R = \frac{1}{n} \sum_{i=1}^{n} |(z_i - z_m)| \tag{5.2}$$

where n is the total number of reference atoms, $z_i$ is the z-coordinate of reference atom i, and $z_m$ is the mean z-position of reference atoms. The values of the membrane roughness are given in Table 5.4. The membrane roughness is calculated through the average z-position

Table 5.4: Membrane Roughness (nm) of tau incorporated systems and control systems.

| System | Roughness (nm) |
|---|---|
| pure PI-PC | $0.863 \pm 0.01$ |
| pure PI-PG | $0.773 \pm 0.01$ |
| PHF-PC | $0.881 \pm 0.01$ |
| PHF-PG | $0.953 \pm 0.08$ |
| SF-PC | $0.872 \pm 0.01$ |
| SF-PG | $0.796 \pm 0.02$ |

of the lipid which describes the vertical fluctuations of the lipid molecules in the bilayers. For our results across all the systems, we have taken the PC or PG lipid as the reference in calculating the roughness. Membrane roughness can modulate the availability, accessibility, and organization of PI molecules, thereby impacting the binding affinity and localization of proteins that interact with PI lipids. Leonenko's group showed experimentally that the membrane roughness of the diseased membrane model in the presence of the A$\beta$ changes over time [243]. The higher membrane roughness correlated with increasing accumulation of A$\beta$ aggregates over the membrane. In our study, we found that the presence of tau fibrils in the system increase the membrane roughness compared to the pure PC+PI and PG+PI systems. Interaction with the PHF structure leads to the increase in the membrane roughness much more than the SF structure.

**Lipid Interdigitation**

The interdigitation of the membrane lipids is calculated through the degree of interdigitation between the acyl tails [244]. Lipid interdigitation is calculated from the corresponding width of the overlapping regions ($w_\rho$). Earlier studies have found that membrane binding with the proteins leads to the thinning of the membrane which in turn leads to the mass overlap of the acyl chains in the opposing leaflets [245, 239]. The values of the interdigitation metrics for all the systems are given in Table 5.5.

We find that the decrease in the bilayer thickness correlates with the increasing inter-

112

Table 5.5: The interdigitation metrics for all the systems.

| System | $w_\rho$ (nm) |
|---|---|
| pure PI-PC | $0.51 \pm 0.03$ |
| pure PI-PG | $0.58 \pm 0.02$ |
| PHF-PC | $0.59 \pm 0.03$ |
| PHF-PG | $0.78 \pm 0.08$ |
| SF-PC | $0.60 \pm 0.05$ |
| SF-PG | $0.88 \pm 0.05$ |

digitation with the interaction of the tau fibrils. The interdigitation is more prominent in PG+PI in presence of SF fibrils. The interdigitation of the pure PG+PI lipids increases by nearly 0.20 nm with the inclusion of the PHF, whereas it increases by 0.30 nm in presence of SF fibril. The change in interdigitation values of the acyl chains is minimal in the PC+PI lipids upon inclusion of tau polymorphs. Thus, we conclude that lipid interdigitation and bilayer thinning occur simultaneously with the inclusion of tau polymorphs, and the change in interdigitation is most prominent in the SF system comprising PG+PI lipids.

### 5.2.3   Tau bilayer interaction

**Number of Contacts**

To model longer timescales of the tau-membrane interaction, we calculated the total number of contacts between the membrane and the tau structures from the coarse grained simulations. The cutoff for the contacts is chosen to be 0.7 nm. The total number of contacts between the membrane and the tau structure is shown in Figure 5.6. The change in the number of contacts is marginal in both the PC+PI and PG+PI systems. PHF in PC+PI bilayer shows a lower number of contacts compared to the PG+PI. On the other hand, the changes in the number of contacts in SF with PC+PI and PG+PI are minimal which is nearly 1%. Hence, it is observed that the PHF structure shows the most stable binding with PG+PI bilayer.

The clustering of the PI lipids is a necessary phenomenon responsible for cell signalling that is critical for cell health [246, 247, 248, 249]. The clustering is mediated by the influence of cations like $Ca^{2+}$, which is also observed in physiological conditions [250]. Based on the coarse grained simulations studies of our earlier report [34], we have compared the number of tau − lipid contacts in the SF fibril in the pure PG bilayer with that in the PG-PI bilayer. The presence of PI lipids in the bilayer increases the number of contacts between the tau fibril and the bilyaer in both the bilayers formed of PC and PG lipids. Thus, we can infer from the coarse grained simulations that PI lipids facilitate the tau fibril binding over the bilayer. The inclusion of the PI lipids show a more consistent tau interaction between the zwitterionic PC in comparison to the anionic PG lipids. We also observe clustering of the PI lipids in the bilayer during the course of the simulations, which is shown in Figure 5.6(b)-(c). The number of PI lipids found in the clustering is shown in Figure 5.6(d). We predict a possible correlation between the clustering of the PI lipids and the increasing number of contacts between the tau fibril and the PI containing bilayers.
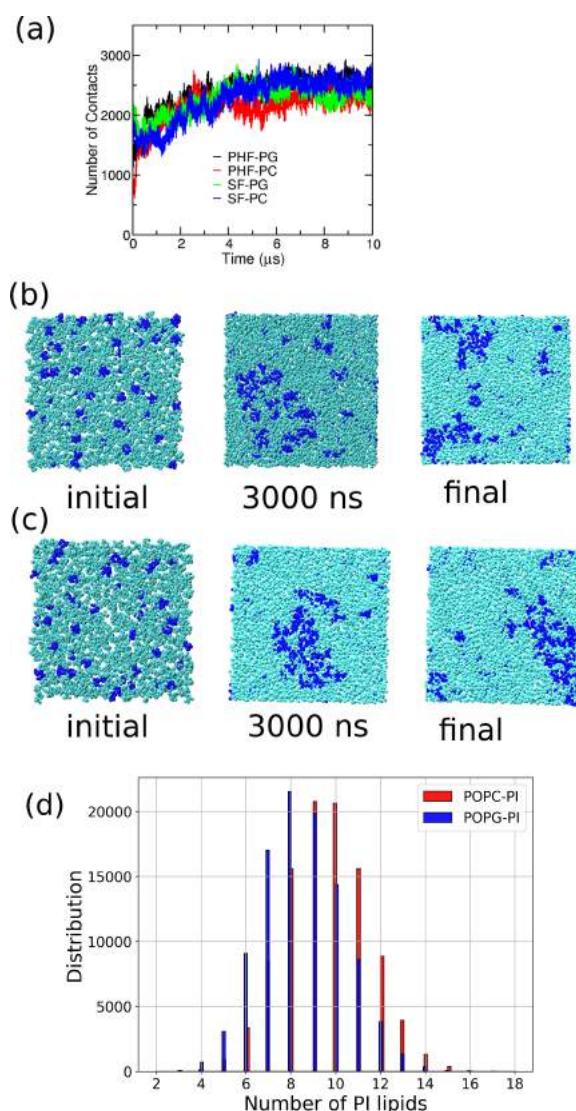
Figure 5.6: (a) The number of contacts between the tau fibrils and the bilayer from the coarse-grained simulations. (b)-(c) are the snaphots of the bilayer at various timesteps from the coarse grained simulations in PC and PG systems, respectively. The PI headgroups are shown as blue VDW spheres, the PC/PG beads are shown in cyan. (d) The histograms of the number of PI lipids forming clusters which is obtained from the coarse grained simulations in PHF system.

**Per Residue Contacts**

To analyse the fibril–lipid contacts, we have calculated the per residue contacts of the tau polymorphs. The per residue contacts for the SF and PHF structures are shown in Figure 5.7.

115

The contacts are calculated taking a cutoff value of 1.0 nm from tau residue to the lipid taken from the all atom simulations. This will help us understanding which specific amino acid residues of the tau fibrils come close to the lipid molecules providing valuable insights into the molecular interactions that may be relevant for understanding the tau mediated pathogenesis.

The PHF structures show more number of contacts with both the POPC and $PIP_2$ lipids in comparison to the SF structures. In the case of the PHF structures, N-terminal region shows a higher number of contacts with the $PIP_2$ lipids, especially between the I308 and K317 residues. The higher number of $PIP_2$ lipid contacts leads to the concomitant decrease of the POPC contacts. The POPC contacts are highest in K321 residue. Similarly, for the PHF with POPG+$PIP_2$ lipids, the peaks for POPG lipids are seen at K317, K321 residues and I371 for the $PIP_2$ lipids. The least number of contacts are seen for the SF structure with POPC+$PIP_2$ lipids with the peaks at 327–328 residues for the $PIP_2$ and POPC lipids respectively.

**Tau dimer interface**

The tau R3–R4 structure is stabilized by certain key residues in the interface. The polymorphism arises from the difference in the dimer interface though the core residues of the R3–R4 fragment are the same. The important amino acid interactions stabilizing the dimer interface are shown in Figure 5.8. In the PHF interface, the important interactions are salt-bridge contacts between K331–E338 and the interaction between G334 residues in the adjacent chains. In the SF structure, the dimer interaction is between L315–K321 and K317–K321 residues.

In the PHF structure, the G334–G334 distance is 0.599 nm in the cryo-EM structure which decreases in all the systems. The average distance between the G334–G334 residues in PG+PI and PC+PI is nearly 0.440 nm. The salt bridge distance between the $NH_3^+$ and
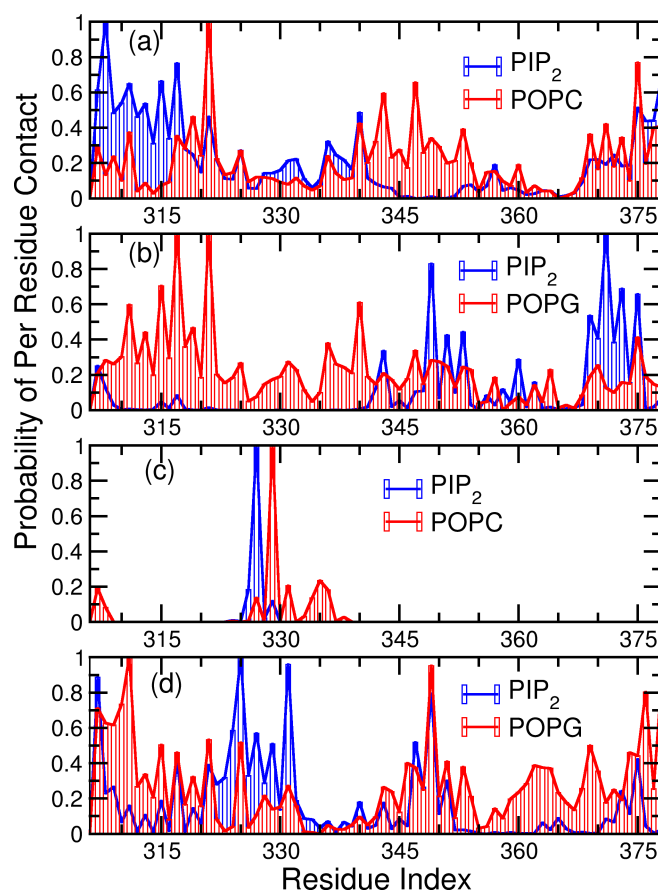
Figure 5.7: (a)-(b) are the per residue contacts for the PHF structure and (c)-(d) are the per residue contacts of the SF structure for the individual lipid components.

$COO^-$ groups in the cryo-EM structure is 0.693 nm and in the water medium it is 0.371 nm. Hence the G334–G334 and salt bridge distance decreases in both the water medium and the PI infused lipids.

In the SF structure, L315–K321 residues have a distance of 0.935 nm in the cryo-EM structure and 0.783 nm in the water medium. This distance changes to 0.839 nm and 0.729 nm in the PC+PI and PG+PI systems. The distance between the K317–K321 residues changes to 1.316 nm and 1.119 nm in the PC+PI and PG+PI lipids respectively. The K317–K321 distance in the water medium is 1.260 nm and the corresponding distance in the cryo EM structure is 1.213 nm. Thus, the cryo EM distances for the interface residues changes
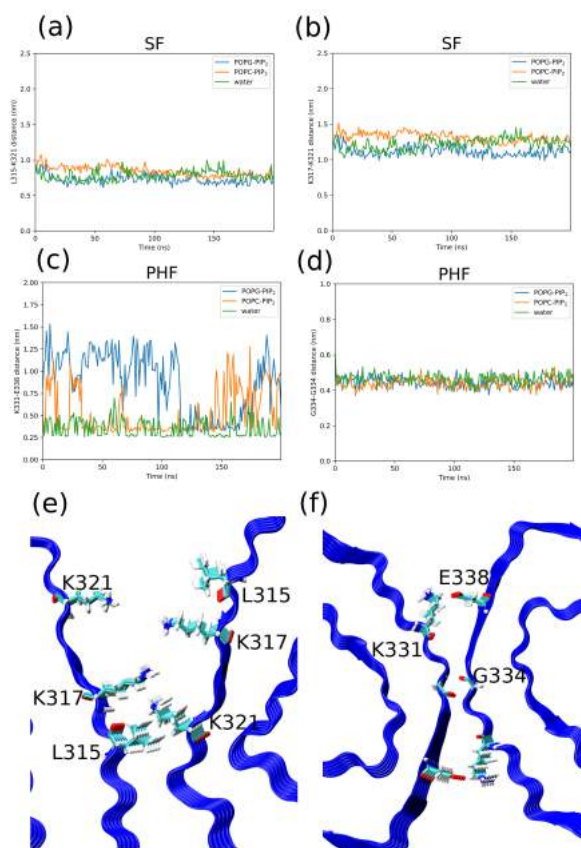
Figure 5.8: (a)-(b) are the L315–K321 distance and K317–K321 distance for SF structures. (c)-(d) are the K331–E338 distance and G334–G334 distance for PHF structures. (e)-(f) are the snapshots for the tau fibril interface showing the key residues.

in both the water medium and in the PI infused membranes. We predict the tighter packing of the tau dimers in the PI infused bilayers in the timescales of our simulations.

**Secondary structure content**

The secondary structure content of the tau polymorphs shed light on the changes in the secondary structure upon binding with the PI-infused lipids. The earlier studies have shown that the composition of the lipid bilayers have an effect on the secondary structure content of the tau fibrils and the interaction of the tau fibrils with the lipid bilayers lead to the concomitant loss of the $\beta$-sheet structures [34, 185]. The cryo-EM structure of the tau R3–

118

R4 fragments span the residues V306–K311 in $\beta$1, V313–C322 in $\beta$2, N327–K331 in $\beta$3, Q336–S341 in $\beta$4, K343–K347 in $\beta$5, R349–I357 in $\beta$6, S356–V363 in $\beta$7 and N368–F378 in $\beta$8. The per residue propensity of the tau residues is shown in Figure 5.9(a)-(b). The total number of the $\beta$-sheet residues is shown in a violin plot in Figure 5.9(c).

The secondary structure content of the tau fibrils varies considerably in the presence of the PI-infused bilayers. The PHF structures show only a marginal change in the per-residue propensity in going from PC+PI to PG+PI. The C-terminals show considerable change in the proportion of the $\beta$-strand and the coil conformation in the SF structures in the PC and PG-infused PI lipids. Also, the $\beta$6 region between R349–I357 and $\beta$7 region between S356–V363 show most notable changes. In the PI-PC lipids the $\beta$3 region and the C-terminal region show most difference in the $\beta$-sheet content. In terms of the total number of $\beta$-sheet residues, we find that the negatively charged PG+PI lipids preserve most of the $\beta$-sheet region in the SF structure. The least number of $\beta$-sheet residues is found in the PHF structure with the PC+PI lipids. In comparison with the tau-PI systems, the total number of beta-sheet residues in the water medium is 379$\pm$22 for the PHF fibrils and 401$\pm$21 in the case of SF structures. Hence we conclude that the interaction of the negatively charged PG with PI lipids preserves the most number of $\beta$ sheet residues in tau. The interaction of the tau fibrils with the lipid bilayers lead to the change in number of $\beta$-sheet residues.

**Bilayer Fibril Depth**

To characterize the binding of the tau fibrils over the membrane bilayers, we have computed the $z$-coordinate center of the mass distance between the tau fibrils and the bilayer. The $z$-coordinate represents the vertical axis perpendicular to the surface of the bilayer, and it is used to describe the position of molecules along this axis. This describes how far the tau fibrils are from the lipid bilayer, providing valuable information about the interaction between them. This bilayer fibril approach depth is shown in Figure 5.10(a). The final
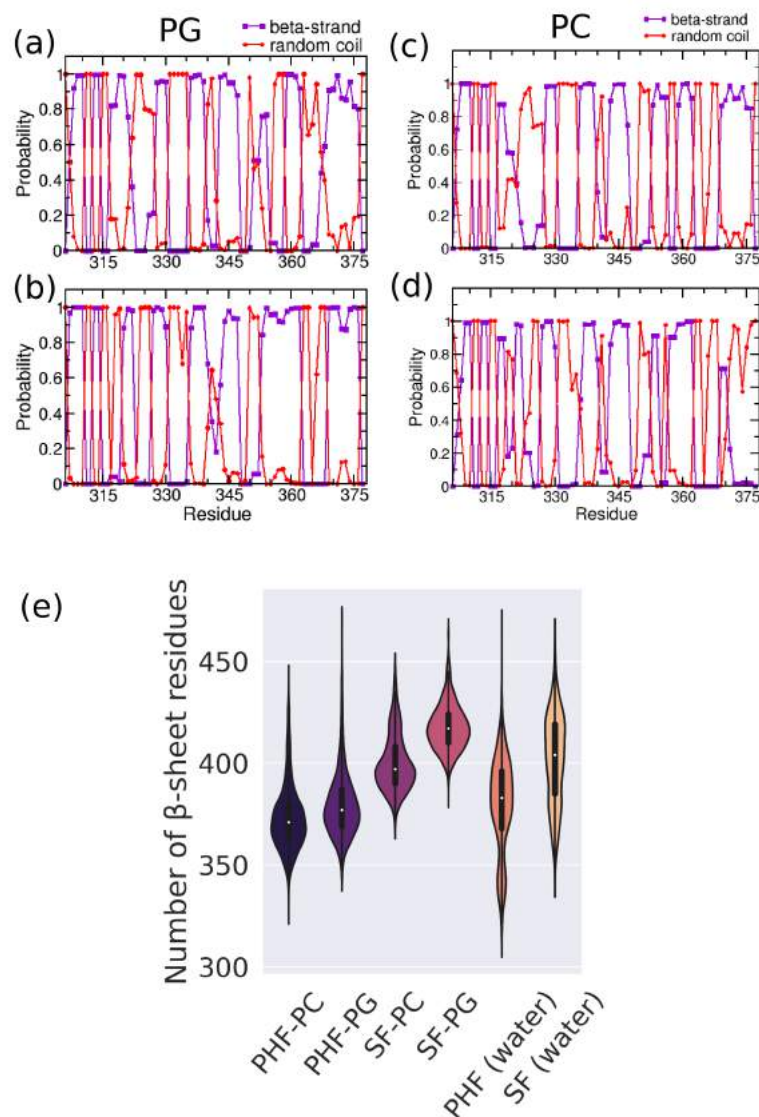
Figure 5.9: (a)-(b) are the per residue propensities in tau polymorphs PHF and SF structures respectively in the PI infused PG lipids, and (c)-(d) are the per residue propensities in the PI infused PC lipids (e) is the violin plot of the total number of $\beta$-sheet residues in the four systems. PHF/SF – PC/PG stands for the PHF or SF structures in PC/PG+PI bilayers.

snapshots of all the systems are shown in Figure 5.10(b)-(e). The tau fibrils approach PI-infused PG lipids closer compared to the PC-infused PI lipids. The depth is less for the SF–PG system with respect to the PHF–PG system. On the contrary, the SF is farthest from the center of mass of the bilayer in PC systems among all the systems. Thus, tau fibrils in the presence of the PG-PI lipids show the most effective binding over the membrane. To further corroborate this fact, the final snapshots are also included in Figure 5.10. As found in the case of the SF–PC system, the final snapshot shows the fibril moving away from the bilayer.

**Binding specificity of PI lipids with the tau fibrils**

The PI lipids cluster spontaneously in the lipid membrane which is responsible for cell signalling and calcium influx in the cell [249]. The calcium ions bridge between the negatively charged phosphate groups in the PI lipids and facilitate the aggregation [247]. It is known that the tau binding on the lipid membranes are mediated by the positively charged residues of the tau surface and the negatively charged lipid headgroups, hence we looked into the possible docking mechanism of the tau fibril over the PI domains on the bilayer [132, 226]. Figure 5.11 shows the snapshots of the interaction of tau filament (PHF) with PI lipids at different timeframes. Arg 349 and Lys 353 residues are shown along with a neighbouring PI lipid. The PI lipid is bound to the Arg 349 residue initially upto 55 ns. Once the PI lipid is unbound, it binds to the neighboring Lys 353. This binding of Lys 353 with the PI lipid has a longer residence time and it lasts nearly 160 ns. The distance between the -NH$_3^+$ of Arg/Lys and the -PO$_4^{3-}$ of PI lipid is also included in Figure 5.11(e).

We prostulate that the PI binding is mediated by the negatively charged PG lipids, the presence of which makes the positively charged tau residues move closer to the PI headgroups. On the contrary, the initial interaction of the tau residues with the PC lipids are less as the PC is zwitterionic. The positively charged residues of the tau are hence far away
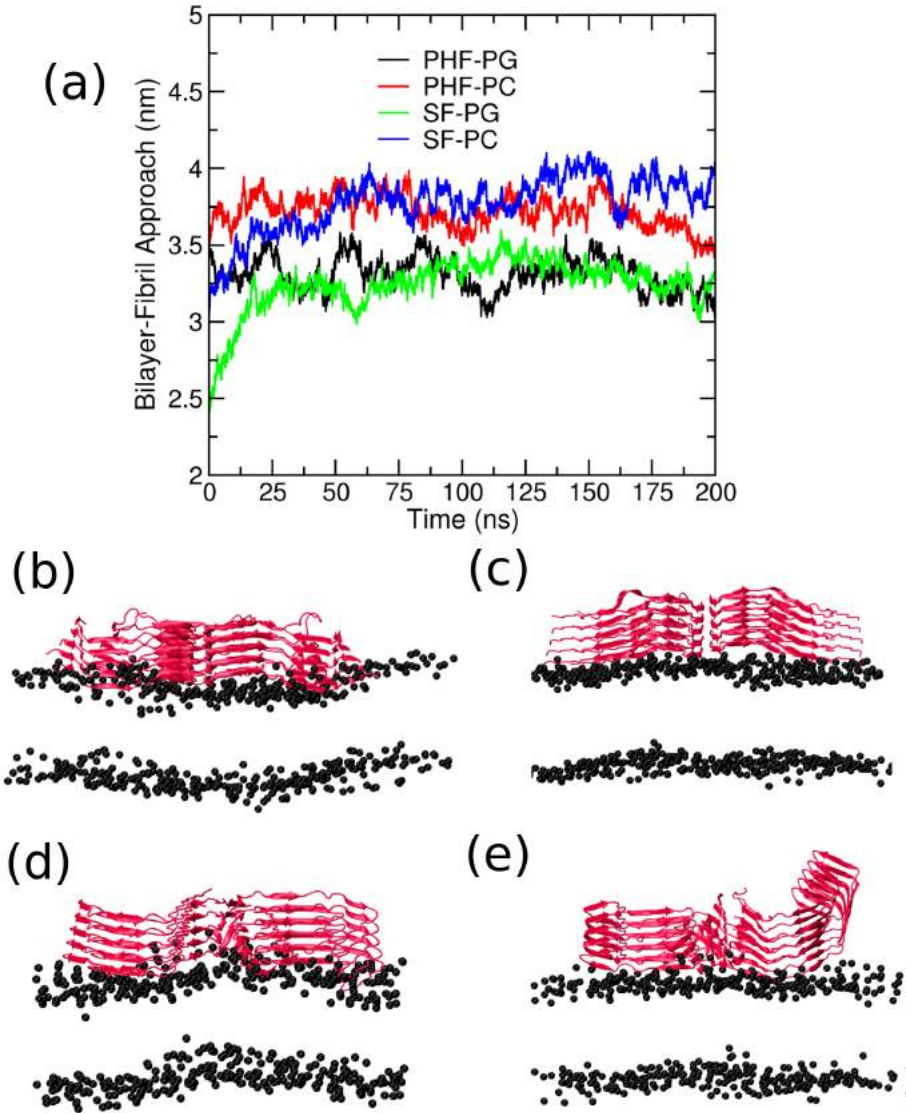
Figure 5.10: (a) The bilayer approach depth of the fibril and the bilayer along the z-direction. (b)-(c) are the final snapshots for the PHF-PG and PHF-PC systems and (d)-(e) are the final snapshots of the SF-PG and SF-PC systems.

from the negatively charged phosphate groups of PI lipids which causes reduced affinity of tau binding in PC-PI lipids.

Corbin et al. proposed a two-step search process based on their investigation of the GRP1 PH domain and PI lipid [251, 225]. Initially, the PH domain engages in transient

and weak electrostatic interactions with the anionic lipids (PS/PI) in the background. This interaction enhances the protein's residency time on the membrane surface and enables a two-dimensional search for PI. Once PI is located, the PH domain binds to it specifically and with a high affinity. The first step involves proteins being attracted to the membrane surface by anionic lipids (PS and PI) through nonspecific electrostatic interactions. This interaction reduces the search dimension from three to two, facilitating efficient protein diffusion without tight binding. In the second step, proteins may encounter their target PIs in a distinct region during two dimensional diffusion, where the PI are bound to adjacent anionic lipids (PS and PI) through hydrogen bonding. Alternatively, proteins can locate target PI through orientational changes when the PI are bonded to the PS/PI in the same region. Finally, proteins bind to PIPs through specific interactions with the phosphate groups of the inositol ring or through stronger nonspecific electrostatic interactions with basic residues in the protein.

## 5.3 Conclusion

The interaction of tau with the cellular membrane appears to be an important factor in the development of tau-related pathologies, and further research is needed to fully understand the mechanisms underlying this interaction and its contribution to disease. MD simulation studies of the tau polymorphs (PHF and SF) in presence of the model membrane composed of PC/PG and PI lipids in the ratio of 9:1 have been carried out to probe the interaction of phosphatidylinositol (PI) with tau fibrils. PHF structures are found to be more stable than the SF in the PI infused POPC and POPG PI lipids. The tau binding over the PI containing bilayer causes membrane deformation which is evident from the order parameter, tilt angle and membrane roughness. Though simulations done in the timescales described cannot capture all modes of interaction and adsorption of tau over the membrane, our studies
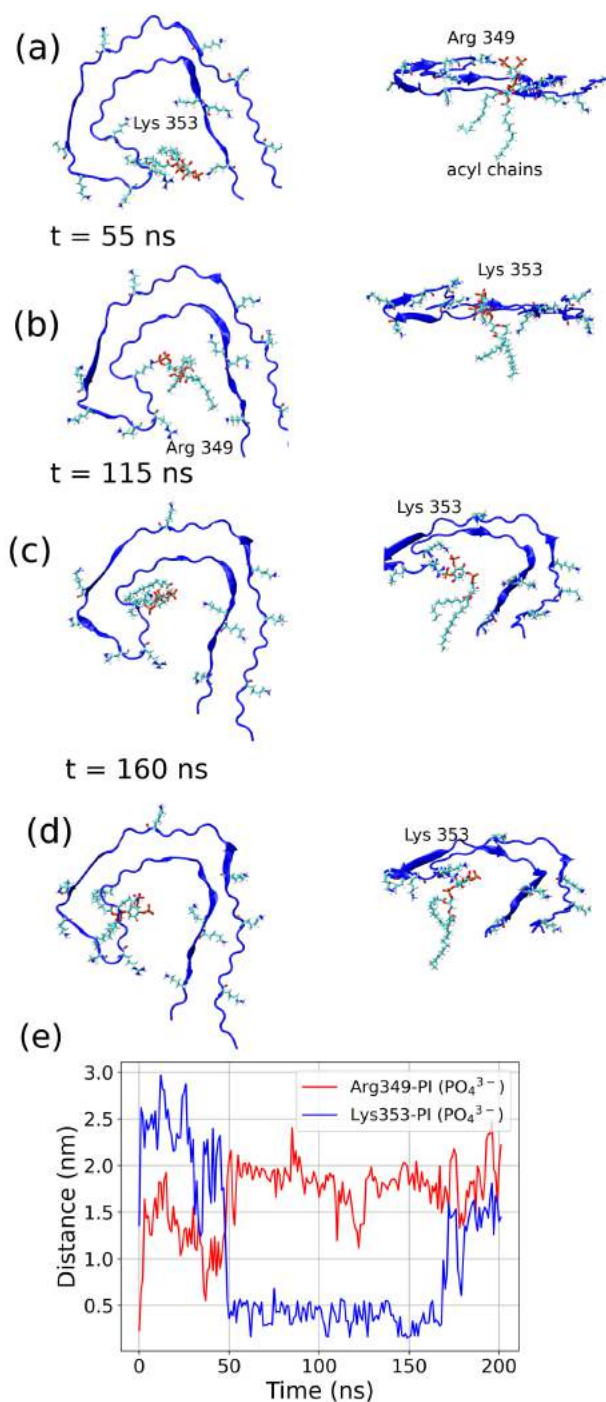
Figure 5.11: The snapshots of tau filament (PHF) interacting with the PI lipids at four different timeframes. Only the first chain of the tau fibril interacting with the lipid is shown for clarity. The positively charged residues (Arg, Lys, His) and the interacting PI lipid are shown in licorice representation. The second column is the snapshot viewed from the xz plane.

124

provide insights into the interaction of PI with tau fibrils in bilayers composed of POPC and POPG infused with PI lipids. Multiple starting configurations with different orientations of the tau are required to capture other modes of interaction. Also, metadynamics and umbrella sampling can be done taking suitable collective variable. But, even with the inclusion of most powerful computational hardwares and optimized MD codes, 300,000 atoms still can be computationally demanding for the MD simulations carried out here in the current report.

# Chapter 6

# Conclusion

Neurodegenerative diseases have a significant impact on global health, affecting millions of people worldwide. These diseases pose a substantial burden on individuals, families, and healthcare systems due to their chronic and progressive nature. These are a group of disorders characterized by the progressive degeneration and dysfunction of neurons (nerve cells) in the central nervous system. These diseases primarily affect the structure and function of the brain and spinal cord, leading to a gradual decline in cognitive function and overall neurological health. The important cause of neurological disorders (like Alzheimer's Disease and several other tauopathies) are correlated with the aggregation of the amyloid beta and tau in the extracellular membrane and neurofibrillary tangles intracellularly. Even with the advent of modern biophysical techniques and imaging techniques the progression of Alzheimer's and its correlation with the decline of cognition is poorly understood. We aim to investigate the structural and biophysical characteristics of these aggregating proteins that lead to neurological disorders. Though most of the research has been guided towards the amyloid $\beta$ protein and its aggregation, tau proteins are less studied and still not understood properly. With the rise of cryo-electron microscopy and sophisticated structure refinement protocols along with NMR, the neurodegenerative protein ensembles are characterized in a better way.

The helix $\rightarrow$ coil transition is an important collective variable used earlier to characterize the folding of the $\alpha$-helix rich small peptides. We find that the helix $\rightarrow$ coil transition of the amyloid $\beta$ monomer is affected by the inclusion of Zn$^{2+}$ ion with the monomer. The Zn$^{2+}$ ion is found to stabilize the regions with $\alpha$-helix residues.

Since the importance of the cell membrane mediated tau toxicity is poorly understood, we modeled the interaction of the tau fibrils (derived from the cryo-EM) through the all-atom and coarse-grained simulations. Lipid composition is found to affect the conformational ensemble of the tau fibrils. Molecular dynamics simulations show that tau proteins interact differentially with the zwitterionic compared to the charged lipid membranes. The negatively charged POPG lipid membranes increase the binding propensity of the tau fibrils. The addition of cholesterol is also found to modify the tau binding to the membrane. The binding of tau fibril leads to the concomitant loss of the β-sheet structures across the tau residues alongside the change in the membrane properties (like area per lipid, bilayer thickness, and order parameter of the lipid tails) over the pure bilayers.

Molecular mechanisms underlying the tau interaction with the neuronal membrane are hitherto unknown and difficult to characterize using experimental methods. Using the structure of the tau-fibrils we have used atomistic molecular dynamics simulation to model the tau fibril and neuronal membrane interaction using explicit solvation. The dynamics and structural characteristics of the tau fibril with the neuronal membrane are compared to the tau fibril in the aqueous phase to corroborate the effect of the neuronal membrane in the tau structure. Tau fibrils have been modelled using CHARMM-36m force field and a six component neuronal membrane composition is taken. The timescale conceivable in our molecular dynamics simulations is of the order of microseconds which captures the onset of the interaction of the tau fibrils with the neuronal membrane. This interaction is found to impact the tau pathogenesis that finally causes neuronal toxicity. Our study initiates the understanding of tau conformational ensemble in the presence of neuronal membrane and sheds light on the significant tau- neuronal membrane interactions.

Phosphatidylinositol (PI) lipids act as important members for the domain formation in the cell membranes. We also have studied the influence of the PI lipids on the structure and conformation of tau proteins. Tau proteins have emerged as important candidates in caus-

127

ing a number of tauopathies including Alzheimer's Disease. We have carried out molecular dynamics simulations (both coarse-grained and all-atom) using PI lipid incorporated lipid patches having POPC and POPG to study the conformational changes of the R3–R4 section of the tau fibrils. We observe varying degree of perturbation by the tau polymorphs in the lipid membrane, which is studied through various lipid membrane properties (like membrane roughness, acyl chain order parameter, tilt angle, etc). We also elucidate the docking sites of the PI lipids on the tau fibrils mediated by the electrostatic interactions between the negatively charged PI lipid headgroups and the positively charged tau residues in the tau surface. The negatively charged POPG along with PI lipids synergistically facilitates this binding of tau on the PI infused lipid membranes.

# References

[1] José Nelson Onuchic and Peter G Wolynes. Theory of protein folding. *Curr. Opin. Struct. Biol.*, 14(1):70–75, 2004.

[2] David L Nelson, Albert L Lehninger, and Michael M Cox. *Lehninger Principles of Biochemistry*. Macmillan, 2008.

[3] Claudio Soto and Sandra Pritzkow. Protein misfolding, aggregation, and conformational strains in neurodegenerative diseases. *Nat. Neurosci.*, 21(10):1332–1340, 2018.

[4] Christopher A Ross and Michelle A Poirier. Protein aggregation and neurodegenerative disease. *Nat. Med.*, 10(Suppl 7):S10–S17, 2004.

[5] Fred E Cohen and Jeffery W Kelly. Therapeutic approaches to protein-misfolding diseases. *Nature*, 426(6968):905–909, 2003.

[6] Xinxin Zuo, Jie Zhou, Yinming Li, Kai Wu, Zonggui Chen, Zhiwei Luo, Xiaorong Zhang, Yi Liang, Miguel A Esteban, Yu Zhou, et al. Tdp-43 aggregation induced by oxidative stress causes global mitochondrial imbalance in als. *Nature structural & molecular biology*, 28(2):132–142, 2021.

[7] Claudio Soto. Protein misfolding and disease; protein refolding and therapy. *FEBS Lett.*, 498(2-3):204–207, 2001.

[8] Jens Tyedmers, Axel Mogk, and Bernd Bukau. Cellular strategies for controlling protein aggregation. *Nat. Rev. Mol. Cell Biol.*, 11(11):777–788, 2010.

[9] Lary C Walker, Marc I Diamond, Karen E Duff, and Bradley T Hyman. Mechanisms of protein seeding in neurodegenerative diseases. *JAMA Neurol.*, 70(3):304–310, 2013.

[10] Christian Münch and Anne Bertolotti. Propagation of the prion phenomenon: Beyond the seeding principle. *J. Mol. Biol.*, 421(4-5):491–498, 2012.

[11] Gill Livingston, Jonathan Huntley, Andrew Sommerlad, David Ames, Clive Ballard, Sube Banerjee, Carol Brayne, Alistair Burns, Jiska Cohen-Mansfield, Claudia Cooper, et al. Dementia prevention, intervention, and care: 2020 report of the lancet commission. *The Lancet*, 396(10248):413–446, 2020.

[12] Cora O'Neill, Brian Anderton, Jean-Pierre Brion, Brian H Anderton, Michéle Authelet, Rejith Dayanandan, Karelle Leroy, Simon Lovestone, Jean-Noël Octave, Laurent Pradier, et al. Neurofibrillary tangles and tau phosphorylation. In *Biochem. Soc. Symp.*, volume 67, pages 81–88. Portland Press, 2001.

[13] Fong Ping Chong, Khuen Yen Ng, Rhun Yian Koh, and Soi Moi Chye. Tau proteins and tauopathies in alzheimer's disease. *Cell. Mol. Neurobiol.*, 38:965–980, 2018.

[14] Suman Nag, Bidyut Sarkar, Arkarup Bandyopadhyay, Bankanidhi Sahoo, Varun KA Sreenivasan, Mamata Kombrabail, Chandrakesan Muralidharan, and Sudipta Maiti. Nature of the amyloid-$\beta$ monomer and the monomer-oligomer equilibrium. *J. Biol. Chem.*, 286(16):13827–13833, 2011.

[15] Ewa Sitkiewicz, Marcin Kłoniecki, Jarosław Poznański, Wojciech Bal, and Michał Dadlez. Factors influencing compact–extended structure equilibrium in oligomers of a$\beta$1–40 peptide - an ion mobility mass spectrometry study. *J. Biol. Chem.*, 426(15):2871–2885, 2014.

[16] Gal Bitan, Sabrina S Vollers, and David B Teplow. Elucidation of primary structure elements controlling early amyloid $\beta$-protein oligomerization. *J. Biol. Chem.*, 278(37):34882–34889, 2003.

[17] Massimo Innocenti, Emanuele Salvietti, Martina Guidotti, Angela Casini, Silvano Bellandi, Maria Luisa Foresti, Chiara Gabbiani, Andrea Pozzi, Paolo Zatta, and Luigi Messori. Trace copper (ii) or zinc (ii) ions drastically modify the aggregation behavior of amyloid-$\beta$ 1–42: An afm study. *J. Alzheimer's Dis.*, 19(4):1323–1329, 2010.

[18] Michael Gold. Phase ii clinical trials of anti–amyloid $\beta$ antibodies: When is enough, enough? *Alzheimer's Dement.: Transl. Res. Clin.*, 3(3):402–409, 2017.

[19] Sjors HW Scheres, Wenjuan Zhang, Benjamin Falcon, and Michel Goedert. Cryo-em structures of tau filaments. *Curr. Opin. Struct. Biol.*, 64:17–25, 2020.

[20] John Berriman, Louise C Serpell, Keith A Oberg, Anthony L Fink, Michel Goedert, and R Anthony Crowther. Tau filaments from human brain and from in vitro assembly of recombinant protein show cross-$\beta$ structure. *Proc. Natl. Acad. Sci. U.S.A.*, 100(15):9034–9038, 2003.

[21] Michel Goedert, David S Eisenberg, and R Anthony Crowther. Propagation of tau aggregates and neurodegeneration. *Annu. Rev. Neurosci.*, 40:189–210, 2017.

[22] Ian W Hamley. The amyloid beta peptide: a chemist's perspective. role in alzheimer's and fibrillization. *Chem. Rev.*, 112(10):5147–5192, 2012.

[23] Jessica Nasica-Labouze, Phuong H Nguyen, Fabio Sterpone, Olivia Berthoumieu, Nicolae-Viorel Buchete, Sebastien Cote, Alfonso De Simone, Andrew J Doig, Peter Faller, Angel Garcia, et al. Amyloid $\beta$ protein and alzheimer's disease: When computer simulations complement experimental studies. *Chem. Rev.*, 115(9):3518–3563, 2015.

[24] Paolo Calabresi, Alessandro Mechelli, Giuseppina Natale, Laura Volpicelli-Daley, Giulia Di Lazzaro, and Veronica Ghiglieri. Alpha-synuclein in parkinson's disease and other synucleinopathies: from overt neurodegeneration back to early synaptic dysfunction. *Cell death & disease*, 14(3):176, 2023.

[25] Joost Schulte and J Troy Littleton. The biological function of the huntingtin protein and its relevance to huntington's disease pathology. *Curr. Trends Neurol.*, 5:65, 2011.

[26] Gillian P Bates. The molecular genetics of huntington disease—a history. *Nat. Rev. Genet.*, 6(10):766–773, 2005.

[27] Sonja Blumenstock and Irina Dudanova. Cortical and striatal circuits in huntington's disease. *Front. Neurosci.*, 14:82, 2020.

[28] Matthew C Kiernan, Steve Vucic, Benjamin C Cheah, Martin R Turner, Andrew Eisen, Orla Hardiman, James R Burrell, and Margaret C Zoing. Amyotrophic lateral sclerosis. *The Lancet*, 377(9769):942–955, 2011.

[29] Jing L Guo and Virginia MY Lee. Cell-to-cell transmission of pathogenic proteins in neurodegenerative diseases. *Nat. Med.*, 20(2):130–138, 2014.

[30] David J Irwin, Virginia M-Y Lee, and John Q Trojanowski. Parkinson's disease dementia: convergence of $\alpha$-synuclein, tau and amyloid-$\beta$ pathologies. *Nat. Rev. Neurosci.*, 14(9):626–636, 2013.

[31] Miranda Robbins, Emma Clayton, and Gabriele S Kaminski Schierle. Synaptic tau: A pathological or physiological phenomenon? *Acta Neuropathol. Commun.*, 9(1):1–30, 2021.

[32] Hebah Fatafta, Chetan Poojari, Abdallah Sayyed-Ahmad, Birgit Strodel, and Michael C Owen. Role of oxidized gly25, gly29, and gly33 residues on the interactions of a$\beta$1–42 with lipid membranes. *ACS Chem. Neurosci.*, 11(4):535–548, 2020.

[33] Hebah Fatafta, Mohammed Khaled, Michael C Owen, Abdallah Sayyed-Ahmad, and Birgit Strodel. Amyloid-$\beta$ peptide dimers undergo a random coil to $\beta$-sheet transition in the aqueous phase but not at the neuronal membrane. *Proc. Natl. Acad. Sci. U.S.A.*, 118(39):e2106210118, 2021.

131

[34] Unmesh Dutta Chowdhury, Arnav Paul, and B. L. Bhargava. The effect of lipid composition on the dynamics of tau fibrils. *Proteins*, 90(12):2103–2115, 2022.

[35] Yoshiyuki Soeda and Akihiko Takashima. New insights into drug discovery targeting tau protein. *Front. Mol. Neurosci.*, 13:590896, 2020.

[36] Christopher Kolloff and Simon Olsson. Machine learning in molecular dynamics simulations of biomolecular systems. *arXiv preprint arXiv:2205.03135*, 2022.

[37] Shreyas Kaptan and Ilpo Vattulainen. Machine learning in the analysis of biomolecular simulations. *Adv. Phys.: X.*, 7(1):2006080, 2022.

[38] RO Calderon, B Attema, and GH DeVries. Lipid composition of neuronal cell bodies and neurites from cultured dorsal root ganglia. *J. Neurochem*, 64(1):424–429, 1995.

[39] Ganesh Shahane, Wei Ding, Michail Palaiokostas, and Mario Orsi. Physical properties of model biological lipid bilayers: insights from all-atom molecular dynamics simulations. *J. Mol. Model.*, 25:1–13, 2019.

[40] Olga Press-Sandler and Yifat Miller. Molecular insights into the primary nucleation of polymorphic amyloid $\beta$ dimers in dopc lipid bilayer membrane. *Protein Science*, 31(5):e4283, 2022.

[41] Lisha Wang, Rajnish Kumar, Pavel F Pavlov, Bengt Winblad, et al. Small molecule therapeutics for tauopathy in alzheimer's disease: Walking on the path of most resistance. *Eur. J. Med. Chem.*, 209:112915, 2021.

[42] Daan Frenkel and Berend Smit. *Understanding molecular simulation: from algorithms to applications*, volume 1. Elsevier, 2001.

[43] Peter Virnau and Marcus Müller. Calculation of free energy through successive umbrella sampling. *J. Chem. Phys.*, 120(23):10925–10930, 2004.

[44] Giovanni Bussi and Alessandro Laio. Using metadynamics to explore complex free-energy landscapes. *Nat. Rev. Phys.*, 2(4):200–212, 2020.

[45] Michael R Shirts, David L Mobley, and John D Chodera. Alchemical free energy calculations: ready for prime time? *Annu. Rep. Comput. Chem.*, 3:41–59, 2007.

[46] Sanghyun Park and Klaus Schulten. Calculating potentials of mean force from steered molecular dynamics simulations. *J. Chem. Phys.*, 120(13):5946–5961, 2004.

[47] Berk Hess, Carsten Kutzner, David Van Der Spoel, and Erik Lindahl. Gromacs 4: Algorithms for highly efficient, load-balanced, and scalable molecular simulation. *J. Chem. Theory Comput.*, 4(3):435–447, 2008.

[48] James C Phillips, Rosemary Braun, Wei Wang, James Gumbart, Emad Tajkhorshid, Elizabeth Villa, Christophe Chipot, Robert D Skeel, Laxmikant Kale, and Klaus Schulten. Scalable molecular dynamics with namd. *J. Comput. Chem.*, 26(16):1781–1802, 2005.

[49] Romelia Salomon-Ferrer, David A Case, and Ross C Walker. An overview of the amber biomolecular simulation package. *Wiley Interdisciplinary Reviews: Computational Molecular Science*, 3(2):198–210, 2013.

[50] Bernard R Brooks, Charles L Brooks III, Alexander D Mackerell Jr, Lennart Nilsson, Robert J Petrella, Benoît Roux, Youngdo Won, Georgios Archontis, Christian Bartels, Stefan Boresch, et al. Charmm: the biomolecular simulation program. *J. Comput. Chem.*, 30(10):1545–1614, 2009.

[51] Paulo CT Souza, Riccardo Alessandri, Jonathan Barnoud, Sebastian Thallmair, Ignacio Faustino, Fabian Grünewald, Ilias Patmanidis, Haleh Abdizadeh, Bart MH Bruininks, Tsjerk A Wassenaar, et al. Martini 3: a general purpose force field for coarse-grained molecular dynamics. *Nat. Methods*, 18(4):382–388, 2021.

[52] Peter J Bond, John Holyoake, Anthony Ivetac, Syma Khalid, and Mark SP Sansom. Coarse-grained molecular dynamics simulations of membrane proteins and peptides. *J. Struct. Biol.*, 157(3):593–605, 2007.

[53] Tobias Hartmann, Sophie C Bieger, Babara Brühl, Pentti J Tienari, Nobuo Ida, David Allsop, Gareth W Roberts, Colin L Masters, Carlos G Dotti, and Klaus Unsicker. Distinct sites of intracellular production for alzheimer's disease a$\beta$40/42 amyloid peptides. *Nat. Med.*, 3(9):1016, 1997.

[54] Rakez Kayed, Elizabeth Head, Jennifer L Thompson, Theresa M McIntire, Saskia C Milton, Carl W Cotman, and Charles G Glabe. Common structure of soluble amyloid oligomers implies common mechanism of pathogenesis. *Science*, 300(5618):486–489, 2003.

[55] Dennis J Selkoe and John Hardy. The amyloid hypothesis of alzheimer's disease at 25 years. *EMBO Mol. Med.*, 8(6):595–608, 2016.

[56] Stephen S. Dominy, Casey Lynch, Florian Ermini, Malgorzata Benedyk, Agata Marczyk, Andrei Konradi, Mai Nguyen, Ursula Haditsch, Debasish Raha, Christina Griffin, Leslie J. Holsinger, Shirin Arastu-Kapur, Samer Kaba, Alexander Lee, Mark I. Ryder, Barbara Potempa, Piotr Mydel, Annelie Hellvard, Karina Adamowicz, Hatice Hasturk, Glenn D. Walker, Eric C. Reynolds, Richard L. M. Faull, Maurice A. Curtis, Mike Dragunow, and Jan Potempa. Porphyromonas gingivalis in alzheimer's disease brains: Evidence for disease causation and treatment with small-molecule inhibitors. *Sci. Adv.*, 5(1), 2019.

[57] Justin A Lemkul and David R Bevan. Assessing the stability of alzheimer's amyloid protofibrils using molecular dynamics. *J. Phys. Chem. B*, 114(4):1652–1660, 2010.

[58] "A.Keith Dunker, J.David Lawson, Celeste J Brown, Ryan M Williams, Pedro Romero, Jeong S Oh, Christopher J Oldfield, Andrew M Campen, Catherine M Ratliff, Kerry W Hipps, Juan Ausio, Mark S Nissen, Raymond Reeves, ChulHee Kang, Charles R Kissinger, Robert W Bailey, Michael D Griswold, Wah Chiu, Ethan C Garner, and Zoran Obradovic. Intrinsically disordered protein. *J. Mol. Graph. Model.*, 19(1):26–59, 2001.

[59] MA Lovell, JD Robertson, WJ Teesdale, JL Campbell, and WR Markesbery. Copper, iron and zinc in alzheimer's disease senile plaques. *J. Neurol. Sci.*, 158(1):47–52, 1998.

[60] Lisa M Miller, Qi Wang, Tejas P Telivala, Randy J Smith, Antonio Lanzirotti, and Judit Miklossy. Synchrotron-based infrared and x-ray imaging shows focalized accumulation of cu and co-localized with $\beta$-amyloid deposits in alzheimer's disease. *J. Struct. Biol.*, 155(1):30–37, 2006.

[61] Kevin J Barnham and Ashley I Bush. Biological metals and metal-targeting compounds in major neurodegenerative diseases. *Chem. Soc. Rev.*, 43(19):6727–6749, 2014.

[62] Bruno Alies, Amandine Conte-Daban, Stephanie Sayen, Fabrice Collin, Isabelle Kieffer, Emmanuel Guillon, Peter Faller, and Christelle Hureau. Zinc (ii) binding site to the amyloid-$\beta$ peptide: Insights from spectroscopic studies with a wide series of modified peptides. *Inorg. Chem.*, 55(20):10499–10509, 2016.

[63] Jens Danielsson, Roberta Pierattelli, Lucia Banci, and Astrid Gräslund. High-resolution nmr studies of the zinc-binding site of the alzheimer's amyloid $\beta$-peptide. *FEBS J.*, 274(1):46–59, 2007.

[64] Sergey A Kozin, Séverine Zirah, Sylvie Rebuffat, Gaston Hui Bon Hoa, and Pascale Debey. Zinc binding to alzheimer's a$\beta$(1–16) peptide results in stable soluble complex. *Biochem. Bioph. Res. Co.*, 285(4):959–964, 2001.

[65] Séverine Zirah, Sergey A Kozin, Alexey K Mazur, Alain Blond, Michel Cheminant, Isabelle Ségalas-Milazzo, Pascale Debey, and Sylvie Rebuffat. Structural changes of region 1-16 of the alzheimer disease amyloid $\beta$-peptide upon zinc binding and in vitro aging. *J. Biol. Chem.*, 281(4):2151–2161, 2006.

[66] Liang Xu, Xiaojuan Wang, and Xicheng Wang. Effects of zn$^{2+}$ binding on the structural and dynamic properties of amyloid $\beta$ peptide associated with alzheimer's disease: Asp1 or glu11? *ACS Chem. Neurosci.*, 4(11):1458–1468, 2013.

[67] Yifat Miller, Buyong Ma, and Ruth Nussinov. Zinc ions promote alzheimer a$\beta$ aggregation via population shift of polymorphic states. *Proc. Natl. Acad. Sci. U.S.A.*, 107(21):9490–9495, 2010.

[68] Wenfei Li, Jian Zhang, Yu Su, Jun Wang, Meng Qin, and Wei Wang. Effects of zinc binding on the conformational distribution of the amyloid-$\beta$ peptide based on molecular dynamics simulations. *J. Phys. Chem. B*, 111(49):13814–13821, 2007.

[69] Mohsen Asadbegi and Amir Shamloo. Evaluating the multifunctionality of a new modulator of zinc-induced a$\beta$ aggregation using a novel computational approach. *J. Chem. Inf. Model.*, 61(3):1383–1401, 2021.

[70] Saikat Pal and Sandip Paul. Atp controls the aggregation of a$\beta_{16-22}$ peptides. *J. Phys. Chem. B*, 124(1):210–223, 2019.

[71] Sathish Dasari and Bhabani S Mallik. Ion-induced free energy landscapes of a$\beta_{33-42}$ peptide dimer in wet ionic liquids. *J. Mol. Liq.*, 318:114026, 2020.

[72] Theodor Ackbarow, Xuefeng Chen, Sinan Keten, and Markus J. Buehler. Hierarchies, multiple energy barriers, and robustness govern the fracture mechanics of $\alpha$-helical and $\beta$-sheet protein domains. *Proc. Natl. Acad. Sci. U.S.A.*, 104(42):16410–16415, 2007.

[73] Elizabeth P. DeBenedictis and Sinan Keten. Mechanical unfolding of alpha- and beta-helical protein motifs. *Soft Matter*, 15:1243–1252, 2019.

[74] Sunhwan Jo, Taehoon Kim, Vidyashankara G. Iyer, and Wonpil Im. Charmm-gui: A web-based graphical user interface for charmm. *J. Comput. Chem.*, 29(11):1859–1865, 2008.

[75] B. R. Brooks, C. L. Brooks III, A. D. Mackerell Jr., L. Nilsson, R. J. Petrella, B. Roux, Y. Won, G. Archontis, C. Bartels, S. Boresch, A. Caflisch, L. Caves, Q. Cui, A. R. Dinner, M. Feig, S. Fischer, J. Gao, M. Hodoscek, W. Im, K. Kuczera, T. Lazaridis, J. Ma, V. Ovchinnikov, E. Paci, R. W. Pastor, C. B. Post, J. Z. Pu, M. Schaefer, B. Tidor, R. M. Venable, H. L. Woodcock, X. Wu, W. Yang, D. M. York, and M. Karplus. Charmm: The biomolecular simulation program. *J. Comput. Chem.*, 30(10):1545–1614, 2009.

[76] Jumin Lee, Xi Cheng, Jason M. Swails, Min Sun Yeom, Peter K. Eastman, Justin A. , Shuai Wei, Joshua Buckner, Jong Cheol Jeong, Yifei Qi, Sunhwan Jo, Vijay S. Pande, David A. Case, Charles L. Brooks, Alexander D. MacKerell, Jeffery B. Klauda, and Wonpil Im. Charmm-gui input generator for namd, gromacs, amber, openmm, and charmm/openmm simulations using the charmm36 additive force field. *J. Chem. Theory Comput.*, 12(1):405–413, 2016.

[77] Jing Huang, Sarah Rauscher, Grzegorz Nawrocki, Ting Ran, Michael Feig, Bert L de Groot, Helmut Grubmüller, and Alexander D MacKerell. Charmm36m: An improved force field for folded and intrinsically disordered proteins. *Nat. Methods.*, 14(1):71–73, 2017.

[78] Berk Hess, Henk Bekker, Herman J. C. Berendsen, and Johannes G. E. M. Fraaije. Lincs: A linear constraint solver for molecular simulations. *J. Comput. Chem.*, 18(12):1463–1472, 1997.

[79] Tom Darden, Darrin York, and Lee Pedersen. Particle mesh ewald: An n·log (n) method for ewald sums in large systems. *J. Chem. Phys.*, 98(12):10089–10092, 1993.

[80] Denis J Evans and Brad Lee Holian. The nose–hoover thermostat. *J. Chem. Phys.*, 83(8):4069–4074, 1985.

[81] Michele Parrinello and Aneesur Rahman. Polymorphic transitions in single crystals: A new molecular dynamics method. *J. Appl. Phys.*, 52(12):7182–7190, 1981.

[82] Carsten Kutzner, David Van Der Spoel, Martin Fechner, Erik Lindahl, Udo W Schmitt, Bert L De Groot, and Helmut Grubmüller. Speeding up parallel gromacs on high-latency networks. *J. Comput. Chem.*, 28(12):2075–2084, 2007.

[83] William Humphrey, Andrew Dalke, and Klaus Schulten. Vmd: Visual molecular dynamics. *J. Molec. Graphics*, 14(1):33–38, 1996.

[84] Jochen S Hub, Bert L De Groot, and David Van Der Spoel. g_wham–a free weighted histogram analysis implementation including robust error and autocorrelation estimates. *J. Chem. Theory Comput.*, 6(12):3713–3720, 2010.

[85] Hu Shi, Baotao Kang, and Jin Yong Lee. $Zn^{2+}$ effect on structure and residual hydrophobicity of amyloid $\beta$-peptide monomers. *J. Phys. Chem. B*, 118(35):10355–10361, 2014.

[86] Masha G Savelieff, Sanghyun Lee, Yuzhong Liu, and Mi Hee Lim. Untangling amyloid-$\beta$, tau, and metals in alzheimer's disease. *ACS Chem. Biol.*, 8(5):856–865, 2013.

[87] Edmund I Lin and M Scott Shell. Can peptide folding simulations provide predictive information for aggregation propensity? *J. Phys. Chem. B*, 114(36):11899–11908, 2010.

[88] Mabel A. Cejas, William A. Kinney, Cailin Chen, Jeremy G. Vinter, Harold R. Almond, Karin M. Balss, Cynthia A. Maryanoff, Ute Schmidt, Michael Breslav, Andrew Mahan, Eilyn Lacy, and Bruce E. Maryanoff. Thrombogenic collagen-mimetic peptides: Self-assembly of triple helix-based fibrils driven by hydrophobic interactions. *Proc. Natl. Acad. Sci. U.S.A.*, 105(25):8513–8518, 2008.

[89] Yan Mu and Meng Yu. Effects of hydrophobic interaction strength on the self-assembled structures of model peptides. *Soft matter*, 10(27):4956–4965, 2014.

[90] Gautam R Desiraju and Thomas Steiner. *The Weak Hydrogen Bond: in Structural Chemistry and Biology*, volume 9. International Union of Crystal, 2001.

[91] Prabir Khatua, Souvik Mondal, and Sanjoy Bandyopadhyay. Effects of metal ions on $a\beta_{42}$ peptide conformations from molecular simulation studies. *J. Chem. Inf. Model.*, 59(6):2879–2893, 2019.

[92] Pham Dinh Quoc Huy, Quan Van Vuong, Giovanni La Penna, Peter Faller, and Mai Suan Li. Impact of cu (ii) binding on structures and dynamics of $a\beta_{42}$ monomer and dimer: Molecular dynamics study. *ACS Chem. Neurosci.*, 7(10):1348–1363, 2016.

[93] Searle S Duay, Gaurav Sharma, Rajeev Prabhakar, Alfredo M Angeles-Boza, and Eric R May. Molecular dynamics investigation into the effect of zinc (ii) on the structure and membrane interactions of the antimicrobial peptide clavanin a. *J. Phys. Chem. B*, 123(15):3163–3176, 2019.

[94] John J Balbach, Yoshitaka Ishii, Oleg N Antzutkin, Richard D Leapman, Nancy W Rizzo, Fred Dyda, Jennifer Reed, and Robert Tycko. Amyloid fibril formation by $a\beta_{16-22}$, a seven-residue fragment of the alzheimer's $\beta$-amyloid peptide, and structural characterization by solid state nmr. *Biochemistry*, 39(45):13748–13759, 2000.

[95] Colin J Barrow, Akikazu Yasuda, Peter TM Kenny, and Michael G Zagorski. Solution conformations and aggregational properties of synthetic amyloid $\beta$-peptides of alzheimer's disease: Analysis of circular dichroism spectra. *J. Mol. Biol.*, 225(4):1075–1093, 1992.

[96] Caroline Hilbich, Brigitte Kisters-Woike, Jennifer Reed, Colin L Masters, and Konrad Beyreuther. Aggregation and secondary structure of synthetic amyloid $\beta$a4 peptides of alzheimer's disease. *J. Mol. Biol.*, 218(1):149–163, 1991.

[97] Alberto Marin-Gonzalez, JG Vilhena, Ruben Perez, and Fernando Moreno-Herrero. Understanding the mechanical response of double-stranded dna and rna under constant stretching forces using all-atom molecular dynamics. *Proc. Natl. Acad. Sci. U.S.A.*, 114(27):7049–7054, 2017.

[98] Michel A Cuendet and Olivier Michielin. Protein-protein interaction investigated by steered molecular dynamics: the tcr-pmhc complex. *Biophys. J.*, 95(8):3575–3590, 2008.

[99] Martin Zacharias. Minor groove deformability of dna: a molecular dynamics free energy simulation study. *Biophys. J.*, 91(3):882–891, 2006.

[100] Gungor Ozer, Stephen Quirk, and Rigoberto Hernandez. Thermodynamics of decaalanine stretching in water obtained by adaptive steered molecular dynamics simulations. *J. Chem. Theory Comput.*, 8(11):4837–4844, 2012.

[101] Yeng-Tseng Wang, Zhi-Yuan Su, and Cheng-Lung Chen. Potential of mean force of the hepatitis c virus core protein–monoclonal 19d9d6 antibody interaction. *Biophys. Chem.*, 145(2-3):86–90, 2009.

[102] Yuxin Zhang, Hujun Shen, Mingbo Zhang, and Guohui Li. Exploring the proton conductance and drug resistance of bm2 channel through molecular dynamics simulations and free energy calculations at different ph conditions. *J. Phys. Chem. B*, 117(4):982–988, 2013.

[103] Po-Chia Chen and Serdar Kuyucak. Accurate determination of the binding free energy for kcsa-charybdotoxin complex from the potential of mean force calculations with restraints. *Biophys. J.*, 100(10):2466–2474, 2011.

[104] Gael Benay and Georges Wipff. Liquid–liquid extraction of alkali cations by 18-crown-6: Complexation and interface crossing studied by md and pmf simulations. *New J. Chem.*, 40(3):2102–2114, 2016.

[105] C. Jarzynski. Equilibrium free-energy differences from nonequilibrium measurements: A master-equation approach. *Phys. Rev. E*, 56:5018–5035, Nov 1997.

[106] C. Jarzynski. Nonequilibrium equality for free energy differences. *Phys. Rev. Lett.*, 78:2690–2693, Apr 1997.

[107] Shankar Kumar, John M. Rosenberg, Djamal Bouzida, Robert H. Swendsen, and Peter A. Kollman. The weighted histogram analysis method for free-energy calculations on biomolecules. i. the method. *J. Comput. Chem.*, 13(8):1011–1021, 1992.

[108] Hailey R Bureau, Dale R Merz Jr, Eli Hershkovits, Stephen Quirk, and Rigoberto Hernandez. Constrained unfolding of a helical peptide: Implicit versus explicit solvents. *PloS one*, 10(5), 2015.

[109] Robert Wieczorek and JJ Dannenberg. H-bonding cooperativity and energetics of $\alpha$-helix formation of five 17-amino acid peptides. *J. Am. Chem. Soc.*, 125(27):8124–8129, 2003.

[110] Alexandre V Morozov, Kiril Tsemekhman, and David Baker. Electron density redistribution accounts for half the cooperativity of $\alpha$ helix formation. *J. Phys. Chem. B*, 110(10):4503–4505, 2006.

[111] Jingwen Li, Yefei Wang, Jingfei Chen, Zhijun Liu, Ad Bax, and Lishan Yao. Observation of $\alpha$-helical hydrogen-bond cooperativity in an intact protein. *J. Am. Chem. Soc.*, 138(6):1824–1827, 2016.

[112] Allam S Reddy, Lu Wang, Sadanand Singh, Yun L Ling, Lauren Buchanan, Martin T Zanni, James L Skinner, and Juan J De Pablo. Stable and metastable states of human amylin in solution. *Biophys. J.*, 99(7):2208–2216, 2010.

[113] Allam S Reddy, Lu Wang, Yu-Shan Lin, Yun Ling, Manan Chopra, Martin T Zanni, James L Skinner, and Juan J De Pablo. Solution structures of rat amylin peptide: Simulation, theory, and experiment. *Biophys. J.*, 98(3):443–451, 2010.

[114] Thomas Arendt, Jens T Stieler, and Max Holzer. Tau and tauopathies. *Brain Res. Bull.*, 126:238–292, 2016.

[115] Jian-Zhi Wang, Yi-Yuan Xia, Inge Grundke-Iqbal, and Khalid Iqbal. Abnormal hyperphosphorylation of tau: Sites, regulation, and molecular mechanism of neurofibrillary degeneration. *J. Alzheimer's Dis.*, 33(s1):S123–S139, 2013.

[116] W Noble, DP Hanger, CC Miller, and S Lovestone. The importance of tau phosphorylation for neurodegenerative diseases. *Front Neurol.*, 2013.

[117] Erin E Congdon and Einar M Sigurdsson. Tau-targeting therapies for alzheimer disease. *Nat. Rev. Neurol.*, 14(7):399–415, 2018.

[118] Anthony WP Fitzpatrick, Benjamin Falcon, Shaoda He, Alexey G Murzin, Garib Murshudov, Holly J Garringer, R Anthony Crowther, Bernardino Ghetti, Michel Goedert, and Sjors HW Scheres. Cryo-em structures of tau filaments from alzheimer's disease. *Nature*, 547(7662):185–190, 2017.

[119] Holger Wille, Gerard Drewes, Jacek Biernat, Eva-Maria Mandelkow, and Eckhard Mandelkow. Alzheimer-like paired helical filaments and antiparallel dimers formed from microtubule-associated protein tau in vitro. *J. Cell. Biol.*, 118(3):573–584, 1992.

[120] Cass Leonard, Christian Phillips, and James McCarty. Insight into seeded tau fibril growth from molecular dynamics simulation of the alzheimer's disease protofibril core. *Front. Mol. Biosci.*, 8:109, 2021.

[121] Roland Brandt, Jocelyne Léger, and Gloria Lee. Interaction of tau with the neural plasma membrane mediated by tau's amino-terminal projection domain. *J. Cell Biol.*, 131(5):1327–1340, 1995.

[122] Shana Elbaum-Garfinkle, Trudy Ramlall, and Elizabeth Rhoades. The role of the lipid bilayer in tau aggregation. *Biophys. J.*, 98(11):2722–2730, 2010.

[123] Emmalee M Jones, Manish Dubey, Phillip J Camp, Briana C Vernon, Jacek Biernat, Eckhard Mandelkow, Jaroslaw Majewski, and Eva Y Chi. Interaction of tau protein with model lipid membranes induces tau structural compaction and membrane disruption. *Biochemistry*, 51(12):2539–2550, 2012.

[124] Victoria Campos-Peña, José Tapia-Ramírez, Carmen Sánchez-Torres, and Marco Antonio Meraz-Rios. Pathological-like assembly of tau induced by a paired helical filament core expressed at the plasma membrane. *J. Alzheimer's Dis.*, 18(4):919–933, 2009.

[125] Stefania A Mari, Susanne Wegmann, Katharina Tepper, Bradley T Hyman, Eva-Maria Mandelkow, Eckhard Mandelkow, and Daniel J Müller. Reversible cation-selective attachment and self-assembly of human tau on supported brain lipid membranes. *Nano Lett.*, 18(5):3271–3281, 2018.

[126] Mehdi Azouz, Cécile Feuillie, Michel Lafleur, Michaël Molinari, and Sophie Lecomte. Interaction of tau construct k18 with model lipid membranes. *Nanoscale Adv.*, 3(14):4244–4253, 2021.

[127] Qiong-Qiong Yao, Jitao Wen, Sarah Perrett, and Si Wu. Distinct lipid membrane-mediated pathways of tau assembly revealed by single-molecule analysis. *Nanoscale*, 2022.

[128] Elka R Georgieva, Shifeng Xiao, Peter P Borbat, Jack H Freed, and David Eliezer. Tau binds to lipid membrane surfaces via short amphipathic helices located in its microtubule-binding repeats. *Biophys. J.*, 107(6):1441–1452, 2014.

[129] Patrick Barré and David Eliezer. Folding of the repeat domain of tau upon binding to lipid surfaces. *J. Mol. Biol.*, 362(2):312–326, 2006.

[130] Jitao Wen, Liu Hong, Georg Krainer, Qiong-Qiong Yao, Tuomas PJ Knowles, Si Wu, and Sarah Perrett. Conformational expansion of tau in condensates promotes irreversible aggregation. *J. Am. Chem. Soc.*, 143(33):13056–13064, 2021.

[131] Botond Penke, Mária Szűcs, and Ferenc Bogár. Oligomerization and conformational change turn monomeric $\beta$-amyloid and tau proteins toxic: Their role in alzheimer's pathogenesis. *Molecules*, 25(7):1659, 2020.

[132] Adeline M Fanni, Crystal M Vander Zanden, Paulina V Majewska, Jaroslaw Majewski, and Eva Y Chi. Membrane-mediated fibrillation and toxicity of the tau hexapeptide phf6. *J. Biol. Chem.*, 294(42):15304–15317, 2019.

[133] Macarena Marin and Thomas Ott. Intrinsic disorder in plant proteins and phytopathogenic bacterial effectors. *Chem. Rev.*, 114(13):6912–6932, 2014.

140

[134] H Jane Dyson and Peter E Wright. Perspective: the essential role of nmr in the discovery and characterization of intrinsically disordered proteins. *J. Biol. NMR*, 73(12):651–659, 2019.

[135] Tiago N Cordeiro, Fatima Herranz-Trillo, Annika Urbanek, Alejandro Estaña, Juan Cortés, Nathalie Sibille, and Pau Bernadó. Small-angle scattering studies of intrinsically disordered proteins and their complexes. *Curr. Opin. Struct. Biol.*, 42:15–23, 2017.

[136] Benjamin Schuler, Andrea Soranno, Hagen Hofmann, and Daniel Nettels. Single-molecule fret spectroscopy and the polymer physics of unfolded and intrinsically disordered proteins. *Annu. Rev. Biophys.*, 45:207–231, 2016.

[137] Joshua A Riback, Micayla A Bowman, Adam M Zmyslowski, Catherine R Knoverek, John M Jumper, James R Hinshaw, Emily B Kaye, Karl F Freed, Patricia L Clark, and Tobin R Sosnick. Innovative scattering analysis shows that hydrophobic disordered proteins are expanded in water. *Science*, 358(6360):238–241, 2017.

[138] Christopher M Baker and Robert B Best. Insights into the binding of intrinsically disordered proteins from molecular dynamics simulation. *Wiley Interdisp. Rev.*, 4(3):182–198, 2014.

[139] Stefano Piana, Alexander G Donchev, Paul Robustelli, and David E Shaw. Water dispersion interactions strongly influence simulated structural properties of disordered protein states. *J. Phys. Chem. B*, 119(16):5113–5123, 2015.

[140] Jessica Nasica-Labouze, Phuong H. Nguyen, Fabio Sterpone, Olivia Berthoumieu, Nicolae-Viorel Buchete, Sébastien Coté, Alfonso De Simone, Andrew J. Doig, Peter Faller, Angel Garcia, Alessandro Laio, Mai Suan Li, Simone Melchionna, Normand Mousseau, Yuguang Mu, Anant Paravastu, Samuela Pasquali, David J. Rosenman, Birgit Strodel, Bogdan Tarus, John H. Viles, Tong Zhang, Chunyu Wang, and Philippe Derreumaux. Amyloid $\beta$ protein and alzheimer's disease: When computer simulations complement experimental studies. *Chem. Rev.*, 115(9):3518–3563, 2015.

[141] Hyunbum Jang, Laura Connelly, Fernando Teran Arce, Srinivasan Ramachandran, Bruce L Kagan, Ratnesh Lal, and Ruth Nussinov. Mechanisms for the insertion of toxic, fibril-like $\beta$-amyloid oligomers into the membrane. *J. Chem. Theory Comput.*, 9(1):822–833, 2013.

[142] Cristiano L Dias, Sharareh Jalali, Yanxing Yang, and Luis Cruz. Role of cholesterol on binding of amyloid fibrils to lipid bilayers. *J. Phys. Chem. B*, 124(15):3036–3042, 2020.

[143] Florentina Tofoleanu, Bernard R Brooks, and Nicolae-Viorel Buchete. Modulation of alzheimer's a$\beta$ protofilament-membrane interactions by lipid headgroups. *ACS Chem. Neurosci.*, 6(3):446–455, 2015.

[144] Xiang Yu and Jie Zheng. Cholesterol promotes the interaction of alzheimer $\beta$-amyloid monomer with lipid bilayer. *J. Mol. Biol.*, 421(4-5):561–571, 2012.

[145] Christopher Lockhart and Dmitri K Klimov. Cholesterol changes the mechanisms of a$\beta$ peptide binding to the dmpc bilayer. *J. Chem. Info. Model.*, 57(10):2554–2565, 2017.

[146] Hongli Liu, Xuewei Liu, Shuangyan Zhou, Xiaoli An, Huanxiang Liu, and Xiaojun Yao. Disclosing the template-induced misfolding mechanism of tau protein by studying the dissociation of the boundary chain from the formed tau fibril based on a steered molecular dynamics simulation. *ACS Chem. Neurosci.*, 10(3):1854–1865, 2019.

[147] Qin Li, Chunmei Xiong, Hongli Liu, Huizhen Ge, Xiaojun Yao, and Huanxiang Liu. Computational insights into the inhibition mechanism of proanthocyanidin b2 on tau hexapeptide (phf6) oligomer. *Front. Chem.*, 9, 2021.

[148] Xuhua Li, Xuewei Dong, Guanghong Wei, Martin Margittai, Ruth Nussinov, and Buyong Ma. The distinct structural preferences of tau protein repeat domains. *Chem. Commun.*, 54(45):5700–5703, 2018.

[149] Lata Rani and Sairam S Mallajosyula. Phosphorylation-induced structural reorganization in tau-paired helical filaments. *ACS Chem. Neurosci.*, 12(9):1621–1631, 2021.

[150] Lili Zhu, Yehong Gong, Hao Lju, Gongwu Sun, Qingwen Zhang, and Zhenyu Qian. Mechanisms of melatonin binding and destabilizing the protofilament and filament of tau r3–r4 domains revealed by molecular dynamics simulation. *Phys. Chem. Chem. Phys.*, 23(36):20615–20626, 2021.

[151] Sebastian S Oakley, Mahmoud B Maina, Karen E Marshall, Youssra K Al-Hilaly, Charlie R Harrington, Claude M Wischik, and Louise C Serpell. Tau filament self-assembly and structure: Tau as a therapeutic target. *Front. Neurol.*, page 1207, 2020.

[152] Siewert J Marrink, H Jelger Risselada, Serge Yefimov, D Peter Tieleman, and Alex H De Vries. The martini force field: Coarse grained model for biomolecular simulations. *J. Phys. Chem. B*, 111(27):7812–7824, 2007.

[153] Luca Monticelli, Senthil K Kandasamy, Xavier Periole, Ronald G Larson, D Peter Tieleman, and Siewert-Jan Marrink. The martini coarse-grained force field: Extension to proteins. *J. Chem. Theory Comput.*, 4(5):819–834, 2008.

[154] Sunhwan Jo, Taehoon Kim, Vidyashankara G Iyer, and Wonpil Im. Charmm-gui: a web-based graphical user interface for charmm. *J. Comp. Chem.*, 29(11):1859–1865, 2008.

[155] David Van Der Spoel, Erik Lindahl, Berk Hess, Gerrit Groenhof, Alan E Mark, and Herman JC Berendsen. Gromacs: Fast, flexible, and free. *J. Comp. Chem.*, 26(16):1701–1718, 2005.

[156] Giovanni Bussi, Davide Donadio, and Michele Parrinello. Canonical sampling through velocity rescaling. *J. Chem. Phys.*, 126(1):014101, 2007.

[157] Herman JC Berendsen, JPM van Postma, Wilfred F van Gunsteren, ARHJ DiNola, and Jan R Haak. Molecular dynamics with coupling to an external bath. *J. Chem. Phys.*, 81(8):3684–3690, 1984.

[158] William L Jorgensen, Jayaraman Chandrasekhar, Jeffry D Madura, Roger W Impey, and Michael L Klein. Comparison of simple potential functions for simulating liquid water. *J. Chem. Phys.*, 79(2):926–935, 1983.

[159] Jeffery B Klauda, Richard M Venable, J Alfredo Freites, Joseph W O'Connor, Douglas J Tobias, Carlos Mondragon-Ramirez, Igor Vorobyov, Alexander D MacKerell Jr, and Richard W Pastor. Update of the charmm all-atom additive force field for lipids: Validation on six lipid types. *J. Phys. Chem. B*, 114(23):7830–7843, 2010.

[160] Joseph B Lim, Brent Rogaski, and Jeffery B Klauda. Update of the cholesterol force field parameters in charmm. *J. Phys. Chem. B*, 116(1):203–210, 2012.

[161] Shūichi Nosé. A molecular dynamics method for simulations in the canonical ensemble. *Mol. Phys.*, 52(2):255–268, 1984.

[162] Berk Hess, Henk Bekker, Herman JC Berendsen, and Johannes GEM Fraaije. Lincs: a linear constraint solver for molecular simulations. *J. Comp. Chem.*, 18(12):1463–1472, 1997.

[163] Xavier Daura, Karl Gademann, Bernhard Jaun, Dieter Seebach, Wilfred F Van Gunsteren, and Alan E Mark. Peptide folding: When simulation meets experiment. *Angew. Chem. Int. Ed.*, 38(1-2):236–240, 1999.

[164] Sarah-Beth TA Amos, Thomas C Schwarz, Jiye Shi, Benjamin P Cossins, Terry S Baker, Richard J Taylor, Robert Konrat, and Mark SP Sansom. Membrane interactions of $\alpha$-synuclein revealed by multiscale molecular dynamics simulations, markov state models, and nmr. *J. Phys. Chem. B*, 125(11):2929–2941, 2021.

[165] Mingzhen Zhang, Baiping Ren, Yonglan Liu, Guizhao Liang, Yan Sun, Lijian Xu, and Jie Zheng. Membrane interactions of hiapp monomer and oligomer with lipid membranes by molecular dynamics simulations. *ACS Chem. Neurosci.*, 8(8):1789–1800, 2017.

[166] Marzieh Saeedimasine, Annaclaudia Montanino, Svein Kleiven, and Alessandra Villa. Role of lipid composition on the structural and mechanical features of axonal membranes: a molecular simulation study. *Sci. Rep.*, 9(1):1–12, 2019.

[167] Tiago Mendes Ferreira, Filipe Coreta-Gomes, OH Samuli Ollila, Maria João Moreno, Winchil LC Vaz, and Daniel Topgaard. Cholesterol and popc segmental order parameters in lipid membranes: Solid state 1 h–13 c nmr and md simulation studies. *Phys. Chem. Chem. Phys.*, 15(6):1976–1989, 2013.

[168] Liqun Zhang. Disulfide bonds affect the binding sites of human $\beta$ defensin type 3 on negatively charged lipid membranes. *J. Phys. Chem. B*, 124(11):2088–2100, 2020.

[169] Kristyna Pluhackova, Sonja A Kirsch, Jing Han, Liping Sun, Zhenyan Jiang, Tobias Unruh, and Rainer A Bockmann. A critical comparison of biomembrane force fields: Structure and dynamics of model dmpc, popc, and pope bilayers. *J. Phys. Chem. B*, 120(16):3888–3903, 2016.

[170] Ganesh Shahane, Wei Ding, Michail Palaiokostas, Helena S Azevedo, and Mario Orsi. Interaction of antimicrobial lipopeptides with bacterial lipid bilayers. *J. Membr. Biol.*, 252(4):317–329, 2019.

[171] Saame Raza Shaikh, Michael R Brzustowicz, Noah Gustafson, William Stillwell, and Stephen R Wassall. Monounsaturated pe does not phase-separate from the lipid raft molecules sphingomyelin and cholesterol: Role for polyunsaturation? *Biochemistry*, 41(34):10593–10602, 2002.

[172] Vladimir Rudajev and Jiri Novotny. The role of lipid environment in ganglioside gm1-induced amyloid $\beta$ aggregation. *Membranes*, 10(9):226, 2020.

[173] Solomiia Boyko, Xu Qi, Tien-Hao Chen, Krystyna Surewicz, and Witold K Surewicz. Liquid–liquid phase separation of tau protein: the crucial role of electrostatic interactions. *J. Biol. Chem.*, 294(29):11054–11059, 2019.

[174] Harindranath Kadavath, Romina V Hofele, Jacek Biernat, Satish Kumar, Katharina Tepper, Henning Urlaub, Eckhard Mandelkow, and Markus Zweckstetter. Tau stabilizes microtubules by binding at the interface between tubulin heterodimers. *Proc. Natl. Acad. Sci. U.S.A.*, 112(24):7501–7506, 2015.

[175] Yipeng Wang and Eckhard Mandelkow. Tau in physiology and pathology. *Nat. Rev. Neurosci.*, 17(1):22–35, 2016.

144

[176] Lukas S Stelzl, Lisa M Pietrek, Andrea Holla, Javier Oroz, Mateusz Sikora, Jürgen Kofinger, Benjamin Schuler, Markus Zweckstetter, and Gerhard Hummer. Global structure of the intrinsically disordered protein tau emerges from its local structure. *JACS Au*, 2(3):673–686, 2022.

[177] Hongli Liu, Haiyang Zhong, Zerong Xu, Qianqian Zhang, Syed Jawad Ali Shah, Huanxiang Liu, and Xiaojun Yao. The misfolding mechanism of the key fragment r3 of tau protein: a combined molecular dynamics simulation and markov state model study. *Phys. Chem. Chem. Phys.*, 22(19):10968–10980, 2020.

[178] Andrew J Doig, Maria P del Castillo-Frias, Olivia Berthoumieu, Bogdan Tarus, Jessica Nasica-Labouze, Fabio Sterpone, Phuong H Nguyen, Nigel M Hooper, Peter Faller, and Philippe Derreumaux. Why is research on amyloid-$\beta$ failing to give new drugs for alzheimer's disease? *ACS Chem. Neurosci.*, 8(7):1435–1437, 2017.

[179] Eugene Bok, Eunju Leem, Bo-Ram Lee, Ji Min Lee, Chang Jae Yoo, Eun Mi Lee, and Jaekwang Kim. Role of the lipid membrane and membrane proteins in tau pathology. *Front. Cell Dev. Biol*, 9:1108, 2021.

[180] Irem Nasir, Emily P Bentley, and Ashok A Deniz. Ratiometric single-molecule fret measurements to probe conformational subpopulations of intrinsically disordered proteins. *Curr. Protoc. Chem. Biol.*, 12(1):e80, 2020.

[181] David Talaga, Willy Smeralda, Laurie Lescos, Julien Hunel, Nad'a Lepejova-Caudy, Christophe Cullin, Sébastien Bonhommeau, and Sophie Lecomte. Pip$_2$ phospholipid-induced aggregation of tau filaments probed by tip-enhanced raman spectroscopy. *Angew. Chem. Int. Edition*, 130(48):15964–15968, 2018.

[182] Utsab R Shrestha, Jeremy C Smith, and Loukas Petridis. Full structural ensembles of intrinsically disordered proteins from unbiased molecular dynamics simulations. *Commun. Biol.*, 4(1):1–8, 2021.

[183] Markus R. Hermann and Jochen S. Hub. Saxs-restrained ensemble simulations of intrinsically disordered proteins with commitment to the principle of maximum entropy. *J. Chem. Theory Comput.*, 15(9):5103–5115, 2019.

[184] Jessica Nasica-Labouze, Phuong H. Nguyen, Fabio Sterpone, Olivia Berthoumieu, Nicolae-Viorel Buchete, Sébastien Cote, Alfonso De Simone, Andrew J. Doig, Peter Faller, Angel Garcia, Alessandro Laio, Mai Suan Li, Simone Melchionna, Normand Mousseau, Yuguang Mu, Anant Paravastu, Samuela Pasquali, David J. Rosenman, Birgit , Bogdan Tarus, John H. Viles, Tong Zhang, Chunyu Wang, and Philippe Derreumaux. Amyloid $\beta$ protein and alzheimer's disease: When computer simulations complement experimental studies. *Chem. Rev.*, 115(9):3518–3563, 2015.

[185] Phuong H Nguyen and Philippe Derreumaux. Molecular dynamics simulations of the tau r3–r4 domain monomer in the bulk solution and at the surface of a lipid bilayer model. *J. Phys. Chem. B*, 126(18):3431–3438, 2022.

[186] Chad A Sallaberry, Barbie J Voss, Jaroslaw Majewski, Jacek Biernat, Eckhard Mandelkow, Eva Y Chi, and Crystal M Vander Zanden. Tau and membranes: Interactions that promote folding and condensation. *Front. Cell Dev. Biol.*, page 2632, 2021.

[187] Zeljka Korade and Anne K Kenworthy. Lipid rafts, cholesterol, and the brain. *Neuropharmacology*, 55(8):1265–1273, 2008.

[188] Elena Posse de Chaves and Simonetta Sipione. Sphingolipids and gangliosides of the nervous system in membrane function and dysfunction. *FEBS Lett.*, 584(9):1748–1759, 2010.

[189] Yu-Chia Kao, Pei-Chuan Ho, Yuan-Kun Tu, I-Ming Jou, and Kuen-Jer Tsai. Lipids and alzheimer's disease. *Int. J. Mol. Sci.*, 21(4):1505, 2020.

[190] Hoang Linh Nguyen, Huynh Quang Linh, Pawel Krupa, Giovanni La Penna, and Mai Suan Li. Amyloid $\beta$ dodecamer disrupts the neuronal membrane more strongly than the mature fibril: Understanding the role of oligomers in neurotoxicity. *J. Phys. Chem. B*, 126(20):3659–3672, 2022.

[191] Viet Hoang Man, Xibing He, Jie Gao, and Junmei Wang. Effects of all-atom molecular mechanics force fields on amyloid peptide assembly: The case of phf6 peptide of tau protein. *J. Chem. Theory Comput.*, 17(10):6458–6471, 2021.

[192] Georg Künze, Patrick Barré, Holger A Scheidt, Lars Thomas, David Eliezer, and Daniel Huster. Binding of the three-repeat domain of tau to phospholipid membranes induces an aggregated-like state of the protein. *Biochim. Biophys. Acta.*, 1818(9):2302–2313, 2012.

[193] Benjamin Falcon, Jasenko Zivanov, Wenjuan Zhang, Alexey G Murzin, Holly J Garringer, Ruben Vidal, R Anthony Crowther, Kathy L Newell, Bernardino Ghetti, Michel Goedert, et al. Novel tau filament fold in chronic traumatic encephalopathy encloses hydrophobic molecules. *Nature*, 568(7752):420–423, 2019.

[194] Sofia Lövestam, Fujiet Adrian Koh, Bart van Knippenberg, Abhay Kotecha, Alexey G Murzin, Michel Goedert, and Sjors HW Scheres. Assembly of recombinant tau into filaments identical to those of alzheimer's disease and chronic traumatic encephalopathy. *Elife*, 11:e76494, 2022.

[195] Yanxing Yang, Sharareh Jalali, Bradley L Nilsson, and Cristiano L Dias. Binding mechanisms of amyloid-like peptides to lipid bilayers and effects of divalent cations. *ACS Chem. Neurosci.*, 12(11):2027–2035, 2021.

146

[196] Koushirou Sogawa, Katsuhiko Minoura, Yasuko In, Toshimasa Ishida, Taizo Taniguchi, and Koji Tomoo. Ch–$\pi$ interaction in vqivyk sequence elucidated by nmr spectroscopy is essential for phf formation of tau. *Peptide Sci.*, 102(3):288–295, 2014.

[197] Koushirou Sogawa, Ryouhei Okuda, Yasuko In, Toshimasa Ishida, Taizo Taniguchi, Katsuhiko Minoura, and Koji Tomoo. C–h $\pi$ interplay between ile308 and tyr310 residues in the third repeat of microtubule binding domain is indispensable for self-assembly of three-and four-repeat tau. *J. Biochem.*, 152(3):221–229, 2012.

[198] M Von Bergen, P Friedhoff, J Biernat, J Heberle, E-M Mandelkow, and E Mandelkow. Assembly of $\tau$ protein into alzheimer paired helical filaments depends on a local sequence motif ($^{306}$vqivyk$^{311}$) forming $\beta$ structure. *Proc. Natl. Acad. Sci. U.S.A*, 97(10):5129–5134, 2000.

[199] Michael R Sawaya, Shilpa Sambashivan, Rebecca Nelson, Magdalena I Ivanova, Stuart A Sievers, Marcin I Apostol, Michael J Thompson, Melinda Balbirnie, Jed JW Wiltzius, Heather T McFarlane, et al. Atomic structures of amyloid cross-$\beta$ spines reveal varied steric zippers. *Nature*, 447(7143):453–457, 2007.

[200] Sarah Rauscher, Vytautas Gapsys, Michal J Gajda, Markus Zweckstetter, Bert L De Groot, and Helmut Grubmuller. Structural ensembles of intrinsically disordered proteins depend strongly on force field: a comparison to experiment. *J. Chem. Theory Comput.*, 11(11):5513–5524, 2015.

[201] Birgit Strodel. Amyloid aggregation simulations: Challenges, advances and perspectives. *Curr. Opin. Struct. Biol.*, 67:145–152, 2021.

[202] Gül H Zerze, Wenwei Zheng, Robert B Best, and Jeetain Mittal. Evolution of all-atom protein force fields to improve local and global properties. *J. Phys. Chem. Lett.*, 10(9):2227–2234, 2019.

[203] Hasna Ahyayauch, Michal Raab, Jon V Busto, Nagore Andraka, José-Luis R Arrondo, Massimo Masserini, Igor Tvaroska, and Félix M Goñi. Binding of $\beta$-amyloid (1–42) peptide to negatively charged phospholipid membranes in the liquid-ordered state: Modeling and experimental studies. *Biophys. J.*, 103(3):453–463, 2012.

[204] Anne M Brown and David R Bevan. Molecular dynamics simulations of amyloid $\beta$-peptide (1-42): Tetramer formation and membrane interactions. *Biophys. J.*, 111(5):937–949, 2016.

[205] Patrick Barré and David Eliezer. Structural transitions in tau k18 on micelle binding suggest a hierarchy in the efficacy of individual microtubule-binding repeats in filament nucleation. *Protein Sci.*, 22(8):1037–1048, 2013.

[206] Vladimir Rudajev and Jiri Novotny. The role of lipid environment in ganglioside gm1-induced amyloid $\beta$ aggregation. *Membranes*, 10(9):226, 2020.

[207] Katsumi Matsuzaki. A$\beta$–ganglioside interactions in the pathogenesis of alzheimer's disease. *Biochim. Biophys. Acta Biomembr.*, 1862(8):183233, 2020.

[208] Yu-Lin Guo, Wen-Jun Duan, Dan-Hua Lu, Xiao-Hui Ma, Xiao-Xiao Li, Zhao Li, Wei Bi, Hiroshi Kurihara, Hai-Zhi Liu, Yi-Fang Li, et al. Autophagy-dependent removal of $\alpha$-synuclein: a novel mechanism of gm1 ganglioside neuroprotection against parkinson's disease. *Acta Pharmacol. Sin.*, 42(4):518–528, 2021.

[209] Indrani Bera and Jeffery B Klauda. Molecular simulations of mixed lipid bilayers with sphingomyelin, glycerophospholipids, and cholesterol. *J. Phys. Chem. B*, 121(20):5197–5208, 2017.

[210] M Goedert, R Jakes, MG Spillantini, M Hasegawa, MJ Smith, and RA Crowther. Assembly of microtubule-associated protein tau into alzheimer-like filaments induced by sulphated glycosaminoglycans. *Nature*, 383(6600):550–553, 1996.

[211] Galina Limorenko and Hilal A Lashuel. Revisiting the grammar of tau aggregation and pathology formation: How new insights from brain pathology are shaping how we study and target tauopathies. *Chem. Soc. Rev.*, 2022.

[212] E Köpke, Yunn-Chyn Tung, Sadia Shaikh, A del C Alonso, Khalid Iqbal, and I Grundke-Iqbal. Microtubule-associated protein tau. abnormal phosphorylation of a non-paired helical filament pool in alzheimer disease. *J. Biol. Chem.*, 268(32):24374–24384, 1993.

[213] Dennis J Selkoe. Treatments for alzheimer's disease emerge. *Science*, 373(6555):624–626, 2021.

[214] Carmen N Chirita, Erin E Congdon, Haishan Yin, and Jeff Kuret. Triggers of full-length tau aggregation: a role for partially folded intermediates. *Biochemistry*, 44(15):5862–5872, 2005.

[215] Gerald P. Gellermann, Thomas R. Appel, Peter Davies, and Stephan Diekmann. Paired helical filaments contain small amounts of cholesterol, phosphatidylcholine and sphingolipids. 387(9):1267–1274, 2006.

[216] Eva Y Chi, Canay Ege, Amy Winans, Jaroslaw Majewski, Guohui Wu, Kristian Kjaer, and Ka Yee C Lee. Lipid membrane templates the ordering and induces the fibrillogenesis of alzheimer's disease amyloid-$\beta$ peptide. *Proteins*, 72(1):1–24, 2008.

[217] Victoria Campos-Peña, José Tapia-Ramírez, Carmen Sánchez-Torres, and Marco Antonio Meraz-Rios. Pathological-like assembly of tau induced by a paired helical filament core expressed at the plasma membrane. *J. Alzheimer's Dis.*, 18(4):919–933, 2009.

[218] Lisa A Flanagan, C Casey Cunningham, Jian Chen, Glenn D Prestwich, Kenneth S Kosik, and Paul A Janmey. The structure of divalent cation-induced aggregates of pip2 and their alteration by gelsolin and tau. *Biophys. J.*, 73(3):1440–1447, 1997.

[219] Stuart McLaughlin, Jiyao Wang, Alok Gambhir, and Diana Murray. Pip2 and proteins: Interactions, organization, and information flow. *Annu. Rev. Biophys. Biomol. Struct.*, 31(1):151–175, 2002.

[220] Tamas Balla. Phosphoinositides: Tiny lipids with giant impact on cell regulation. *Physiological reviews*, 93(3):1019–1137, 2013.

[221] Philip W Majerus, Thomas M Connolly, Hans Deckmyn, Theodora S Ross, Teresa E Bross, Hidemi Ishii, Vinay S Bansal, and David B Wilson. The metabolism of phosphoinositide-derived messenger molecules. *Science*, 234(4783):1519–1526, 1986.

[222] Thomas FJ Martin. Role of pi (4, 5)p2 in vesicle exocytosis and membrane fusion. *Phosphoinositides II: The Diverse Biological Functions*, pages 111–130, 2012.

[223] Liqun Zhang. Interaction of human $\beta$ defensin type 3 (hbd-3) with different pip2-containing membranes, a molecular dynamics simulation study. *J. Chem. Inf. Model.*, 61(9):4670–4686, 2021.

[224] Robert J Allsopp and Jeffery B Klauda. Impact of pip2 lipids, force field parameters, and mutational analysis on the binding of the osh4's $\alpha 6 - \alpha 7$ domain. *J. Phys. Chem. B*, 125(20):5296–5308, 2021.

[225] Emilia L Wu, Yifei Qi, Kevin C Song, Jeffery B Klauda, and Wonpil Im. Preferred orientations of phosphoinositides in bilayers and their implications in protein recognition mechanisms. *J. Phys. Chem. B*, 118(16):4315–4325, 2014.

[226] Unmesh D Chowdhury, Arnav Paul, and BL Bhargava. Interaction of the tau fibrils with the neuronal membrane. *Biophys. Chem.*, page 107024, 2023.

[227] Zheng Li, Richard M Venable, Laura A Rogers, Diana Murray, and Richard W Pastor. Molecular dynamics simulations of pip2 and pip3 in lipid bilayers: Determination of ring orientation, and the effects of surface roughness on a poisson-boltzmann description. *Biophys. J.*, 97(1):155–163, 2009.

[228] Emilia L. Wu, Xi Cheng, Sunhwan Jo, Huan Rui, Kevin C. Song, Eder M. Davila-Contreras, Yifei Qi, Jumin Lee, Viviana Monje-Galvan, Richard M. Venable, Jeffery B. Klauda, and Wonpil Im. Charmm-gui membrane builder toward realistic biological membrane simulations. *J. Comp. Chem.*, 35(27):1997–2004, 2014.

[229] Naveen Michaud-Agrawal, Elizabeth J Denning, Thomas B Woolf, and Oliver Beckstein. Mdanalysis: a toolkit for the analysis of molecular dynamics simulations. *J. Comp. Chem.*, 32(10):2319–2327, 2011.

[230] Olaf S Andersen and Roger E Koeppe. Bilayer thickness and membrane protein function: an energetic perspective. *Annu. Rev. Biophys. Biomol. Struct.*, 36:107–130, 2007.

[231] Frederick A Heberle, Robin S Petruzielo, Jianjun Pan, Paul Drazba, Norbert Kucerka, Robert F Standaert, Gerald W Feigenson, and John Katsaras. Bilayer thickness mismatch controls domain size in model membranes. *J. Am. Chem. Soc.*, 135(18):6853–6859, 2013.

[232] Justin A Lemkul and David R Bevan. Perturbation of membranes by the amyloid $\beta$-peptide–a molecular dynamics study. *FEBS J.*, 276(11):3060–3075, 2009.

[233] Jacob J Kinnun, KJ Mallikarjunaiah, Horia I Petrache, and Michael F Brown. Elastic deformation and area per lipid of membranes: atomistic view from solid-state deuterium nmr spectroscopy. *Biochim. Biophys. Acta - Biomembr.*, 1848(1):246–259, 2015.

[234] TJ McIntosh. Differences in hydrocarbon chain tilt between hydrated phosphatidylethanolamine and phosphatidylcholine bilayers. a molecular packing model. *Biophys. J.*, 29(2):237–245, 1980.

[235] JF Nagle. Theory of lipid monolayer and bilayer phase transitions: effect of headgroup interactions. *J. Membr. Biol.*, 27(1):233–250, 1976.

[236] Sze May Yee, Richard J Gillams, Sylvia E McLain, and Christian D Lorenz. Effects of lipid heterogeneity on model human brain lipid membranes. *Soft Matter*, 17(1):126–135, 2021.

[237] S Tristram-Nagle, R Zhang, RM Suter, CR Worthington, WJ Sun, and JF Nagle. Measurement of chain tilt angle in fully hydrated bilayers of gel phase lecithins. *Biophys. J.*, 64(4):1097–1109, 1993.

[238] Maria C Neves, Hugo AL Filipe, Rita Leones Reis, João P Prates Ramalho, Filipe Coreta-Gomes, Maria J Moreno, and Luis Loura. Interaction of bile salts with lipid bilayers: An atomistic molecular dynamics study. *Front. Physiol.*, page 393, 2019.

[239] T Devanand, Sankaran Krishnaswamy, and Satyavani Vemparala. Interdigitation of lipids induced by membrane–active proteins. *J. Membr. Biol.*, 252:331–342, 2019.

[240] Sharon E Miller, Daniela A Sahlender, Stephen C Graham, Stefan Höning, Margaret S Robinson, Andrew A Peden, and David J Owen. The molecular basis for the endocytosis of small r-snares by the clathrin adaptor calm. *Cell*, 147(5):1118–1131, 2011.

[241] Andreas Santamaria, Javier Carrascosa-Tejedor, Eduardo Guzmán, Nathan R Zaccai, and Armando Maestro. Unravelling the orientation of the inositol-biphosphate ring and its dependence on phosphatidylinositol 4, 5-bisphosphate cluster formation in model membranes. *J. Colloid Interface Sci.*, 629:785–795, 2023.

[242] Eva Bilkova, Roman Pleskot, Sami Rissanen, Simou Sun, Aleksander Czogalla, Lukasz Cwiklik, Tomasz Róg, Ilpo Vattulainen, Paul S Cremer, Pavel Jungwirth, et al. Calcium directly regulates phosphatidylinositol 4, 5-bisphosphate headgroup conformation and recognition. *J. Am. Chem. Soc.*, 139(11):4019–4024, 2017.

[243] Elizabeth Drolle, Alexander Negoda, Keely Hammond, Evgeny Pavlov, and Zoya Leonenko. Changes in lipid membranes may trigger amyloid toxicity in alzheimer's disease. *PloS one*, 12(8):e0182194, 2017.

[244] Marieke Kranenburg, Martin Vlaar, and Berend Smit. Simulating induced interdigitation in membranes. *Biophys. J.*, 87(3):1596–1605, 2004.

[245] Myriam M Ouberai, Juan Wang, Marcus J Swann, Celine Galvagnion, Tim Guilliams, Christopher M Dobson, and Mark E Welland. $\alpha$-synuclein senses lipid packing defects and induces lateral expansion of lipids leading to membrane remodeling. *J. Biol. Chem.*, 288(29):20883–20895, 2013.

[246] Kyungreem Han, Soon Ho Kim, Richard M Venable, and Richard W Pastor. Design principles of pi(4,5)p$_2$ clustering under protein-free conditions: Specific cation effects and calcium-potassium synergy. *Proc. Natl. Acad. Sci. U.S.A.*, 119(22):e2202647119, 2022.

[247] Kyungreem Han, Arne Gericke, and Richard W Pastor. Characterization of specific ion effects on pi(4,5)p$_2$ clustering: molecular dynamics simulations and graph-theoretic analysis. *J. Phys. Chem. B*, 124(7):1183–1196, 2020.

[248] Kyungreem Han, Richard W Pastor, and Cristina Fenollar-Ferrer. Pld2–pi (4, 5) p2 interactions in fluid phase membranes: Structural modeling and molecular dynamics simulations. *PLoS One*, 15(7):e0236201, 2020.

[249] Yu-Hsiu Wang, Agnieszka Collins, Lin Guo, Kathryn B Smith-Dupont, Feng Gai, Tatyana Svitkina, and Paul A Janmey. Divalent cation-induced cluster formation by polyphosphoinositides in model membranes. *J. Am. Chem. Soc.*, 134(7):3387–3395, 2012.

[250] Maria J Sarmento, Ana Coutinho, Aleksander Fedorov, Manuel Prieto, and Fabio Fernandes. $Ca^{2+}$ induces pi(4,5)p$_2$ clusters on lipid bilayers at physiological pi(4,5)p$_2$ and ca$^{2+}$ concentrations. *Biochimica et Biophysica Acta (BBA)-Biomembranes*, 1838(3):822–830, 2014.

[251] John A Corbin, Ronald A Dirkx, and Joseph J Falke. Grp1 pleckstrin homology domain: Activation parameters and novel search mechanism for rare target lipid. *Biochemistry*, 43(51):16161–16173, 2004.
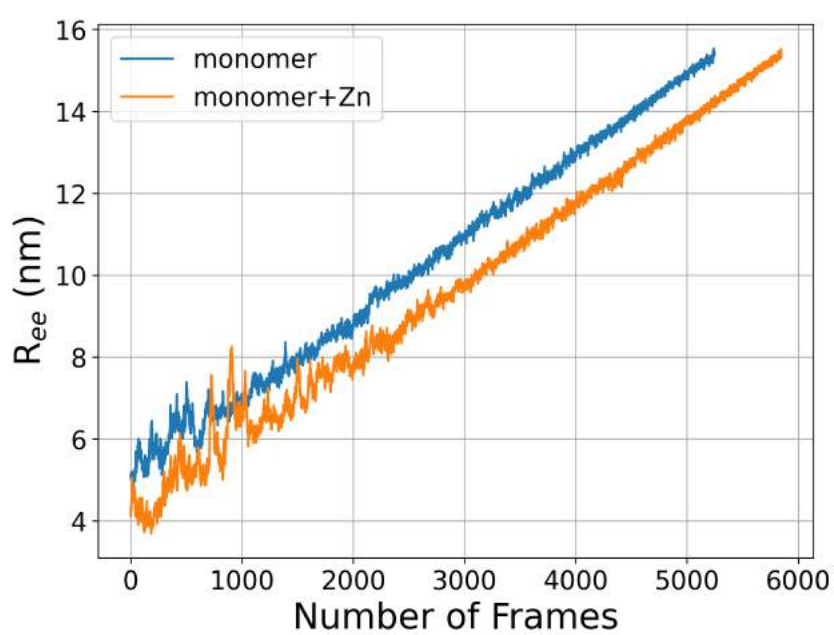
# Appendix A



Figure A.1: End-to-end distance being plotted with respect to the number of frames for the pulling simulations.
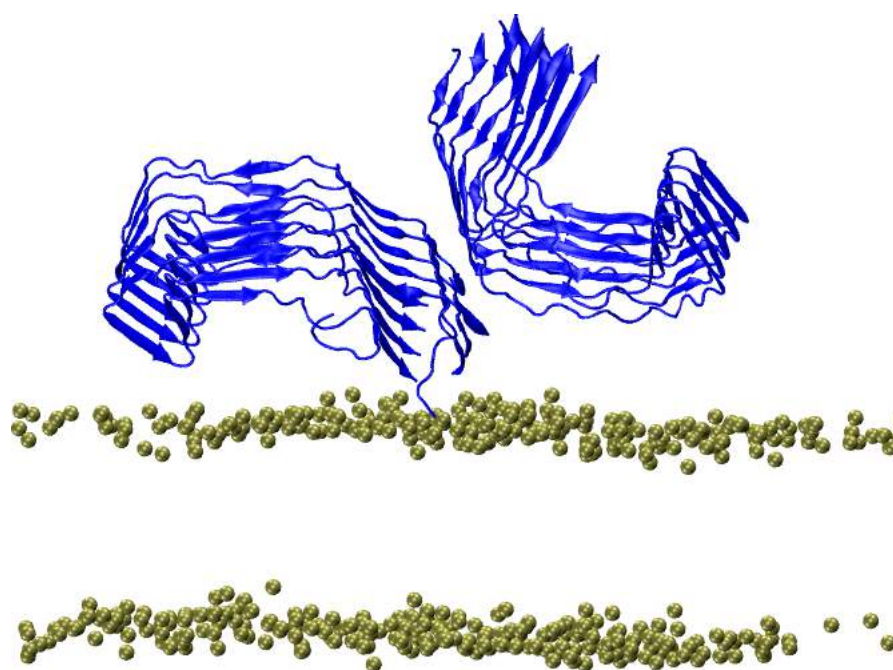
Figure A.2: Final snapshot of the tau fibril over the POPC lipid with the tau shown in new cartoon representation and the phosphorus headgroups shown in VDW representation.